

https://dspace.org/

Identification of inelastic deformation mechanisms around deep level mining stopes and their application to improvements of mining techniques.

Kuijpers, J.S.

2014-02-26
http://hdl.handle.net10539/13969

Downloaded from a DSpace repository. https://dspace.org/

IDENTIFICATION OF INELASTIC DEFORMATION MECHANISMS AROUND DEEP LEVEL MINING STOPES AND THEIR APPLICATION TO IMPROVEMENTS OF MINING TECHNIQUES

J.S. Kuijpers

Thesis submitted for the Degree of Doctor of Philosophy in the Faculty of Engineering

UNIVERSITY OF THE WITWATERSRAND

Johannesburg, 1998

ABSTRACT

Mining induced fracturing and associated deformations can commonly be observed around deep gold mining excavations. As the rockmass behaviour and the stability of the excavations are directly influenced by these processes, a proper understanding of this influence would certainly improve current mining practices with respect to blasting, rock breaking, support design and mining lay-outs.

The main subject of this thesis is the physics of failure and post failure behaviour of rock and similar materials. Failure is defined here as a state at which the material has been subjected to fracture and/or damage processes. The applicability of commonly used constitutive models in representing such failure and post failure processes has been investigated mainly by means of numerical simulations. Mechanisms which control fundamental fracture and damage processes have been analysed by comparing the results from relevant laboratory experiments with numerical models.

Linear elastic fracture mechanics has been applied to explain and simulate the formation of large scale extension fractures which form in response to excessive tensile stresses. Using the flaw concept it is demonstrated that these fractures not only initiate and propagate from the surface of an opening in compressed rock, but that so called secondary fracturing can be initiated from within the solid rock as well. The effect of geological discontinuities such as bedding planes, faults and joints on the formation of (extension) fractures has also been investigated and it has been shown how the presence of such discontinuities can cause the formation of additional fractures.

Micro mechanical models have been used to investigate the interaction and coalescence processes of micro fractures. It was found that the formation of large scale extension fracturing can be explained from such processes, but so called shear fractures could not directly be reproduced, although such a possibility has been claimed by previous researchers. The formation of shear fractures is of particular interest as violent failure of rock, which is subjected to compressive stresses only, is often associated with such fractures. In an all compressive stress environment, only shear deformations would allow for the relief of excess stress and thus energy.

The formation of shear fractures is associated with complex mechanisms and shear fractures can therefore not directly be represented by single cracks. In contrast to the propagation of tensile fractures, which can readily be explained by traditional fracture mechanics in terms of stress concentrations around the crack tip, the propagation of shear fractures requires a different explanation. In this thesis an attempt has nevertheless been made to reproduce shear fractures by direct application of fracture mechanics. This his been done by representing a shear fracture as a single crack and by assuming fracture growth criteria which are either based on critical excess shear stresses, or on a maximum energy release. Both criteria are completely empirical and require a value for the critical shear resistance in the same way as a critical tensile resistance is required to represent the formation of tensile fractures. The determination of a critical tensile resistance (K_{Ic}) is relatively straight forward, as the formation of tensile fractures from a pre-existing flaw can be reproduced and observed in standard laboratory tests. The determination of a critical

shear resistance is, however, not a common practice, as the formation of a shear fracture from a pre-existing flaw is very infrequently observed.

The application of shear fracture growth criteria nevertheless resulted in plausible fracture patterns, which suggests that such criteria are realistic. It is argued here however that the formation of shear fractures cannot be associated with primary fracture growth, but rather with the localisation of failure and damage in an area which is subjected to plastic deformation. The application of fracture mechanics is therefore not correct from a fundamental point of view as these processes are not represented. For this reason plasticity theory has also been applied in order to simulate failure in general, and shear failure localisation in particular. It was in principle possible to reproduce the shear fractures with the use of this theory, but numerical restraints affected the results to such an extent that most of the simulations were not realistic. Plasticity theory can also be extended to include brittle behaviour by the use of so called strain softening models. The physical processes which lead to brittle failure are however not directly represented by such models and they may therefore not result in realistic failure patterns. It was in fact found that strain softening models could only produce realistic results if localisation of failure could be prevented. The effect of numerical restraints becomes even more obvious with a strain softening model in the case of failure localisation.

While the plasticity models appear inappropriate in representing brittle failure, they demonstrated that plastic deformations can be associated with stress changes which may lead to subsequent brittle fracturing. Although only indirect attempts have been made to reproduce this effect, as appropriate numerical tools are not available, it is clear that many observations of extension fracturing could be explained by plastic deformations *preceding* the brittle fracturing processes. Many rocks are classified as brittle, but plastic deformation processes often occur during the damage processes as well. The sliding crack for instance, which is thought to represent many micro mechanical deformation processes in rock, directly induces plastic deformations when activated. A pure brittle rock, which may be defined as a rock in which absolutely no plastic deformation processes take place, may therefore only be of academic interest as it is inconceivable that such a rock material exists. Only in such an academic case would (linear) elastic fracture mechanics be directly applicable. As plastic deformation processes do play a role in real rock materials it is important to investigate their influence on subsequent brittle failure processes. The elastic stress distribution, which is often used to explain the onset of brittle fracturing, may be misleading as plastic deformations can substantially affect the stress distribution preceding fracture initiation.

In an attempt to combine both plastic and brittle failure, use has been made of tessellation models, which in effect define potential fracture paths in a random mesh. The advantage of these models is that various failure criteria, with or without strain softening potential, can be used without the numerical restraints which are normally associated with the conventional continuum models. The results of these models are also not free from numerical artefacts, but they appear to be more realistic in general. One of the major conclusions based on these results is that shear failure does not occur in a localised fashion, but is associated with the uniform distribution and extension of damage. Shear failure, which can be related directly to plastic failure, can however induce brittle, tensile, failure due to stress redistribution.

While the theories of fracture mechanics and plasticity are well established, their application to rock mechanical problems often leads to unrealistic results. Commonly observed fracture patterns in rock, loaded in compression, are most often not properly reproduced by numerical models for a combination of reasons. Either a model concentrates on the discrete fracturing processes, in which case the plastic deformation processes are ignored, or plasticity is represented, but brittle failure is poorly catered for. While theoretically a combination of these models might lead to better representations and simulations, numerical problems do affect all models to a certain extent and a practical solution is not immediately available. The results of numerical models can therefore only be analysed with caution and the underlying assumptions and numerical problems associated with a particular technique need to be appreciated before such results can be interpreted with any sense. Many of the problems are identified here and this may assist researchers in the interpretation of results from numerical simulations.

Laboratory experiments, which have been chosen for analyses, involve specimens which have been subjected to compressive stresses and which contain openings from which failure and fracturing is initiated. Such specimens are less subjective to boundary influences and are far more representative of conditions around mining excavations than typical uni- and tri-axial tests. The uniform stress conditions in these latter tests allow boundary effects to dominate the stress concentrations, and thus failure initiation, in the specimens. The large stress gradients, which can be expected to occur around underground excavations, are not reproduced in such specimens. As a consequence failure is not contained within a particular area, but spreads throughout the complete specimen in the uni- and tri-axial tests. Specimens containing openings are therefore far more likely to reproduce the fracture patterns which can be observed around deep level mining excavations.

Numerical simulations of brittle, tensile fracturing around mining excavations resulted in consistent fracture patterns. Fracture patterns could however be strongly influenced by the presence of geological (pre-existing) discontinuities such as bedding planes. Although tensile stresses are often assumed to be absent around deep level excavations because typical hanging- and foot-walls are subjected to compressive horizontal strain and thus stress, the numerical models identified alternative locations of tensile stress and also mechanisms which could induce secondary tensile stresses. A tensile failure criterion has therefore been identified as the most likely cause of large scale fracturing while shear fracturing may only occur in the absence of such tensile stresses and only as a consequence of failure localisation in damaged rock rather than fracture propagation (in solid rock). Geological discontinuities can easily induce tensile stresses when mobilised and may even replace the mining induced fractures by offering a more efficient means for energy release. The latter possibility is a true three dimensional issue which has not been addressed any further in this study, but may be very relevant to jointed rock.

Although dynamic failure has not directly been addressed, one of the mechanisms for brittle, and thus stress relieving, failure under compressive stress conditions has been investigated in detail, namely shear fracturing. Shear fractures are effectively the only discontinuities which allow for stress relief under such conditions in the absence of pre-existing, geological discontinuities, and are therefore quite relevant to dynamic rock failure, such as rock bursts, in deep level mining conditions. Potential mechanisms for

shear fracture formation and the numerical simulation of these features have been investigated and this may especially assist further research into rock bursts.

DECLARATION

I, Johannes Stanislaus Kuijpers, declare that this thesis is my own work and that it has not been submitted for a degree at any other university.

J.S. Kuijpers

July 1998

ACKNOWLEDGEMENTS

I wish to thank the following people and organizations for their support and encouragement:

My supervisor at CSIR Miningtek, Dr. John Napier for his inspiration and unabated enthusiasm. Especially the many discussions with him allowed me to develop a clearer vision on the subjects related to this thesis. The computer programme DIGS is his brainchild and has been used thoroughly throughout this thesis.

My supervisor at Wits University, Dr. Ugur Ozbay for his patience and persistence during the many years which it took to finalize this work.

Dr. Peter Cundall for his clear and practical comments. His inspiring work, combining sound physical interpretation with theoretical models, has been used as an example.

Colleagues, ex-colleagues and friends at Miningtek whom have been helpful in many dedicated technical discussions and practical assistance. In this respect I specially want to mention Drs. N. Gay, E. Siebrits, M. Handley, L. Wojno, E. Sellers, J. Schweitzer, J. Berlenbach, and Messrs. A. Jager, N. Lightfoot, G. York, M. Hildyard, F. Malan, J. Glisson, A. Squelch, O. Goldbach

Colleagues which have assisted with laboratory work, especially B. Watson, J. Sachse and F. Swart

The division of Miningtek of the Council for Scientific and Industrial Research (CSIR) who enabled this research to take place as part of their research programme.

The Safety In Mines Research and Advisory Committee (SIMRAC) for their financial support.

My family and friends for their continuous trust and belief in me.

TABLE OF CONTENTS

1.0 INTRODUCTION 1

1.1 General 1
1.2 Observations around deep level excavations 2
1.3 Current design practices 6
1.4 Motivation and outline of present research 7

2.0 APPLICATION OF FRACTURE MECHANICS TO ROCK FRACTURING 10

2.1 Introduction 10
2.2 Numerical modelling of brittle fracturing 15
2.3 Micro fracturing and potential fracture coalescence mechanisms under compressive stresses 23
2.3.1 Sliding crack model 23
2.3.2 Pressurised crack model 28
2.3.3 Open flaw model 33
2.4 Conclusions 34

3.0 APPLICATION OF PLASTICITY TO THE FAILURE OF ROCK 36

3.1 Introduction 36
3.2 Mohr-Coulomb and shear band localisation 37
3.3 Numerical simulation of shear localisation 57
3.4 Conclusions 62

4.0 THE SEARCH FOR A SHEAR FRACTURE CRITERION 65

4.1 Introduction 65
4.2 Shear fracture growth from numerical simulations 73
4.3 Conclusions 76

5.0 OBSERVATIONS FROM LABORATORY EXPERIMENTS IN RELATION TO THE FRACTURING OF ROCK 79

5.1 Fracturing around cylindrical openings in rock subjected to compression 79
5.2 Fracturing around rectangular openings in rock subjected to compression 88
5.3 Experiments designed to induce shear fracturing 102
5.3.1 Introduction 102
5.3.2 Fracturing around inclined slots in bi-axially loaded specimens 100
5.3.3 Fracturing in punch through shear experiments 120
5.3.3.1 Numerical simulations of the punch-through experiment with FLAC 122
5.3.3.2 Numerical simulations of the punch-through experiment with DIGS 127
5.4 Conclusions 138

6.0	APPLICATIONS	**140**
	6.1 Fracture formation ahead of stope faces	140
	6.1.1 Introduction	140
	6.1.2 DIGS simulation of shear fracturing ahead of a stope face	140
	6.1.3 FLAC simulation of shear fracturing ahead of a stope face	143
	6.2 Bedding planes	145
	6.2.1 General	145
	6.2.2 Bedding planes in FLAC simulations	149
	6.2.3 Bedding planes in DIGS simulations	153
	6.3 Punching	160
	6.4 Effect of loading history under inelastic conditions	162
	6.5 Summary	169
7.0	DISCUSSION AND CONCLUSIONS	**171**
8.0	RECOMMENDATIONS	**176**
	REFERENCES	**178**

LIST OF FIGURES

2.1 Illustration of two linear variation displacement discontinuity elements used to represent normal and shear discontinuities in DIGS 15
2.2 Discontinuity interactions that can lead to numerical instabilities 16
2.3 Tangential stress directly and immediately ahead of a crack tip 17
2.4 Numerical and theoretical values for the tangential stresses ahead of a flaw with a length of 100 units in a hydrostatic tensile stress field 17
2.5a Distribution of minor principal stresses around an open flaw in a uni-axial stress field before fracture initiation (DIGS) 18
2.5b Distribution of minor principal stresses around an open flaw in a uni-axial stress field after some growth of the primary fractures (DIGS) 19
2.6 Primary and secondary fracture growth around a single open flaw in a uni-axial stress field 20
2.7 Fracture development from a single pore with a length of 4 units 20
2.8a Stress distribution around a flaw in a pure shear stress field before the initiation of fracturing 21
2.8b Stress distribution around a flaw in a shear stress field after the formation of the mode I fractures 22
2.9 Stress-strain behaviour of sliding cracks with and without wing crack formation (uni-axial loading, DIGS modelling results) 24
2.10 Sliding crack model (after Meyer et. al., 1992) 25
2.11 Coalescence of two sliding cracks into an effective "shear" fracture 26
2.12 Coalescence of two sliding cracks into a "splitting" fracture 27
2.13 Numerical simulation of micro fracture formation and interaction (after Zheng et. al., 1989) 29
2.14 Band of interacting micro fractures initiated from an initial flaw A, in a random flaw distribution in a bi-axial stress field, under minimum crack pressurisation (DIGS) 30
2.15 Band of interacting micro fractures initiated from an initial flaw A, in a random flaw distribution in a bi-axial stress field, under very high crack pressurisation (DIGS) 31
2.16 Distribution of minimum principal stresses around the tip of a pressurised crack in a vertical uni-axial stress field (DIGS) 31
2.17 Band of interacting micro fractures initiated from a regular flaw distribution (DIGS) 32
2.18 Distribution of tensile minor principal stresses around an open flaw in the form of slot A-B (DIGS, half symmetry) 33
2.19 Distribution of minor tensile principal stresses around a horizontal slot in a uni-axial compressive stress field after the formation of a vertical fracture (DIGS, half symmetry) 34
3.1 Typical stress-strain relation observed in tensile testing of metals 36
3.2 Mohr envelope based on the results of various tri-axial tests 37
3.3 Cohesion softening and friction hardening as a function of damage (after Martin, 1995) 39
3.4 Mohr stress circle and Coulomb yield surface 40
3.5 Plastic deformations and parameters associated with the plastic potential function 41

3.6	Dilation associated with sliding along a plane	43
3.7	Relation between hardening modulus and shear band inclination	48
3.8	Orientation of the shear band and the local axes	50
3.9a	Stress-strain relations for various possible shear band orientations (after Vermeer and de Borst, 1984)	53
3.9b	Bifurcation with associated softening and stress rotations inside the shear band	54
3.10	Consecutive stages of failure localisation in a uni-axially loaded specimen (FLAC)	58
3.11	Stress-strain relation for the simulation shown in Figure 3.10	58
3.12	Results from a simulation in which the dilation angle was increased to 30°	59
3.13	Development of a shear zone from a flaw in the centre of the specimen	59
3.14	Contours of damage and the stress-strain relation for a strain softening model	60
3.15	Contours of damage and the stress-strain relation for a strain softening model	61
3.16	Contours of damage and the stress-strain relation for a strain softening model	61
3.17	Shear fracture propagation from the tip of a compressed notch	62
4.1	Mode II fracture conditions	67
4.2	Stresses around a mode II fracture tip	68
4.3	ESS criterion for pure mode II conditions	69
4.4	Relative value for the energy criterion around a mode II crack tip	71
4.5	Relative values for the energy criterion when tensile stresses are completely suppressed by a compressive hydrostatic stress field	72
4.6	Relative values for the energy criterion when tensile stresses are partially suppressed by a compressive hydrostatic stress field	72
4.7	Resulting fractures for (pure) mode II conditions	73
4.8	Fracture geometry for mode II loading conditions with varying additional hydrostatic compressive stresses for both criteria	74
4.9	Stress distribution around a mode II fracture tip (FLAC)	76
5.1	Numerical simulation of the fracturing around a uni-axially loaded specimen containing a circular opening (DIGS, double symmetry)	80
5.2	Fracturing around a hole in a large specimen of Timeball Hill Quartzite	81
5.3	Effect of confinement on the stiffness of various rocks (after Stavropoulou, 1982)	83
5.4	Comparison between the linear elastic and pressure dependent elastic model (after Maury, 1987)	85
5.5	Simulated (tensile) fracture pattern due to the presence of a horizontal "crushing" zone in the sidewall of a circular opening (DIGS)	88
5.6	Fractures induced in sandstone due to bi-axial loading (after Gay, 1976)	90
5.7	Tensile fracturing around a horizontal slot. Ratio of horizontal versus vertical stress = 0.4 (DIGS)	91
5.8	Tensile fracturing around a horizontal slot. Ratio of horizontal versus vertical stress = 0.0 (DIGS)	92
5.9	Tensile fracturing around a horizontal slot from seeds which are represented by stress raisers (pores). Ratio between horizontal and vertical stress = 0.4 (DIGS)	92
5.10	Tessellation scheme of potential fracture locations used in the following numerical simulations of fracturing around slots in a compressive stress field	94
5.11	Tensile failure; cohesion before failure = 900MPa (practically infinite); cohesion after failure = 0MPa; tensile strength =1MPa	95

5.12	Cohesion softening with high tensile strength; cohesion before failure = 20MPa; cohesion after failure = 0MPa; tensile strength = 20MPa	95
5.13	Cohesion softening with low tensile strength; cohesion before failure = 20MPa; cohesion after failure = 0MPa; tensile strength = 1MPa	96
5.14	Perfectly plastic with high tensile strength; cohesion before failure = 20MPa; cohesion after failure = 20MPa; tensile strength = 20MPa	96
5.15	Perfectly plastic with low tensile strength; cohesion before failure = 20MPa; cohesion after failure = 20MPa; tensile strength = 1MPa	96
5.16	Tensile failure in a stress field of 60MPa vertical and 20MPa horizontal stress (K = 0.33)	97
5.17	Cohesion softening with high tensile strength and a double slot length; cohesion before failure = 20MPa; after failure = 0MPa, tensile strength = 20MPa	97
5.18	Regular mesh of Delaunay triangles selected for the simulations shown in Figure 5.19	98
5.19	Results from the regular Delaunay mesh; tensile strength = 20MPa	99
5.20	Regular hexagonal mesh used in the following simulations	99
5.21	Results from a regular hexagonal mesh, tensile strength = 20MPa	100
5.22	Results from a regular hexagonal mesh with reduced strength	100
5.23	Fracture pattern due to the presence of bedding planes parallel to a stope	102
5.24	Ductile shear zone with en echelon micro cracks developed in PMMA under uni-axial loading (after Petit and Barquins, 1988)	103
5.25	Shear band with associated (surface) micro cracks in a bi-axial test on PMMA (after Petit and Barquins, 1988)	103
5.26	Results from uni-axial tests on marble plates (after Chen et. al., 1992)	105
5.27	Progressive formation of primary and secondary fractures around inclined slots in gypsum plates subjected to horizontal loading (after Shen, 1995)	105
5.28	Simulated fracture pattern around an inclined slot in a uni-axial stress field	106
5.29	Uni-axial load, tensile failure (FLAC)	107
5.30	Uni-axial load, perfectly plastic (FLAC)	107
5.31	Uni-axial load, gradual softening (FLAC)	108
5.32	Uni-axial load, rapid softening (FLAC)	108
5.33	Random mesh of Delaunay triangles used in simulations 5.34 to 5.45	109
5.34	Regular mesh of Delaunay triangles used in simulations 5.46 and 5.47	110
5.35	Perfectly plastic	110
5.36	Tensile failure	111
5.37	Hardening	111
5.38	Moderate softening, tensile strength 20MPa	112
5.39	Complete softening, tensile strength 20MPa	112
5.40	Complete softening, tensile strength 10MPa	113
5.41	Complete softening, tensile strength 35MPa	113
5.42	Complete softening, tensile strength 20MPa	114
5.43	Complete softening, friction angle = 20 degrees	115
5.44	Complete softening, flaws in the form of pores	115
5.45	Tensile failure, additional flaws	116
5.46	Perfectly plastic, regular mesh	117
5.47	Moderate softening, regular mesh	117
5.48	Tensile fracturing from multiple slots	118
5.49	Multiple slots, uni-axial loading	119

5.50	Development of en echelon fractures into a macroscopic shear fracture; punch-through shear test of mortar specimens (after Davies et. al., 1988)	120
5.51	Tensile fracture formation from notches in the punch-through experiment (DIGS result)	121 118
5.52	Simulation of the punch-through experiment with FLAC	124
5.53	Tensile stress distribution around the bottom notch in the case of non-linear elasticity	127
5.54	Fracture geometry in the punch-through experiment according to the Energy Criterion	128
5.55	Tessellation mesh used for the simulations of the punch-through experiment	129
5.56	Resulting fracture patterns; tensile strength = 20MPa, friction = 30 degrees	130
5.57	Same parameters as the model in 5.56, but the presence of tensile stresses results in brittle failure in this case	130
5.58	Resulting fracture patterns; cohesion before failure = 15MPa; friction angle = 30 degrees	131
5.59	Same parameters as the models in Figure 5.58, but the presence of tensile stresses results in brittle failure in this case	132
5.60	Resulting fracture patterns	133
5.61	Same parameters as the models in Figure 5.60, but the presence of tensile stresses results in brittle failure in this case	133
5.62	Results for relatively high friction angles	134
5.63	Same parameters as the model in Figure 5.62, but the presence of tensile stresses results in brittle failure in this case	135
5.64	Effect of a small perturbation in boundary conditions	136
5.65	Low friction angles; complete softening	137
6.1	DIGS simulation of shear fracturing ahead of an advancing stope face; Excess Shear Stress criterion	141
6.2	DIGS simulation of shear fracturing ahead of an advancing stope face according to the Energy criterion	142
6.3	FLAC simulation of failure in the abutment of an excavation	144
6.4	Cantilevering beam which is clamped on the left hand side	146
6.5	Theoretical and numerical (DIGS) values for stresses and displacements in a cantilevering beam	147
6.6	Theoretical and numerical (DIGS) values for stresses and displacements in a cantilevering beam	148
6.7	Axial stresses in the extreme beam elements (vertical axis) in relation to the step number in the iteration process (horizontal axis); numerical simulation with FLAC	149
6.8	A longwall stope half span in an elastic medium	150
6.9a	Bedding planes, spaced 2m.	151
6.9b	Bedding planes, spaced 2m.	151
6.10	Results of a DIGS simulation near a stope abutment	156
6.11	(tensile) Fracture formation due to the stress field induced by a stope in a layered medium as in the previous example	157
6.12	Effect of induced fracture coalescence	158
6.13	Effect of a joint set on mining induced (extension) fracturing	159
6.14	FLAC simulation of punching in a perfectly plastic material	160
6.15	DIGS simulation of punching in an elastic material	161

6.16	Elastic stress distribution around a stope	164
6.17	Stress distribution after activation of the first vertical discontinuity at the abutment	165
6.18	Stress distribution after 7 mining steps; no tensile fracturing simulated	166
6.19	Stress distribution after 7 mining steps, with generation of tensile fracturing	167
6.20	Development of horizontal tangential stresses in the skin of the stope due to the "ratchetting" mechanism of locked-in deformations	168
6.21	Vertical deformations at the skin of a stope for different scenario's	169

1 INTRODUCTION

1.1 GENERAL

A primary concern in mining operations in general is "ground control", i.e. control of the displacements of rock surrounding the various excavations generated by, and required to service, mining activity. Unlike many other engineering disciplines where the behaviour of structures under various loading conditions can be analytically predicted with great certainty, rock engineering has to rely to a large extent on empirical methods for various reasons. A major reason is the lack of control over material properties and loading conditions which are encountered in underground environments. In deep level mining, where stresses easily exceed the strength of the intact rock, an additional uncertainty is created, namely the behaviour of rock during and after fracturing.

Problems directly associated with high stresses and fracturing involve rockbursts and rockfalls, which account for a large percentage of fatal accidents occurring in South African gold mines, control of stoping width, which affects the economics of the mining operations, drilling difficulties, which are encountered in fractured rock, and the efficiency of rock breaking systems, which is directly related to the failure and post failure behaviour of the rock. Moreover, inelastic deformations and stress distributions around deep level mining excavations directly affect support requirements, the stability of hanging walls, the response to rockbursts and mining operations such as drilling, rock breaking and even transport.

At present rock mechanics engineers on South African gold mines use a design method in which the rock mass is assumed to behave elastically. In combination with the Energy Release Rate (ERR) concept (Cook, 1967 and Salamon, 1974), this method allows the engineer to determine the seismic potential associated with a particular mining lay-out. Although it is recognised that the fractured rock around a mining excavation has a major effect on the actual stress distribution, deformation and energy dissipation, no rational design method, which incorporates these effects, has yet been implemented. The engineer is still left with empirical rules and "engineering judgement" in combination with a very basic, crude and incomplete design method. Although the rock beyond the fracture zone may behave elastically, it is the fractured zone around the excavation which really controls the behaviour of the rock mass in the mining environment.

Previous research has provided understanding of fracture processes in general, the fracture pattern around typical deep level mining excavations, deformations in and around fractured rock, the stresses, forces and deformations induced in support structures etc. However, even with all this information, it has not been possible to develop a rational design method which includes the fundamental behaviour of brittle rock during and after failure. Observed behaviour is mostly insufficiently analysed, often because adequate numerical tools are not available to test proposed mechanisms and/or constitutive laws. During more recent years more powerful computer programs have become available and, together with further developments in the understanding of (brittle) rock fracturing, this enables rigorous and critical examination and identification of potential failure mechanisms and constitutive laws. The adjective "brittle" is used throughout this thesis to indicate a reduction in strength during the failure process. The conditions under which failure takes place will

determine to a large extent if such a reduction in strength (softening) takes place in a particular material.

The observed behaviour around underground excavations is generally very difficult to interpret because the detailed history of a particular site is often unknown. Geological processes may be inferred from specific observations on discontinuities, but the results most often lack sufficient detail to be useful for modelling purposes. The identification of geological discontinuities is obscured by the potential for stress or mining induced fracturing; it can be extremely difficult, if not impossible, to distinguish between (re-activated) joints and pure mining induced fractures. The exact causes of mining induced fracturing are also not always identifiable as the local static stress field is unknown and the effects of blasting and seismic activity are unspecified and mostly undetectable. This scenario leaves too many options to explain observed behaviour although numerical models can be and have been used to analyse some of these options.

For the purpose of this research the results of relevant laboratory experiments have been used as they provide a better opportunity to investigate fracturing and damage processes under more controllable conditions. Numerical models simulating such experiments have been analysed in order to identify fundamental failure mechanisms. The failure mechanisms thus identified are used to explain observed behaviour around underground excavations in deep level gold mines.

1.2 OBSERVATIONS AROUND DEEP LEVEL EXCAVATIONS

Detailed fracture mapping of areas which are exposed ahead and behind advancing longwall faces has been done by various researchers (Adams et. al., 1981; Brummer, 1987; Kersten, 1964; Leeman, 1960; Legge,1984; Joughin and Jager, 1983; Roering, 1978). In general there appears to be agreement about the nature of fracture formation in the highly stressed region ahead of a stope face.

Two types of mining induced fractures are identified; namely extension fractures and shear fractures. Extension fractures are defined as discontinuities which lack any evidence of shear displacement across their surfaces and which appear to be aligned with the direction of the major principal stresses. Shear fractures are defined as complex macroscopic features which comprise many closely spaced extension fractures. Relative lateral movement between the intact rock on either side of the macroscopic shear zone causes crushing of the material inside this shear zone which allows for easy identification. The width of a typical shear zone can range between 5mm and 500mm. Shear fractures have been observed to occur deeper into the solid than extension fractures which only seem to form within a few metres of the stope face.

The shear fractures are typically separated by areas of intact rock further ahead of the stope face, while closer to the stope face extension fractures are formed in the intact rock between shear fractures. Shear fractures are found to be aligned along two complementary directions with respect to the vertical direction, effectively forming a pattern of wedges ahead of the mining excavation. These observations are reported as typical for deep level gold mining and the absence of shear fractures should indicate lower stress levels or more competent rock. It should be pointed out that the occurrence of shear fractures has not

frequently been observed by the author and many of his colleagues and they certainly appear far less common than suggested by researchers such as Brummer (1987) and Legge (1984). The subject of shear fracture formation therefore requires careful analysis in order to obtain a realistic picture.

Horizontal movement of rock material ahead of the stope faces towards the excavation is typically observed (Brummer, 1987 and Legge, 1984). This movement is in fact in opposite direction than that predicted by elasticity theory and can therefore be totally attributed to inelastic deformation processes. Legge (1984) reports that three types of behaviour with respect to this horizontal dilation were observed; sometimes dilation initiated along the shear fractures, sometimes dilation could only be associated with the extension fractures, or, on rare occasions, no dilation could be measured at all. In the last case no fractures were present in the rock, which is then classified as a "hard patch". Typically, however, approximately 70 per cent of the movement occurs within 1.5m from the face while the remainder is absorbed within a distance of 6-7m ahead of the stope face. The presence of dip gullies was found to have a pronounced effect on the horizontal dilation occurring ahead of the stope faces. Dip gullies which were cut into the footwall near the stope face allowed for additional dilation into the footwall. Relative movements (slip) of up to 25mm were observed across parting planes close to the stope face. These movements are assumed to have two effects; firstly energy is dissipated due to frictional resistance and secondly the magnitude of horizontal stresses acting on the immediate stope face area will be reduced. Reduction of horizontal stresses (confinement) is reported to reduce the ability of the fractured rock ahead of the stope face to sustain vertical load, which is then transferred to rock further ahead, causing extended failure. (Herrmann, 1984) In one case a relative movement of 600mm was observed in the footwall with respect to the hangingwall where a dip gullies were present. In a case where no dip gully was present it was observed that the footwall buckled upward into the stope, also indicating the presence of large horizontal deformations and associated compressive stresses.

The dilation ahead of the stope face is assumed to induce compressive stresses in both hangingwall and footwall strata. This mechanism is most likely accommodated by the presence of parting planes and movements along these planes were found to occur well into hanging- and footwall strata. Boreholes drilled into these strata showed stepwise shearing, which is thought to be associated with bedding plane slip (Joughin and Jager, 1983; Legge, 1984; Brummer, 1987). Slip across shear zones, including the observed shear fractures, was not generally associated with rock bursts by these researchers, but was found to develop in a stable fashion. However, the opposite has also been reported by Ortlepp (1984), namely that some rockbursts have been found to be associated with mining induced shear fractures. Ortlepp refers to these shear fractures as "burst fractures" and claims that this type of fracturing is commonly observed ahead of stopes that have suffered a rock burst. Based on these observations, it is arguable that both stable and unstable formation of shear fracturing is possible. In one particular case shear slip of approximately 200mm along a shear fracture was observed ahead of a mining face by Brummer (1987). While such deformations may easily explain the associated dilation towards the excavation, it is difficult to visualise how such large shear deformations can be absorbed inside the rockmass. Either the total length of the shear fracture must be excessive in order to accommodate and generate such large displacements in an otherwise elastic medium, or these displacements must be associated with extremely large plastic deformations in the

rockmass itself. It is not clear from the observations which scenario is more likely, although it appears that plastic deformations would be the most plausible explanation considering the fact that no violent failure has been observed in that case.

The discrepancy between measured convergence and elastic convergence is explained by many researchers as being caused by bedding plane separation. This explanation may however not be complete as in some cases dilation of the hangingwall strata was measured while no bedding planes could be detected. The effect of support pressure on stope convergence has been investigated by Herrmann (1987), who claimed that support pressures of up to 0.4MPa did not have a noticeable influence on such convergence. This observation is quite significant as it indicates that the inelastic deformations are not merely caused by the weight of the immediate hangingwall. A support pressure of 0.4MPa would be sufficient to carry the weight of approximately 15m of rock. In other observations however, the support resistance has been found to influence the deformation around typical deep level longwall stopes, but these observations were done in either waste filled or backfilled stopes and the associated pressures were most likely significantly higher (Legge, 1984)

Measurements of rock displacements behind the stope face, directly above and below the longwall stope, revealed that further mining had a relatively small effect on the vertical dilation in either hanging- or footwall (Legge, 1984). This observation indicates that the inelastic deformations which contribute to the stope convergence either occur ahead of the stope face, in the unmined region, or very close to the stope face, in areas which were not monitored by instruments. Dilation normal to the strata has been measured in hangingwalls and although (elastic) relaxation of vertical stresses obviously also affected the results, inelastic localised dilation and contraction was observed in individual bore holes. Overall dilation occurred until a certain distance behind the face, where a maximum value was reached. After that, overall contraction was initiated, supposedly due to the activated support pressure of rock fill. The observations indicate that dilation normal to the strata takes place fairly uniformly across the stope and is associated with the opening of bedding planes. This opening is related to slip which is mobilised along favourably orientated discontinuities ahead of, or close to the stope face and the normal dilation is reversible by moderate support pressures. Similar measurements in the footwall strata resulted in shearing of the boreholes, thus preventing further observations. The shearing is associated with large deformations in the strike direction. Measurements of such deformations showed compaction in both hanging- and footwall behind the stope face. These deformations are related directly to similar dilatory deformations which take place ahead of the stope face.

A very revealing observation is the deformation profile across backfill panels in relation to the stresses measured inside these panels (Gurtunca et all.,1990). Until the stresses inside the backfill reaches values of about 1MPa, the deformation profile is fairly uniform across the backfill panel and the adjacent strike gully. As soon as the stresses in the backfill panel exceed the 1MPa limit differential closure between the hangingwall immediately above the gully and the hangingwall above the backfill panel is initiated. This difference increases to approximately 200mm, at which stage the backfill stresses reach values of about 3MPa. As the area above the gully does not experience the effect of support pressure, the difference in closure can be associated directly with the effect of support pressure This behaviour has

been observed in a variety of longwall stopes and may be considered representative. An explanation for these observations may be that the previously dilated hanging- and footwall strata are being compacted by the support pressure. The resistance of the strata against these reversed inelastic deformations is approximately 1MPa and when subjected to higher stresses, the previously dilated rockmass is increasingly compacted. A secondary effect of increased vertical support pressure is the induction of horizontal compressive stresses into the hangingwall. This may increase the stability of the hangingwall, as many potentially unstable blocks could effectively be pinned by such horizontal clamping stresses.

A possible explanation for this behaviour is that the inelastic deformations are associated with shear deformations along favourably orientated discontinuities in both hanging- and footwall. The vertical dilation of the strata is thus directly induced by the horizontal stresses generated ahead of the stope face. A balance between these horizontal stresses (which in turn are associated with horizontal dilation due to excessive vertical stresses) and the vertical dilation of hanging- and footwall strata can apparently be affected by support pressures in excess of 1MPa, as such pressures do result in a (re)compression of the strata.

In an experiment by Herrmann (1987), a hydraulic barrier prop was used to apply a load onto the fractured hangingwall to measure the induced stresses inside the hangingwall in response to the applied loading. The first 200KN of load where associated with an increase of measured compressive stresses, but further loading resulted in the measured stresses approaching an asymptote of constant stress. Herrmann explains the limit in measured stresses being due to limited frictional resistance along activated discontinuities, while the increasing load results in the activation of a larger number of discontinuities. In other words the stresses remain constant, but the area subjected to stress increases. Relaxation of the applied load only resulted in a partial relaxation of the induced stresses. Deformation measurements around the active support load indicated relatively large upward movements at one location, whereas at other locations smaller downward movements were observed. Herrmann attributes this behaviour to wedging and dislodging respectively.

In other experiments, Herrman (1987) investigated possibilities of influencing the orientation of mining induced fracturing. As the orientation of these fractures is believed to influence the stability of the affected hangingwall, such a possibility could be of practical use. The cutting of dip parallel hangingwall slots caused a relaxation of horizontal stresses. This reduction in compressive stress was found to lead to a steeper inclination of mining induced extension fractures in the immediate hangingwall strata when a relatively low support resistance of 0.1MPa was applied. In the case of a larger applied support pressure of 0.4MPa it was found that even without the hangingwall slot, extension fractures assumed a relatively steep orientation and the cutting of a slot did not influence fracture orientations. Herrmann reports, however, an improvement in hangingwall stability due to the slot cutting for both support systems, but especially for the softer one. Both the support action and the horizontal stresses in the hangingwall are assumed to affect the orientation of the mining induced fractures due to their influence on the stresses ahead of the stope face, where these fractures are assumed to initiate.

As the region between the last row of hydraulic support units and the 1.2m deep hangingwall slot was left unsupported in the experiments described above, back area

hangingwall collapse occurred with further stope face advance. In the case of the higher resistance support system a cantilevering hangingwall beam was left projecting over the back area. At intervals this beam broke off at the last row of supports and separated along a bedding plane. On average, this beam was approximately 5m long and 0.5m high at the moment of collapse. In the case of the softer support system the hangingwall collapsed to a height of 1m immediately behind the last row of support units, resulting in a typical 'caving stope' operation. The lower vertical confinement provided by the weaker support system is assumed to allow for an increased potential for block separation. It is also assumed that the support induces horizontal dilation, similar to the observations with the active support element. Reduced stability is explained due to a lack of clamping force combined with an increased potential for block formation. The effect of cutting a slot was similar for both support conditions, namely an initial relaxation of stresses followed by re-compression in those layers which were intersected by the slot. The immediate hangingwall layer experienced lower stress changes than the second layer, further inside the rock. This difference is explained by the higher fracture density in the first layer which effectively reduces the stiffness of the local rockmass. The difference between the high and low strength support system was only observed in the immediate hangingwall layer. With the high strength, 0.4MPa, support system, re-compression of this layer occurred more rapidly than with the 0.1MPa support system. This increase in re-compression is assumed to be caused by the larger confinement produced by the stronger system. The fact that the difference in support resistance only affected the measurements in the immediate hangingwall layer suggests that the stronger support system has little additional influence on the rest of the hangingwall strata over the weaker support system.

1.3 CURRENT DESIGN PRACTICES

The failure of rock itself and the inelastic deformations associated with geological discontinuities are not directly analysed for conventional design purposes. The elastic stress distribution around mining excavations is commonly computed and used to determine the relative failure potential in a particular situation. The concept of excess shear stress (ESS) is used to evaluate the extent of possible shear slip along potential discontinuities within areas subjected to excess (shear) stress. Large values of excess shear stress are associated with the potential of relatively large seismic events and are therefore undesirable. In a similar fashion the concept of energy release rate (ERR) is used to compute the relative magnitude of stresses at the abutments of mining excavations and across pillars. These stress levels are directly associated with the failure potential of such locations and the designer must limit the values below a certain critical level by adjusting mining lay-outs and pillar dimensions.

Although it is accepted that inelastic deformations and stress relaxation processes affect the stress distribution and the associated failure processes around highly stressed excavations, there is at present no alternative design methodology which fully incorporates these effects. The presence of major structures such as dykes and faults is often directly considered in the design of mining lay-outs. These structures can offer a potential source of seismic action and the mining lay-out is adjusted accordingly. The effect of inelastic deformations is also considered in the design of support systems which have to accommodate and/or employ relatively large deformations associated with inelastic behaviour. Although these examples demonstrate that inelastic mechanisms are recognised

and addressed to a certain extent, the effects of fracturing and shear slip around highly stressed mining excavations have much wider implications, which are not considered at all. Many inelastic deformation processes are "a-seismic" and can result in stress distributions which differ substantially from the elastic situation. Design based on the assumption of an elastic stress distribution is therefore highly questionable.

Relaxation of stresses in the abutments of highly stressed excavations can be observed and can be attributed to load shedding due to fracturing and slip along discontinuities. The effect of such a stress redistribution on a parameter like ERR can be substantial and should be considered in order to obtain a realistic estimate of the potential for (kinetic) energy release. Of similar importance is the effect of the inelastic deformations on the mechanisms of energy release. Depending on the nature of the inelastic deformation mechanism, energy can be released in a dynamic, violent fashion or not. Cases of stable, non violent deformation may not be comparable to cases in which a relatively large percentage of the energy is released in a violent way. It is therefore important to understand both the mechanism of inelastic deformation as well as its effect on the stress distribution, in order to derive at an efficient design.

The nature of fracturing will to a large extent determine the detailed geometry of a particular hangingwall. This has immediate implications for local support design as the stability of the hangingwall needs to be ensured. It is therefore of importance that the local fracturing processes are taken into account for this purpose. The typical presence of compressive stresses in the immediate hangingwall and footwall of longwall stopes can only be explained from inelastic deformation mechanisms and has major implications for support design as well. It is again important that the presence of these stresses is considered.

Other effects which can be associated with the fractured and damaged skin around deep level excavations are large deformations into the excavation, modification of incoming seismic waves, punching into the skin, local instabilities, etc. These effects directly influence support requirements and are not taken into account in any elastic analysis. The detailed inelastic behaviour of the fractured and damaged skin has to be considered in order to accommodate or affect such behaviour. Current design practices only address certain aspects of inelastic behaviour and do not cater for all of them.

1.4 MOTIVATION AND OUTLINE OF PRESENT RESEARCH

While it has become clear from previous research and underground experience that inelastic deformation processes play a dominant role in deep level mining, such processes are still poorly understood. The interpretation of many underground observations is often based on personal intuition combined with a certain amount of (logical) reasoning. This situation is unsatisfactory as it does not result in an objective evaluation of the situation.

One of the main problems in achieving such an objective evaluation is the fact that rock failure and post failure are still not satisfactorily described by any constitutive model. Major research efforts have been made to address these issues in the past and many successes have been claimed and even achieved, but the failure of rock is still an ill described phenomenon. Well established theories such as fracture mechanics and plasticity

have been and are applied to represent the failure and post failure behaviour of rock with varying success. When rock is subjected to compressive stresses, as is common in mining operations, large differences between predicted and observed behaviour can be noticed. As it is believed that the underground situation can only be correctly interpreted if the processes of rock failure are properly described, it was decided to first analyse these processes in more detail in this thesis.

The applicability of both fracture mechanics and plasticity have been investigated with the use of appropriate numerical models. The numerical model results were subsequently compared with laboratory test specimens of rock, which had been subjected to similar conditions as their numerical counterparts. The limitations of both theories could clearly be identified by these comparisons. By using a variety of numerical techniques, particular numerical shortcomings could also be detected. The validity of the assumptions which form the basis of the various models has been investigated as well.

The theory of fracture mechanics is treated in Chapter 2 and the application of this theory to the fracturing of rock, subjected to compressive stresses, is addressed. Initially, the fracturing around openings in compressed rock is analysed and it is found that many observations can be explained directly with the use of this theory especially if the concept of flaws is adopted. In conventional fracture mechanics, failure is usually assumed to take place in tension. Using this convention, shear fracture formation can not directly be reproduced by the numerical models, although a large variety of extension fractures were simulated.

Plasticity has been applied in order to represent the failure of rock on a global scale. While it is understood that many of the micro mechanical processes which control failure are not explicitly represented by plasticity, the theory offers a convenient means of simulating inelastic deformations, peak stresses and post failure behaviour. Failure localisation in the form of shear bands is a logical extension of the theory of plasticity and the possibility of representing shear fractures by shear bands is investigated in Chapter 3. Numerical problems associated with failure localisation resulted in unsatisfactorily simulations and the suitability of the theory could not properly be established. It remains questionable whether the theory of plasticity can capture the micro mechanical processes which are assumed to control the failure of rock on a macro scale.

As an alternative to the theory of plasticity and the conventional application of the theory of fracture mechanics, the possibility of an alternative fracture criterion has been investigated in Chapter 4. Instead of excess tensile stresses at the fracture tip, criteria which are either based on excess shear stress or maximum energy release have been used to determine the direction of fracture propagation in the numerical models. While it is possible to obtain results which appear realistic, this approach must be regarded as highly empirical. The fundamental processes of large scale fracture formation, which are most likely related to the growth and coalescence of micro fractures, are not considered by this alternative and the assumption of a propagating shear fracture may be misleading.

Results from laboratory experiments are presented and discussed in Chapter 5. Numerical simulations of these experiments have been used to test the potential of various approaches. As an alternative to the previously mentioned models, the application of so

called tessellation, or random grid schemes have been investigated. While the use of interacting flaws in numerical models normally leads to numerical problems, this has been overcome to a large extent by the application of tessellation schemes in which potential fracture paths are predetermined. As these models allow for a more natural representation of rock failure, their results have been analysed in detail in order to determine the global response. It was found that the resulting global fracture patterns could in principle be interpreted as either extension or shear fractures, although the formation of fully developed shear fractures, with large scale shear deformations and associated crushing, cannot be represented by these models. The fact that the models are two dimensional simulations of three dimensional micro fracturing processes must also be taken into account.

While the tessellation models appear to allow for the most natural representation of rock fracturing processes, it is not clear if the resulting large scale fracture patterns can immediately be compared with observed fractures. The influence of the third dimension and large deformations has not been investigated yet, while the density of flaw distribution and the effect of opening size also have to be analysed. Larger models are required for such simulations and it is expected that future research will address these issues. The results which are shown in this thesis do however indicate the potential of this approach with respect to the simulation of large scale fracture formation in brittle rock subjected to compressive stresses.

Practical applications with direct relevance to the fracturing around typical deep level mining excavations are finally presented in Chapter 6. The effect of geological discontinuities such as bedding planes on the stress distribution is analysed with the use of numerical simulations and numerical problems associated with the representation of beams are demonstrated and discussed. The concept of locked-in deformations and the associated effect of loading (or mining) history on the distribution of stresses around a longwall stope is used in another analysis to demonstrate that conventional single step numerical simulations may not be correct in cases where inelastic deformations occur. The assumptions in that particular analysis are that shear deformations take place along steeply inclined discontinuities. The mechanism of punching has been analysed as well, with the use of various numerical models, and it is shown how each of these models can be used to produce the most realistic results.

In the conclusions the findings are summarised and the applicability of the various numerical techniques is discussed. The focus is on the nature of large scale fracture formation and its effect on failure of the rock mass. Recommendations for further research into these fundamental aspects of mechanical behaviour o rocks are given and the limitations of this particular research and the current status of failure representation are pointed out.

2.0 APPLICATION OF FRACTURE MECHANICS TO ROCK FRACTURING

2.1 INTRODUCTION

The use of fracture mechanics would appear to be the most suitable approach for describing the processes which control the fracturing of rock. The fact that only limited success has been achieved with the application of fracture mechanics in the field of rock mechanics may therefore seem to be illogical. The successful application of fracture mechanics to a wide variety of engineering materials is to a large extent related to the fact that such materials are subjected to tensile loading, which allows for a direct analysis. Failure and fracturing around deep level stopes is assumed mainly to be associated with compressive stresses as horizontal stresses in typical deep level stope hanging and footwalls have been observed to be compressive (Legge, 1984). This should not necessarily exclude the presence of tensile stresses at any location, but tensile stresses are often inferred to be absent.

Brittle failure always occurs through a tensile mechanism and the stress required to initiate the first fracture is also the stress required to fail the (brittle) material under tensile stress conditions. Geological materials, however, are more often loaded in compression, which results in a far more complex fracturing process. The theories of brittle fracture in compression are all based on a model introduced by Griffith (1924). Three fundamental assumptions are associated with this model:

(1) Brittle fracture is initiated from a microscopic flaw (the Griffith crack), and the process is controlled by the elastic stress field around the flaw.
(2) The material surrounding the flaw is an elastic, homogeneous and isotropic continuum containing no further imperfections.
(3) Individual flaws are spaced widely enough from each other so that the stress distributions associated with them do not affect each other.

Two additional assumptions are common to all these theories:

(1) Fracture extension occurs from tensile stress concentrations.
(2) Fracture is initiated when the maximum tensile stress concentration, occurring on a critical flaw boundary, reaches the tensile strength of the material surrounding the flaw.

Although compressive stress concentrations will be substantially higher than the tensile stress concentrations in a compressive stress environment, their effect on fracture initiation is completely ignored according to the first additional assumption. The size effect is not considered as can be appreciated from the second additional assumption. Only the stresses at the flaw boundary are accounted for and the discontinuous nature of the surrounding material, which contains its own natural flaw system at a scale which may be smaller than that of the critical flaw, is not accounted for. The Griffith criterion only addresses fracture initiation which does not imply that fractures will propagate to sizes which can be observed. This issue becomes relevant under compressive loading conditions where fracture propagation can be stable and fracture initiation is not necessarily associated with failure as it would be under tensile loading conditions.

In a series of experiments on uni-axially loaded specimens which were made of plaster of Paris, Lajtai (1971) investigated fracture growth from artificial flaws of varying dimensions and orientations and compared his observations with the theoretical strength as predicted by the Griffith criterion in order to assess the applicability of that criterion under compressive stress conditions. Although Lajtai mentions the fact that certain fractures may be initiated, but do not sufficiently propagate to become noticeable, he reports no agreement between his *observations* and the predictions of the Griffith theory with respect to the fractures which can be detected. Where the Griffith criterion does not predict a size effect, the observations indicated a very strong size effect. Only the larger circular flaws (diameter 25mm to 50mm) induced fractures at stress levels which approached theoretical values, while for instance an opening with a diameter of 10mm only induced a fracture at an applied stress of approximately five times the theoretical value.

A similar pattern was found by Lajtai (1971) with elliptically shaped flaws, whereby instead of the diameter of the opening, the length of the flaws was varied. In that series of experiments the orientation of the flaws with respect to the direction of loading was also varied. It was found that the flaw orientation most conducive to fracture growth was such, that the loading was perpendicular to the long axis of the flaw. This effect was more pronounced for the smaller flaws than for the larger flaws, which again must be attributed to a size effect. The most critical orientation according to Griffith's criterion is however the orientation at which the angle between the flaw and the direction of loading is 30 degrees, where the tensile stresses reach a value which is approximately three times higher than the value of the maximum tensile stresses which are generated around a flaw which is orientated at 90 degrees with respect to the direction of the load. It is obvious that the experimental results did not match the theoretical Griffith values.

Lajtaj (1971) explains his observations by proposing that the magnitude of the theoretical stress concentrations is less important than the size of a particular flaw. This size effect is attributed by him to the shape and size of the tensile zone which occurs around the flaw and which consequently is the critical parameter controlling tensile fracturing from a single flaw in a compressed medium. Failure initiating from areas where compressive stress concentrations occur was also observed in the form of intense crushing; the fractures associated with this mechanism have been termed shear fractures although this term refers to complicated structures involving combinations of shear failure and tensile fracturing. Lajtai observed that tensile fracturing did not have a large effect on the ultimate failure of the specimens. Failure was associated with shear fracturing, which in turn may be associated with the interaction processes between multiple flaws. These findings point to the unsuitability of (conventional) fracture mechanics to represent brittle failure in a compressive environment.

Under uni-axial loading conditions the unstable propagation of a tensile fracture from a single flaw is in theory possible if plane strain or stress is assumed. However, as soon as a confining stress is applied, fractures will stabilise after limited propagation and, in the case of a three dimensional flaw, fracture propagation will be limited even under uni-axial loading conditions. Gramberg (1970) reports however that tensile 'splitting' fractures can develop under conditions of uni-axial loading and even under conditions where small amounts of confinement are present in brittle materials. Although such observations are often reported, it should be appreciated that it is often impossible to ascertain the exact

boundary conditions and the loads which are induced in a particular specimen when laboratory experiments are concerned. Nevertheless Gramberg (1970) points at some other shortcomings in Griffith's theory as applied to compressive loading conditions, namely the assumption that very flat, open ellipses are present, that the direction of fracture propagation coincides with the major axis of the ellipse (which has its critical orientation at 30 degrees from the direction of the major principle stress) and that the apex point of the flat ellipses is shaped according to the analytical description of an ellipse. These assumptions are incorrect because (1) a flat ellipse cannot remain open under compression (see also McClintock and Walsh, 1962), (2) tensile fractures propagate in the direction of the major principle stress and not oblique to it and (3) a realistic fracture tip should have a cusp- or beak-shaped notch rather than the assumed elliptical shape.

Gramberg (1989) continues to propose a mechanism which allows brittle fracturing to take place in a compressive environment by a combination of an ellipsoidal flaw with a cusp shaped fracture tip. Fracture propagation is assumed to take place by a transformation process in which the relatively narrow cusp shaped tip rapidly changes into an ellipse which is orders of magnitude wider than the fracture tip. This relatively large width at a distance close to the fracture tip is required in order for tensile stresses to be induced at the fracture tip by the major principal stresses which are aligned along the major ellipse axis. Gramberg explains that the fracture tip occurs at an atomic scale and that the excessive widening is possible due the relaxation of atomic bonding stresses. This proposed mechanism is not based on solid theory and lacks evidence in the form of fracture tip observations. It is mainly driven by the assumption that tensile fracturing can take place from a single flaw in an all compressive stress environment. An alternative explanation can be found in the boundary conditions and associated stress distributions. It is possible that local tensile stresses are induced near the boundaries, due to irregularities at the interface between specimen and loading platens. For the purpose of this thesis Gramberg's theory is not applied and it is therefore assumed that tensile fracturing can only take place in response to excessive (local) tensile stresses, induced at different scales by geometrical and structural effects.

The microstructure of rock will most certainly lead to an internal redistribution of global stresses in such a way that local tensile stresses can be induced even if the global stress field is all compressive. Micro fracturing in brittle rock is assumed to result from excessive local tensile stresses . The initiation of micro fracturing is however neither associated with permanent strain nor with material failure when global tensile stresses are absent. Failure under compressive conditions only takes place at increased stress levels after the initiation of micro fracturing and is most likely associated with interaction processes between previously formed micro fractures and probably involves a shear deformation mechanism. The application of fracture mechanics becomes highly questionable under these circumstances, although attempts have been made to represent large scale shear fractures as single fractures which propagate according to an alternative failure criterion such as an excess shear stress criterion (Shen, 1995). Such criteria are highly empirical and it is even questionable if so-called shear *fractures* can be represented by individual fractures. This subject is quite relevant to the situation around highly stressed deep excavations in brittle rock where failure and fracture is expected to take place under similar loading conditions and the presence of shear fractures is often reported.

A more detailed treatment of shear fracturing is given in chapter 4. Interaction processes between (micro) fractures are described in the literature but mainly deal with a two dimensional representation of flaws and fractures. A more realistic three dimensional treatment is obviously far more cumbersome, but also leads to different results. In experiments on brittle polyester specimens in which penny shaped flaws were created using a laser and a focusing lens Germanovich et. al. (1996) found that single flaws could only generate wing-like cracks of a size comparable to the flaw size, even when the load reached the compressive strength of the material. In specimens which contained a relatively low density of artificial flaws, failure occurred in a burst like manner at stress levels close to the uni-axial compressive strength of the material. Specimens with higher flaw densities failed due to vertical splitting at relatively low stresses. Analysis of the stress distribution around an inclined penny shaped flaw subjected to uni-axial compression confirmed the limited potential of penny shaped flaws to generate large cracks, which points to the importance of interaction between multiple flaws and cracks for large fracture generation. Dyskin et al. (1994) report that even two neighbouring flaws can produce large cracks which tend to split the specimen under uni-axial loading conditions. Although the underlying mechanism could not be described exactly it was suggested that micro-scale flaws generate tensile stresses which are the driving force for large scale fractures.

Although the initial development of a 3-D flaw is substantially different from a 2-D flaw, the effect on the resulting large scale fracture may be described in a similar manner, namely a concentrated internal pressure. This may justify the application of 2D models for the simulation of fracture propagation. While such models allow for a far simpler approach, they may still be able to capture the essential mechanism, namely the internal pressurisation from a micro flaw. In section 2.3 brittle micro fracturing and interaction processes are analysed with such two dimensional models. While pure brittle fracturing excludes any form of plastic deformation, plasticity has initially been treated separately from fracturing in this chapter. It will become clear however that neither a purely brittle fracture model nor a model which merely allows for plastic deformations is appropriate to represent failure in a typical rock material. Only by allowing an appropriate combination of plasticity and brittle fracturing can a realistic model be expected. Based on this combination model, the following models are presented in this thesis:

- a strain softening approach using plasticity theory (chapter 3)
- the use of alternative fracture criteria (chapter 4)
- the use of a shear failure criterion within a tessellation approach (chapter 5)
- sliding flaws and brittle, tensile fracturing within a tessellation approach (chapter 5)

The advantages and disadvantages of each of these alternatives are discussed in the relevant chapters. Only the last one of these alternatives is assumed to be a direct representation of micro mechanical processes leading to micro fracturing and micro fracture coalescence. The basis of this model is the sliding crack with wing crack as proposed by Brace and Bombolakis (1963). This model has been adopted by many subsequent researchers in different forms. Most of the applications of this model have been in the form of indirect constitutive laws based on the model, whereas the direct application of the model has never resulted in realistic simulations of macroscopic rock fracturing processes. This may be due to limitations imposed by the numerical tools used to produce

these simulations, although this is not always indicated or explained. The other potential alternatives listed above are not intended to represent micro mechanical processes directly, but are only designed to capture larger scale failure phenomena.

2.2 NUMERICAL MODELING OF BRITTLE FRACTURING

In order to simulate and analyse brittle fracture processes, numerical methods have to be used as closed formed solutions are not available. In this section such a numerical method is introduced and tested against basic cases of opening mode (mode I) and shearing mode (mode II) fracture initiation. The fracture initiation criterion which is being applied is commonly used and well accepted; namely the maximum tangential tensile stress near the fracture tip. An elastic stress distribution is assumed around the fracture tip and although the stresses at very close proximity to fracture tips reach theoretical values which approach infinity, this problem is avoided in the numerical model by calculating stresses at so called collocation points which are located away from the element ends and thus also from the fracture tips. While a process zone such as proposed by Dougill (1976) is not represented by the numerical model, the problem of a stress singularity is effectively avoided.

The numerical programme DIGS (Displacement Interaction and Growth Simulation) is a two dimensional Boundary Element (Crouch and Starfield, 1983) programme which is designed to represent and simulate brittle fracture initiation and growth by analysing the (elastic) stress distribution around fracture tips or at potential seed points and applying a particular fracture extension criterion to decide if and in which direction a fracture should propagate. Fracture extension is accomplished by adding a segment of specified length to the fracture tip or by placing such a segment at selected seed points (Napier, 1990; Napier and Hildyard, 1992). The process of analysing stress distributions and deciding if fracture initiation and/or growth should take place continues until a stable situation is obtained at which no further segments need to be added. The opening and/or sliding displacements along each element are allowed to vary linearly and the stresses around the fracture tip are evaluated on a circle with a radius which is related to the size of the segment containing the fracture tip. This radius can be specified by the user but its default value is 14.6% of the segment length, which is equal to the distance of the collocation points from the segment end (Figure 2.1). The linear displacement variation does not allow for cusp like fracture tip profiles such as suggested by Barenblatt (1962) for instance and exact fracture tip behaviour is therefore not claimed to be represented.

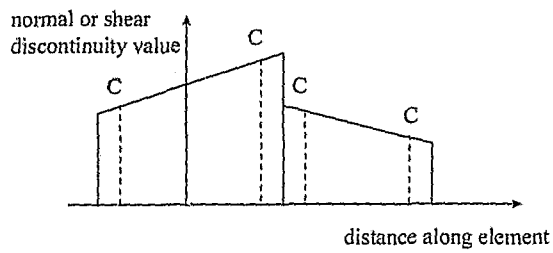

Figure 2.1 Illustration of two linear variation displacement discontinuity elements used to represent normal or shear discontinuities in DIGS; C refers to the collocation point positions within each element. No effort is made to enforce continuity between adjacent elements

The method can best be described as a "cellular" model, in that the values calculated at the collocation points must be regarded as representative average values for a particular discrete segment, rather than point values in a continuum. Satisfactory results are obtained except when fracture tips intersect other discontinuities at shallow angles (less than 20 degrees), or when two cracks overlap one another in close proximity. (Figure 2.2)

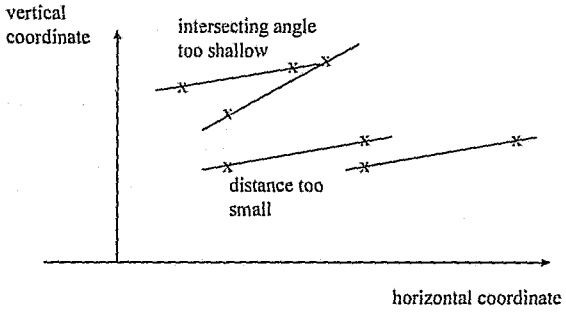

Figure 2.2 Discontinuity interactions that can lead to numerical instabilities

In this section the only fracture criterion which has been considered is a critical value for the tangential tensile stress along the selected circle around the fracture tip (figure 2.3). This fracture criterion has been widely accepted as suitable for brittle fracturing and is further referred to as the tensile (T) criterion. In order to access to suitability of DIGS for simulating mode I fracturing, the following numerical experiment has been conducted. A flaw of varying length has been placed in a tensile stress field . The flaw size was increased by adding additional segments until unstable fracturing is initiated. If the segment size is 1 unit, the tensile stress 1 unit and if the critical tensile strength is set to 10 units, the critical flaw size was found to be 47 units. The theoretical length, according to linear elastic fracture mechanics, can be derived from

$$\sigma_{\theta\theta} = \sigma\left[\frac{x}{\sqrt{x^2 - c^2}}\right] \tag{2.1}$$

whereby 2c is the flaw length, x is the distance from the centre of the flaw along the flaw direction, $\sigma_{\theta\theta}$ is the tangential stress and σ is the field stress. (Figure 2.3)

Rewriting equation 2.1 by using the distance from the fracture tip, r, to replace x by $(r + 2c)$ and assuming near crack tip conditions, it follows that

$$c = 2r\left(\frac{\sigma_{\theta\theta}}{\sigma}\right)^2 + O\sqrt{r} \tag{2.2}$$

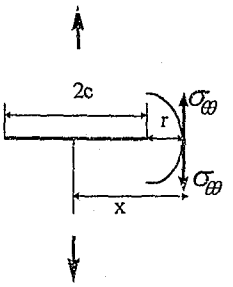

Figure 2.3 tangential stress directly and immediately ahead of a crack tip

With a critical tangential stress of 10 units, an applied stress of 1 unit and a distance r of 0.146 units, it follows from (2.2) that the theoretical value for the critical flaw size, $2c$, is 58 units. The difference between this theoretical value and the numerical value is explained by the fact that the crack tip is represented by a linear shape function in DIGS. Figure 2.4 shows the theoretical and the numerical stress distribution ahead of a flaw with a length of 100 units subjected to a hydrostatic tensile field stress of 1 unit.

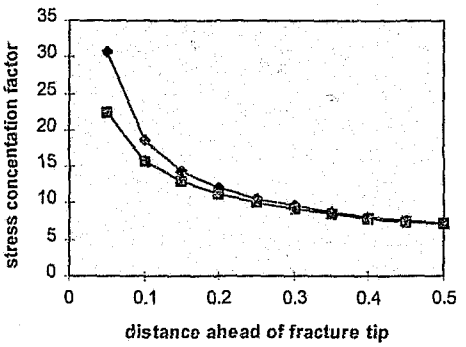

Figure 2.4 Numerical (top) and theoretical (bottom) values for the tangential stresses ahead of a flaw with a length of 100 units in a hydrostatic tensile stress field

It is clear from this figure that the numerical values deviate from the theoretical values at relatively small distances from the fracture tip. The values for the critical flaw length are even more affected as they are directly related to the square of the stress values (equation 2.2). The fact that stress values are assessed at a short distance (0.146 x element size) ahead of the fracture tip is the reason for the difference of approximately 10% between numerical and theoretical values. A larger search radius may be defined by the user, but practical problems could arise if propagating fractures intersect other discontinuities. For qualitative analyses the associated error may be ignored as absolute values are of minor importance.

The tensile strength of the rock mass can, in principle, be related to the critical tangential stress ahead of a flaw. Figure 2.4 can either be used to determine the stress concentration at varying distances ahead of a flaw of fixed length, or alternatively to determine the stress concentration at a fixed distance ahead of flaws of varying lengths. In the DIGS

application, the effective flaw length is controlled by the number of elements used to represent the flaw. In the previous example with a flaw length of 100 units, the stress concentration at 0.146 units ahead of the flaw is approximately 13. If the flaw length would have been 50 units for instance, a stress concentration of around 8 would be found at the same distance ahead of the flaw. The choice of an appropriate flaw length is therefore critical as it determines the stress concentrations at the fracture tip. This in turn can affect the results of associated numerical simulations; for instance in a situation where a propagating fracture tip in a non uniform stress field has to compete with fracture initiation from pre-existing flaws such as in the next example.

Fracturing in a uniaxial compressive environment from a single slot normally results in the formation of a fracture of limited extent as can be seen from Figures 2.5. Only in the case of extremely brittle materials, where the stress concentration at the fracture tip can be assumed to be infinite, and r in equation 2.1 vanishes, can unstable fractures be generated from a single pore in a uniaxial stress field. It is however of interest to note that zones of high tensile stress concentration can be observed after the primary fracture has grown to a certain length (Figure 2.5b).

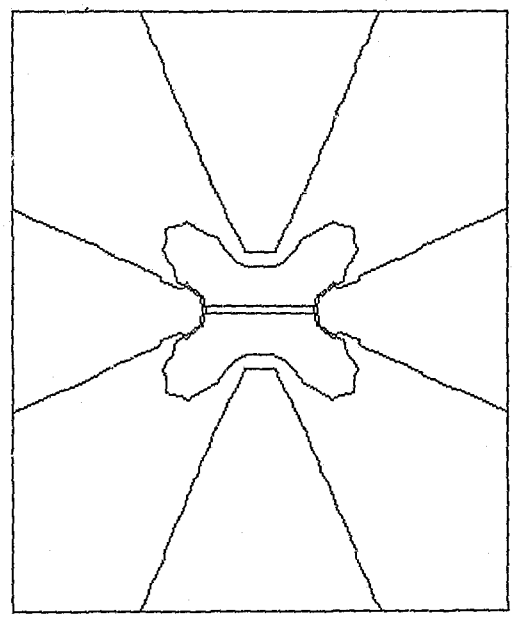

Figure 2.5a Distribution of minor principal stresses around an open flaw (horizontal slit) in a uni-axial stress field before fracture initiation. Loading is in a vertical direction and the contours indicate the transition between compression and tension of the minor principal stress (DIGS)

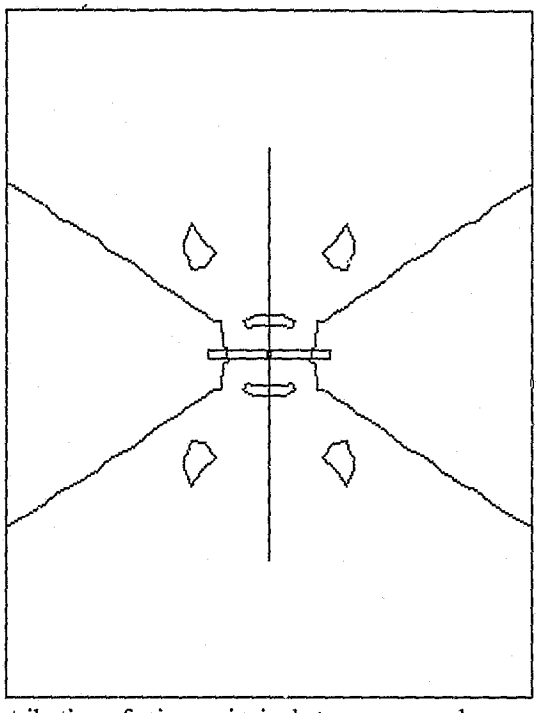

Figure 2.5b Distribution of minor principal stresses around an open flaw (horizontal slit) in a uni-axial stress field after some growth of the (vertical) primary fractures. Loading is in vertical direction and the contours indicate both the transition between compression and tension as well as maximum tensile values of the minor principal stress (DIGS)

In Figure 2.5b the tensile stress concentration near the fracture tips (collocation points) is less than the tensile stress concentration inside the closed zones which are shown in the figure. This is of course directly related to the choice of the search radius r in the numerical model, but, as has been mentioned before, only in extremely brittle materials would infinite stress concentrations at the fracture tips be approached. In the numerical model it is also assumed that the material is homogeneous except for the original flaw and the primary fractures. If (secondary) flaws are present in the zones of tensile stress concentration then the possibility arises for secondary fractures to initiate from these locations. These so-called remote or secondary fractures initiate from smaller size flaws around the major flaw at the locations of tensile stress concentration as is shown in Figure 2.6. The length of these flaws would determine the local stress concentrations and thus the initiation of fracturing. In terms of numerical representation, flaw length is equivalent to the number of segments which make up the flaw, as has been discussed previously.

The seed points for secondary fracturing in Figure 2.6 have been positioned at the centre of four of the six zones of local tensile stress concentrations according to Figure 2.5b. Primary fracturing in Figure 2.6 is similar to the primary fracturing in Figure 2.5b. The fact that secondary fracturing does not take place in symmetric fashion may be explained by the incremental nature of the numerical simulation which introduces immediate a-symmetry.

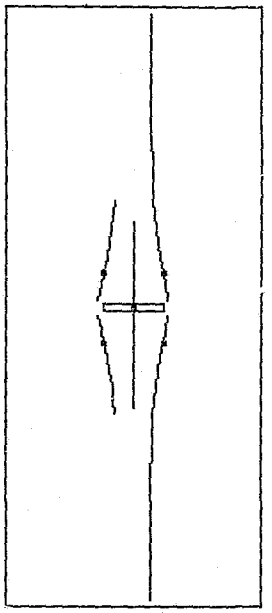

Figure 2.6 Primary and secondary fracture growth around a single open flaw in a uni-axial stress field (DIGS)

The fact that these secondary fractures can grow to larger lengths than the primary fractures in a uni-axial compressive environment deserves some attention here. The explanation for the extended propagation of secondary cracks around pores is associated with the stress distribution around these growth sites. The primary cracks are more restrained in their growth than the secondary fractures. The effects are clearly demonstrated in Figure 2.7 where it can be seen how much more efficiently the secondary fractures propagate.

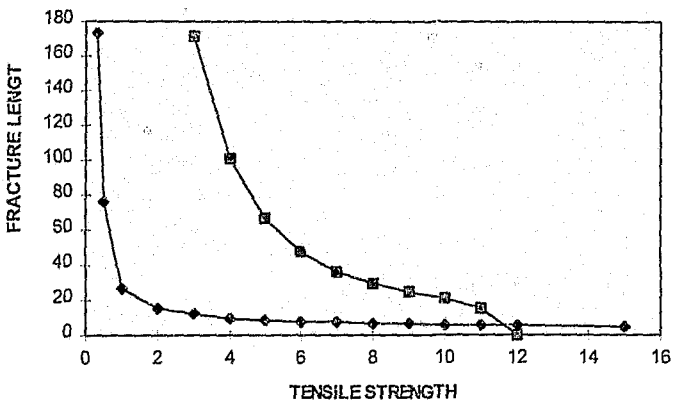

Figure 2.7 Fracture development from a single pore with a length of 4 (units): primary fracture (lower graph) and secondary fracture (upper graph)

Fracturing in response to mode II loading (shear stresses only) has been simulated as well, in order to complement the calibration of basic fracture processes. The critical theoretical length for a flaw can be approximated, using near crack tip stress conditions, as:

$$c = 2.3r\left(\frac{\sigma_{\theta\theta}}{\tau}\right)^2 + O\sqrt{r} \qquad (2.3)$$

where τ is the remote shear stress; the other parameters are depicted in Figure 2.3

In (2.3) it is implicitly assumed that the fracture angle with respect to the flaw is that one which results in the highest value for the tangential stress $\sigma_{\theta\theta}$. Using the same value as in the mode I fracturing example, namely $r = 0.146$, $\sigma_{\theta\theta} = 10$ units and $\tau = 1$ unit, it follows that the critical length l is equal to 67 units, while a critical value of 45 units is obtained from the numerical model. This demonstrates that similar deviations of the numerical results which have been observed under mode I loading conditions can occur under shear loading. The resulting (initial) fracture pattern and the associated stress field under pure mode II conditions in shown in Figures 2.8.

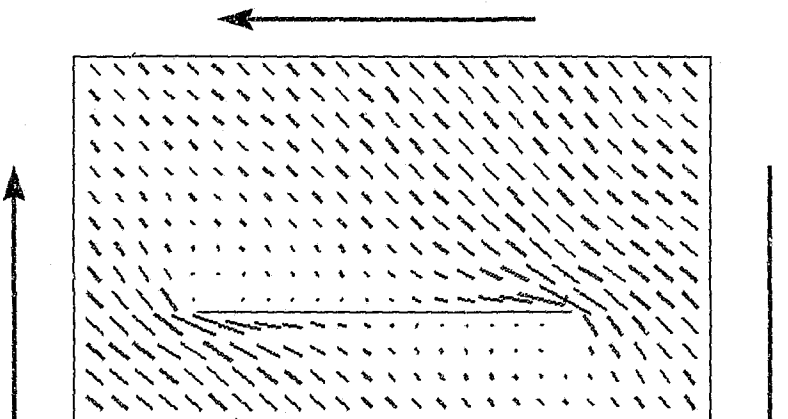

Figure 2.8 a Stress distribution around a flaw in a pure shear stress field before the initiation of fracturing. Only tensile stresses are represented here. (mode II loading conditions, DIGS)

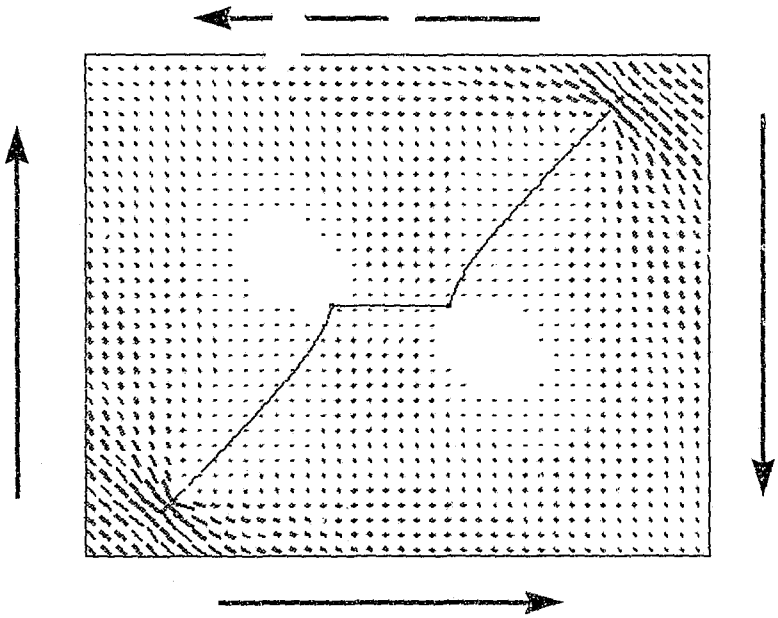

Figure 2.8b Stress distributions around a flaw in a shear stress field after the formation of the mode I fractures; only tensile stresses are represented here (mode II loading conditions, DIGS)

In most rock engineering applications, shear loading occurs in a compressive stress field. Compressive stresses may effectively result in the suppression of tensile fracturing, both under mode I and mode II loading conditions. The fracture mechanism itself is not affected by the presence of compressive stresses, but fracturing will become stable as driving forces are localised around individual flaws. The far field stresses may not be conducive to fracture initiation and propagation when compressive stresses are present. An increment in fracture length would therefore require additional driving forces at individual flaws and this will result in stable, sub-critical fracture growth. These fracturing processes do not result in failure of the rock, as long as individual flaws with their associated fractures are not interacting with neighbouring flaws and fractures. However, at a certain stage, when a critical density of flaws is activated and individual fractures have grown in a stable fashion to critical lengths, interaction processes are assumed to result in the formation of macro fractures by the linking of multitude of flaws and micro fractures. In the next section an attempt is made to simulate such interaction processes with the use of numerical models in which many brittle micro fractures can be accommodated.

2.3 MICRO FRACTURING AND POTENTIAL FRACTURE COALESCENCE MECHANISMS UNDER COMPRESSIVE STRESSES

Simulation of brittle fracturing in a compressive stress environment requires a model of the micro structure of a particular material in order to capture the stable micro fracturing processes which ultimately lead to the formation of the unstable (brittle) macro fracture. There may be a large variation of micro structures which could be responsible for the initiation of micro fractures. Only some of those, such as pores, point loading and local stiffness variations, do not require any plastic deformations in order to induce fracturing and can thus be considered true brittle fracture mechanisms. However the sliding crack, which is certainly a good representative model for most micro mechanical fracture sources such as grain boundaries, frictional cracks, cleavages, slip bands, plastic inclusions, etc., does implicitly rely on plastic deformations as a source for micro fracture generation and propagation. Many researchers have used the sliding crack model in an indirect way by treating the sliding crack model as a linear elastic model. (Fairhurst and Cook, 1966; Horii and Nemat-Nasser, 1986; Kemeny and Cook, 1987; Zheng et. al., 1989) As a consequence, the problem of micro fracture interaction and coalescence has been treated as an elastic and purely brittle phenomenon. As it is observed that extremely brittle materials do not show coalescence of micro fractures into large scale shear fractures, the assumption of an elastic model is questionable.

2.3.1 SLIDING CRACK MODEL

An attempt is made to represent the sliding crack and the associated wing crack formation, as proposed by Brace and Bombolakis (1963) directly. A single sliding crack and associated wing cracks have first been analysed with DIGS in a simulation in which wing crack growth followed a series of load increments. While increased uni-axial pressure resulted in stable propagation of wing cracks, the deformations assumed a non linear relation with respect to the applied pressure. This non linear behaviour is a result of increased sliding deformation, associated with the growth of wing cracks and is shown in Figure 2.9. Without the development of wing cracks the sliding along the crack is limited and the deformation is linear with respect to the load. Unloading involves hysteresis as frictional resistance has to be overcome to reverse the slip deformation. With the formation of wing cracks, additional sliding and associated deformations are induced and a non-linear relation between slip and applied stress can be observed in Figure 2.9.

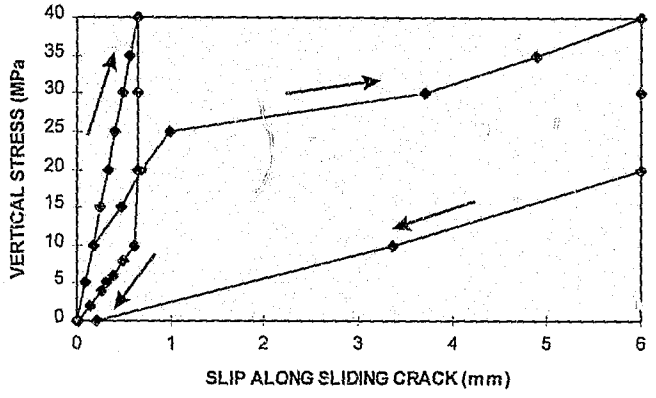

Figure 2.9 Stress-strain behaviour of sliding cracks with (smaller loop) and without (larger loop) wing crack formation (uni-axial loading, DIGS modelling results)

Such non linear behaviour has also been demonstrated by Meyer et al. (1992), who used a theoretical model proposed by Kemeny and Cook (1987) in which the interaction of micro fracturing is considered. In this model the crack tip stress intensity factor for two approaching wing cracks is expressed as:

$$K_1 = \frac{2l_0\tau\cos\theta}{\sqrt{b\sin\left(\pi l/b\right)}} - \sigma_2\sqrt{2b\tan\left(\pi l/2b\right)} \tag{2.4}$$

where $\tau = \frac{1}{2}\left(\sigma_1 - \sigma_2\right)\sin 2\theta - \tau_f$, (2.5)

$$\tau_f = \frac{1}{2}\mu\left(\sigma_1 + \sigma_2 + \left(\sigma_1 - \sigma_2\right)\cos 2\theta\right), \tag{2.6}$$

θ is the inclination of the sliding crack,
μ is the coefficient of friction along the sliding crack,
$2b$ is the (vertical) distance between two sliding cracks,
$2l$ is the (vertical) length of a sliding crack with its wing cracks
and l_0 is the length of the sliding crack itself

Figure 2.10 shows the sliding crack model and is used to explain the potential for brittle behaviour due to the collinear interaction of a series of tensile cracks which are driven from sliding cracks. The model can in principle be used to predict non linear behaviour including strain hardening, strain softening and dilatation by using the Irwin relationship for the additional elastic strain energy due to the crack:

$$G = \frac{K_1^2\left(1-\upsilon^2\right)}{E} \tag{2.7}$$

equation 2.7 does not take into account parallel or en echelon crack interaction as it is assumed by the authors that crack interaction mainly occurs in the form of collinear coalescence into vertical splitting cracks under conditions of low confinement.

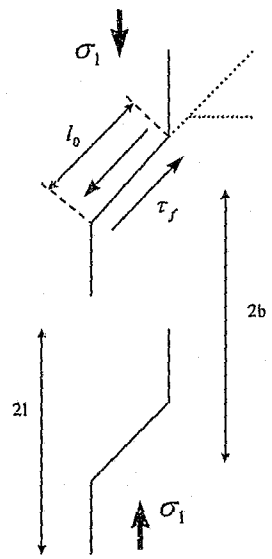

Figure 2.10 Sliding crack model (after Meyer et al., 1992)

By equating the work done by the applied loads against the displacements induced by the combined sliding crack/tensile crack combination and the strain energy due to the crack, it is possible to derive a closed form analytical solution for the stress-strain relation which is effectively based on the stress intensity factor as expressed in (2.4). This stress-strain relation is non linear and predicts strain-softening for relative crack length values (l / b) which exceed a value of approximately 0.7 (a value of 1.0 would result in an infinite stress concentration at the fracture tips).

Numerical analyses of the crack model shown in Figure 2.10 demonstrated, however, that collinear interaction of wing cracks as assumed by Kemeny and Cook (1987) is not exactly possible. In order for the cracks to coalesce, as assumed in the Kenemy and Cook model, the initial sliding cracks have to be located as shown in Figure 2.11. This location is such that the sliding cracks cannot be placed directly beneath or above one other as this would not allow the coalescence of the wing cracks with each other or with the neighbouring sliding crack. In order to enable the fractures to join, the initial sliding cracks have to be positioned along a line which is inclined with respect to the direction of the major principal stress (vertical). However, the large scale fracture, which results from the coalescence process, is therefore not a pure vertical splitting fracture, but should rather be interpreted as a shear fracture. The inclination of this shear fracture depends on the relative location of the initial sliding cracks from which the coalescing wing cracks are to be generated. Figure 2.11 suggests that this inclination is steep in relation to a traditional shear band orientation if the distance between the sliding cracks with respect to their length is large.

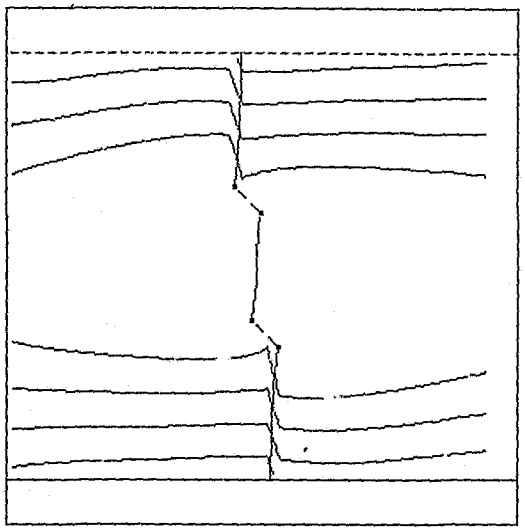

Figure 2.11 Coalescence of two sliding cracks into an effective "shear" fracture; contour lines indicate levels of vertical deformation

A potential model for a true splitting fracture is shown in Figure 2.12. Pairs of sliding cracks, which are mirror images, are introduced here in order to allow a perfect alignment of the resulting large scale fracture with the major principal stress. At first sight this model also appears to offer the potential for unstable behaviour, as the application of equations 2.4 would suggest. However, a comparison of Figures 2.11 and 2.12, in which the results of numerical models of the shear fracture and the splitting fracture are shown respectively, indicates that while in the shear fracture scenario of Figure 2.11 unstable slip can take place in response to an imbalance in the boundary forces, the splitting crack system scenario of Figure 2.12 is not subjected to unbalanced boundary forces and therefore does not show unstable shear deformations. The coalescence of the sliding cracks would not lead to global failure and associated softening in this case. The imbalance in boundary forces in the case of Figure 2.11 can be explained from the inclination of the resulting (shear) fracture with respect to the vertical direction of the principal stresses. Slip along this shear fracture will be induced when uniform stresses are applied to the vertical boundaries.

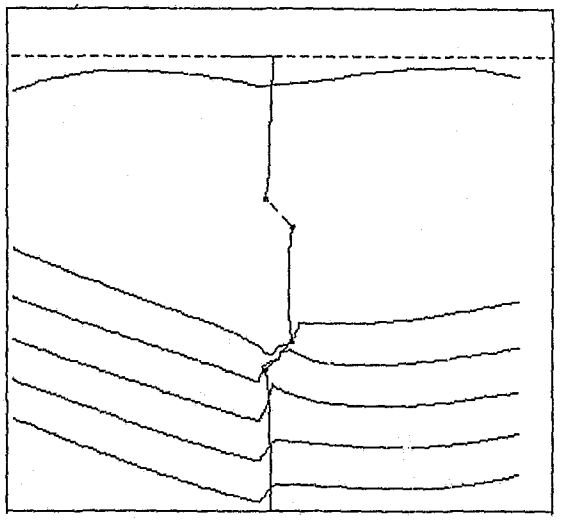

Figure 2.12 Coalescence of two sliding cracks into a "splitting" fracture; contour lines indicate levels of vertical deformation

In the Kemeny/Cook (1987) model it is assumed that a system of coalescing sliding cracks and wing-cracks can be treated as an isolated column. The interaction with neighbouring columns is not taken into account in their model. Such a situation is not realistic, as a single column, containing a system of sliding and wing cracks, should not lead to the instability of the medium in which it is located. A system, consisting of multiple columns, might allow for instability under similar loading conditions, but such a system is not represented by the model of Kenemy and Cook.

Instability induced by inclined large scale shear fractures as shown in Figure 2.11 is related to an unbalance in the external forces which provides a more plausible mechanism for large scale instability than vertical splitting fractures under loading conditions which do *not* involve direct tensile stresses. However, typical observations of processes leading to shear failure, indicate a different mechanism of micro fracture coalescence. Hallbauer et al. (1973) for instance demonstrated that in tri-axial loading experiments on quartzite specimens, after an initial random distribution of micro cracks, the density of micro fractures becomes localised with further loading. This phenomenon is most likely to be associated with the effect of micro cracks on the local strength of the rock. Coalescence of micro cracks takes place at a later stage, probably when a critical density of micro cracks has been reached and a shear band is formed in a similar fashion to the formation of shear banding in granular materials.

The sliding crack model is a two dimensional representation of brittle, tensile fracturing induced by some form of shear deformation. As such it can demonstrate the combined effect of brittle and plastic behaviour, but the three dimensional interaction of micro fractures which lead to the formation of a shear band as described by Hallbauer et al. (1973) is not represented by a two dimensional sliding crack model which assumes the merger of wing crack tips. Splitting fractures are also not necessarily associated with coalescence processes, but may be true macro fractures in the sense that their formation is

controlled by the propagation of a single fracture front (tip) which is driven by tensile stresses. Jaeger (1960) also concluded from his observations on tri-axially and uni-axially loaded specimens that splitting fractures were associated with tensile stresses induced by (unwanted) boundary conditions associated with the transmission of forces from the loading apparatus into the specimen. Jaeger (1960) claims that under loading conditions in which no tensile stresses are applied, failure is ultimately caused by large scale shear fractures. This is in contradiction with the findings of Fairhurst and Cook (1966), who claim that: ".....macroscopic fracture frequently occurs through the buckling of incipient slabs generated by cleavage". However, their claim is mainly based on the finding that surface parallel fracturing are often observed around underground openings in combination with the assumption that only compressive stresses are acting in such an environment. The argument of surface parallel fracturing is often used to motivate the presence of extension fractures in a medium which is subjected to compressive stresses. Closer examination of these parallel fractures often reveals connecting fractures between the extension fractures. It is not clear if these connecting fractures are formed before or after the formation of the extension fractures, but the presence of these connecting fractures warrants further investigation.

In another model proposed by Kemeny and Cook (1987), shear faulting is represented by a parallel set of cracks which are inclined at an angle with respect to the major principal stress. It is assumed that these cracks propagate in the plane of the initial crack to coalesce with neighbouring cracks and so form a continuous large scale shear fracture. This model predicts initial softening upon fracture growth and unstable behaviour upon fracture coalescence in a similar fashion to their splitting fracture model. Coalescence is associated with an increase in the stress intensity around the fracture tips which approaches infinity upon final coalescence, in the same way as in their splitting fracture model. As has been discussed before, the sliding and wing crack model can also be used directly to construct a large scale shear fracture and a separate shear faulting model is thus not required. It is, however, highly questionable whether fracture coalescence is represented appropriately by a model which assumes that individual fracture tips connect and in such a way allows fractures to merge. Although it is possible to simulate such a mechanism in a two dimensional numerical model by adjusting the positions of the flaws in a very delicate way, it is highly unlikely that similar processes would take place in a natural way as no evidence of such a phenomenon has been reported.

2.3.2 PRESSURISED CRACK MODEL

Zheng et. al. (1989) use a numerical model to simulate micro fracture coalescence by adapting Fairhurst and Cook's (1966) representation of the sliding crack as a pressurised crack. In this representation only the opening of the wing cracks due to the slip along the sliding crack is considered; the sliding itself is not taken into account. Splitting of grains was modelled in Zheng's model by assuming pressurised crack of fixed length, which simulate the loss of tensile stress in a particular grain. Grain centres were randomly distributed throughout the model and acted as potential seeds for further micro fracturing. The seed experiencing the highest (induced) tensile stress, due to the action of neighbouring pressurised seeds, is forced to fail next and is thus also pressurised. This process repeats itself in an incremental fashion until insufficient tensile stresses are

generated for further fracture initiation and associated pressurisation. A typical result is shown in Figure 2.13 which shows Zheng et. al.'s simulation of micro fracture formation.

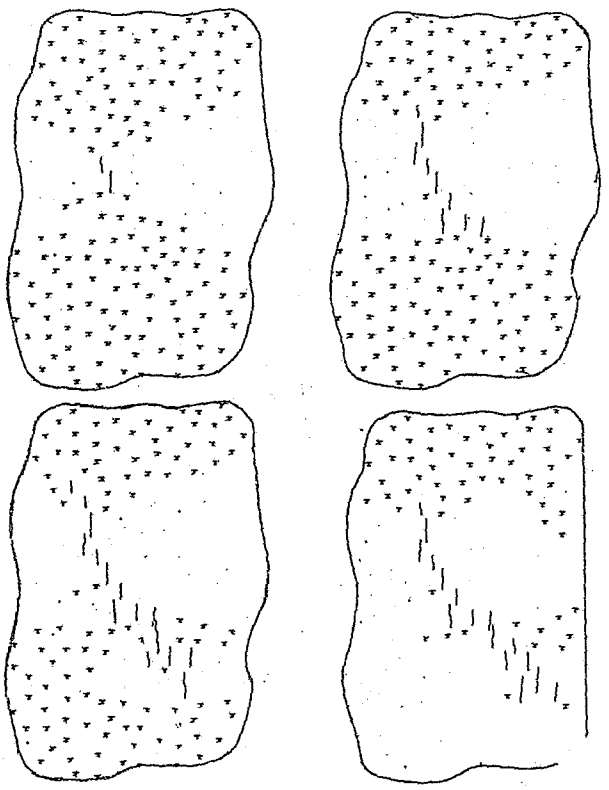

Figure 2.13 Numerical simulation of micro fracture formation and interaction (after Zheng et. al., 1989)

Zheng et. al. relate their results to an embryonic shear band, which implies that the formation of a shear band can result from an elastic process. In order to investigate this possibility, a similar model to the one reported by Zheng et. al. (1989) has been set up using DIGS. A random distribution of potential fracture nucleation points was excited by one initial pressurised crack until, after an incremental process in which newly formed cracks were also pressurised, no additional fractures initiated from any of these seeds. Each increment involves the selection of the nucleation point with the highest stress level after which a fracture is allowed to initiate from the selected nucleation point. This fracture is subsequently pressurised to the same level as the initial crack after which the next nucleation point is determined, etc. A typical result is shown in Figure 2.14 where it can be observed that instead of a 'shear band' with a shallow inclination, the coalescence process results in the formation of a band of micro fractures which is much steeper and more or less oriented along the direction of the major principal stress (vertical). The initial flaw is located in the middle of the specimen and subsequent flaws were triggered successively in a stepwise process.

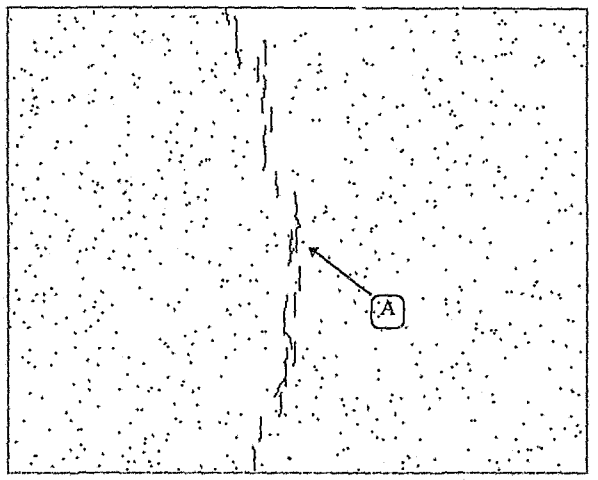

Figure 2.14 Band of interacting micro fractures initiated from an initial flaw A, in a random flaw distribution in a bi-axial stress field, with loading in a vertical direction and horizontal confinement; minimum crack pressurisation (DIGS)

The fracture pattern in Figure 2.15 is derived from exactly the same flaw distribution as the fracture pattern in Figure 2.14, but the cracks have been pressurised to much higher levels. While the resulting fracture patterns appear to resemble shear fractures, it should be realised that the applied crack pressures are probably unrealistically high, something which is also reflected in the orientation of individual (micro) fractures in Figure 2.15. Many of these fractures assume an inclined orientation with respect to the global field stresses due to the local effect on stress distribution by the pressurised cracks. As this is not confirmed by observed behaviour, the results from Figure 2.15 should be regarded as less realistic than those from Figure 2.14, where the applied pressure inside the micro cracks was just sufficient to enable the fracturing process and the orientation of the micro fractures was aligned with the direction of the field stresses.

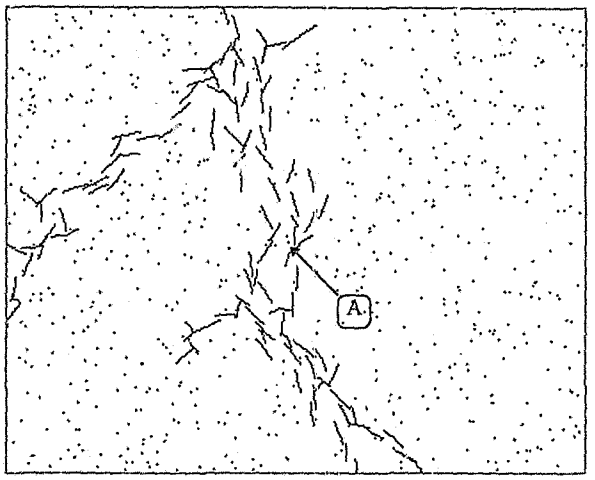

Figure 2.15 Band of interacting micro fractures initiated from an initial flaw A, in a random flaw distribution in a bi-axial stress field, very high crack pressurisation (DIGS)

While the results of Figure 2.14 appear to be the most realistic, they do not confirm the results from Zheng et. al.'s model (Figure 2.13). In order to analyse this discrepancy it was decided to investigate the stress distribution around a single pressurised crack in more detail. Figure 2.16 shows the induced tensile stresses around a single flaw which is subjected to internal compression.

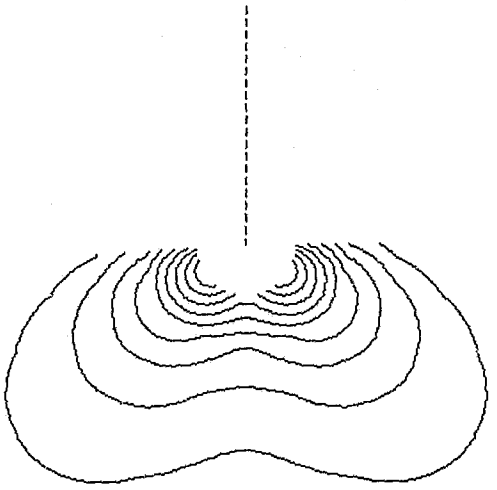

Figure 2.16 Distribution of minimum principal stresses around the tip of a pressurised crack (dotted line) in a vertical uni-axial stress field. (DIGS)

It can be seen from Figure 2.16 that the maximum tensile stresses are not found directly ahead of the flaw. They appear to be located along a line which is inclined with respect to the direction of the major principal stress and the orientation of the flaw itself. This implies that, if nucleation points were located at a fixed distance from the flaw tips, fracturing would not be initiated from the two nucleation points which are located directly ahead of the two flaw tips. The most favourable nucleation points are in fact located along two lines from each flaw tip as can be appreciated from Figure 2.16. When the first flaw is activated, four potential nucleation points, at an equal distance from the fracture tips, can be found. However, after one of them has been selected for initiation of the second fracture, a certain preferential nucleation point will prevail for the initiation of the third fracture. The reason for this prevalence is the combined effect of the first and the second fracture on the stress distribution around the activated flaws. When a regular distribution of nucleation points is used, this effect becomes dominant as can be observed from Figure 2.17. Similar observations have been made by Du and Aydin (1991) who demonstrated with an analytical model that the interaction between mode I micro cracks is the strongest when these micro cracks are located in a conjugate echelon array.

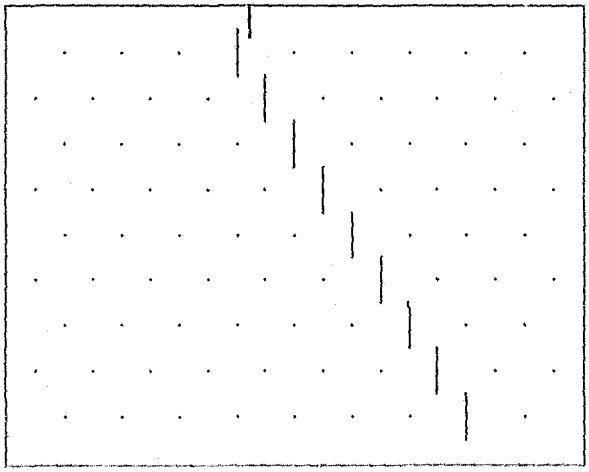

Figure 2.17 Band of interacting micro fractures initiated from a regular flaw distribution. The first fracture is the top one (DIGS)

The mechanism is however extremely sensitive to irregularities in the distribution of nucleation points. By varying the distance between the nucleation point and the flaw it was found that critical deviations occurred at around 2% of the distance between flaw and nucleation point. The critical distance was that one at which the normally selected nucleation point would *not* be the source of fracture initiation, but another nucleation point would be selected instead. From these results it is clear that the distribution of nucleation points plays a more dominant role than the coalescence effect of the brittle flaws. Results obtained from these models therefore reflect the distribution of seed points rather than any fundamental process of micro fracture coalescence.

2.3.3 OPEN FLAW MODEL

If an alternative micro mechanical model in the form of open flaws instead of pressurised cracks is chosen, different effects on the stress distribution can be expected. These effects are not unlike those which are described in Chapter 5, where the fracturing around large scale openings in compressed rock is analysed. Figure 2.18 shows the resultant stress distribution around a horizontal slot in a uni-axial stress field and Figure 2.19 shows a similar situation after a crack has been allowed to grow from the centre of the horizontal slot at right angles to the slot. This situation is supposed to represent the micro fracturing around openings subjected to compression, and is in fact similar to the results shown in Figures 2.5. Figure 2.18 and Figure 2.19 are however more detailed and demonstrate more clearly that the distribution of minor principal (tensile) stresses is such that fracture initiation from secondary flaws can be expected to occur at locations which are not necessarily located directly underneath or above the primary flaw.

A potential mechanism for coalescence of neighbouring flaws could be expected from the generation of multiple fractures in the region of tensile stresses between neighbouring flaws. Secondary processes, associated with the presence of closely spaced multiple fractures, could be expected to result in failure. As can be appreciated from Figure 2.18 and 2.19, the tensile regions tend to expand in directions which deviate from the vertical direction and thus the direction of the applied loading. As failure is expected to occur in these areas, it is possible that neighbouring flaws could be linked by such failure zones. Such a process may ultimately lead to general failure and instability.

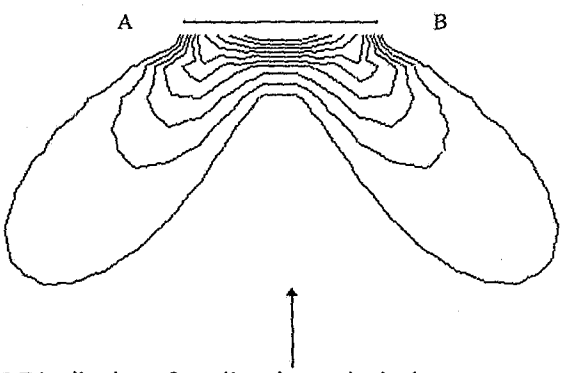

Figure 2.18 Distribution of tensile minor principal stresses around an open flaw in the form of slot A-B. Uni-axial compressive stress field (DIGS, half symmetry)

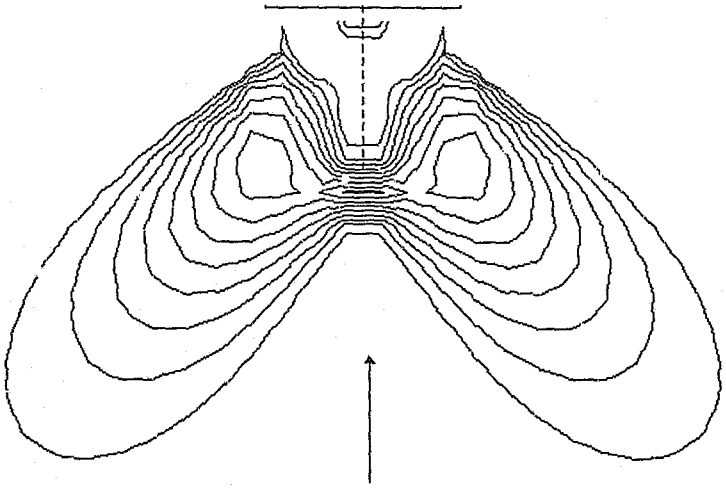

Figure 2.19 Distribution of minor tensile principal stresses around a horizontal slot in a uni-axial compressive stress field after the formation of a vertical fracture which is represented by the dotted line (DIGS, half symmetry)

2.4 CONCLUSIONS

While the application of the particular sliding crack model described in section 2.3 has not resulted in the simulation of a large scale shear fracture, this does not imply that the basic sliding crack model is inappropriate for that purpose In Chapter 5, for instance, another attempt is made to apply the sliding crack model by using it in numerical models which are less prescriptive in terms of coalescence rules than the model described here.

The simulation of micro fracturing from pressurised cracks demonstrated that the resulting fracture geometry is sensitive with respect to the distribution of nucleation points. The coalescence of micro fractures into a shear band could only be obtained by using a very uniform distribution of such nucleation points. A small deviation in this distribution led to the formation of a band of activated micro fractures which was aligned with the direction of the major principal stress.

Secondary fracturing around pores or soft inclusions may be an alternative mechanism which could explain the development of failure through the coalescence of these flaws. It has been shown that relatively large areas around such flaws can be subjected to tensile stresses and initiation of fractures can therefore be expected from such areas. Ultimate collapse of these fractured areas is proposed as a potential failure mechanism.

As an alternative to fracture mechanics principles for describing failure, the theory of plasticity can be applied. Although brittle behaviour is in principle not catered for by the original theory, which was developed for ductile deformation processes, recent extensions allow the theory to deal with a wide range of inelastic behaviour. Various failure criteria can be accommodated, especially those criteria which assume some form of shear failure. In the next chapter the applicability of plasticity to the (brittle) failure of rock, subjected to compressive stresses, is investigated. Although the theory of plasticity does not allow a

direct representation of the physical failure processes in rock, it may be possible to use empirical rules in order to obtain an indirect representation of large scale failure processes. The subject of shear fracture formation will be the main objective in this investigation, as this is perceived to be the basis of instability and rock failure in compressive stress environments.

3.0 APPLICABILITY OF PLASTICITY TO FAILURE OF ROCK

3.1 INTRODUCTION

The theory of plasticity originated from attempts to describe the failure processes in metals after their elastic limit has been exceeded. Plasticity theory is, in fact, based on the behaviour of metals and was only later modified and applied to other materials. Plastic deformations in single crystal metals occur by slip along planes which have the closest packing of atoms. The location of such planes is determined by the particular crystal structure. The direction of slip along these slip planes is also, and without exception, along the line of closest packing of atoms, with the combination of slip plane and slip direction being termed the *slip system.* Slip normally takes place on multiple slip planes when the shear stress acting along such planes exceeds a critical value.

Dislocation theory is used to describe plastic deformations in metals. According to dislocation theory, dislocations are localised at the boundaries of slip planes and are associated with local elastic straining. Von Mises (1928) first pointed out that five independent slip systems are necessary for a randomly oriented polycrystal to undergo a general homogeneous deformation. Even when five independent systems are available, brittleness may be encountered in polycrystals due to local strain incompatibility at barriers to plastic flow. Grain boundaries, solid solutions and phase precipitation provide barriers to slip planes and effectively increase the strength of metals while reducing the ductility. Work hardening in metals is related to dislocation density and the work hardening rate depends on the rate at which dislocations increase with strain (Pickering, 1978)

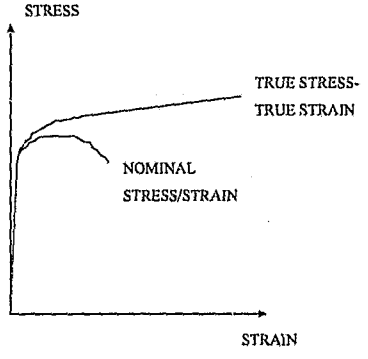

Figure 3.1 Typical stress-strain relation observed in tensile testing of metals.
(the true stress/strain has been obtained by considering the effective reduction in area of the tested specimen, whereas the nominal stress/strain is based on the original cross section of the specimen before the test)

Results of a standard tensile test are shown in Figure 3.1 and it is clear from these results that hardening continues until brittle failure is initiated. Perfect plasticity (no work hardening) is therefore only a theoretical possibility as barriers to plastic flow will always

be present in real materials. For purposes of simplicity the ductile behaviour of metals is often idealised by a perfectly plastic model in which the yield stress remains constant during plastic deformation. As a yield criterion the Von Mises criterion is most commonly used:

$$(\sigma_2 - \sigma_3)^2 + (\sigma_3 - \sigma_1)^2 + (\sigma_1 - \sigma_2)^2 = 2\sigma_0^2 \tag{3.1}$$

where σ_0 is a constant yield strength and σ_i are the principal stress components.

Of interest is the fact that only the stress deviation, or shear stress, controls the yield strength according to this criterion. The level of the hydrostatic pressure does not affect the criterion. While this is satisfactory for most metals, it does not hold for other materials such as soils, concrete and rock.

3.2 MOHR-COULOMB AND SHEAR BAND LOCALISATION

Mohr (1900) proposed that when the shear and normal stresses which act across a particular plane reach critical values, shear failure along that plane is initiated. These critical values are expressed by a relation between the shear stress and the normal stress, which is characteristic of a particular material

$$|\tau| = f(\sigma) \tag{3.2}$$

This relation is not necessarily defined by an analytical expression, but is obtained from experimental data, as the envelope of the Mohr circles, which correspond to failure under a variety of loading conditions (Figure 3.2). This so-called Mohr envelope can be represented in shear and normal stress space and allows the determination of the notional plane along which shear failure is assumed to have taken place to be determined. The critical assumption in Mohr's hypothesis is the existence of a (single) shear failure plane controlling the strength of a particular material.

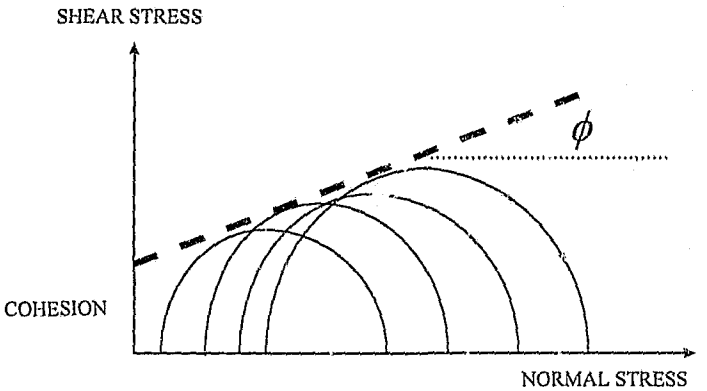

Figure 3.2 Mohr envelope based on the results of various tri-axial tests

While it is true that dominating shear failure surfaces are observed in typical specimens after failure has occurred, such surfaces are often of a complicated geometry and are the result of intricate micro mechanical processes preceding the formation of the final shear band. Stress distributions may already be affected before the activation of the shear band and the assumption of a planar surface in a uniform stress field, which represents the failure processes and associated strength of a particular material, is a simplification which may not always be justified. In that case the Mohr envelopes can only be used as a failure surface without defining the causes of failure. One of the simplest representations of the Mohr envelope is the Coulomb (1776) criterion which assumes a linear relation between the shear and normal stresses acting on a shear failure plane:

$$|\tau| = C_0 + \mu\sigma \tag{3.3}$$

whereby C_0 is the cohesion and μ is termed the coefficient of internal friction of the material.

Although this criterion is very attractive and popular, it is based on the same assumptions as the Mohr criterion, while an additional assumption is that cohesion and friction are simultaneously active. This is not necessarily true and in fact recent publications (Martin, 1993) suggest that frictional resistance in brittle rocks only becomes activated after the cohesion is destroyed (Figure 3.3). The application of the Coulomb criterion should for this reason always be critically judged, especially if brittle materials are involved.

Martin (1993) refers to the stress level at which permanent strains are introduced in the rock as 'crack damage stress'. This parameter is indicated as σ_{cd} in Figure 3.3. Typical peak values of the crack damage stress are approximately 70% of the short term peak strength as recorded in standard laboratory tests. Very slow loading processes can reduce the peak strength of the rock to the crack damage stress and even affect the mechanism of failure. Martin (1993) also observed that axial splitting of the specimens did not occur if the loading was applied extremely slowly. Instead characteristic shear planes, formed by processes of internal sliding, developed. Fast loading apparently did not allow sufficient time for the accumulation of damage necessary to complete the process of shear fracture formation in his specimens.

In figure 3.3 a damage parameter ω is used. This parameter is defined as the cumulative permanent volumetric strain and is thus a reflection of inelastic strain.

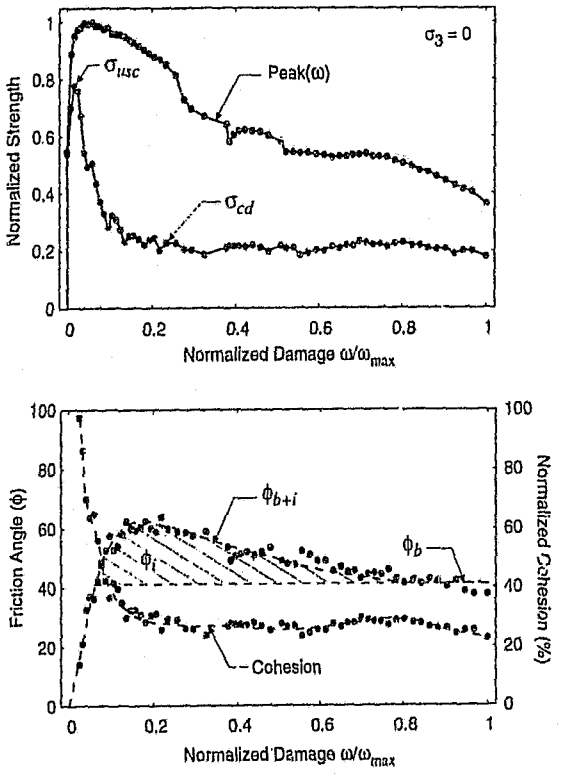

Figure 3.3 Cohesion softening and friction hardening as a function of damage (after Martin, 1993)

Granular materials differ in many respects from (ideal) metals, but one of the most relevant differences is the change in volume which is associated with shear distortion. In metals, such a volume change is not observed during plastic deformations, while frictional resistance is also absent. Plastic deformation in granular materials mainly takes place along the boundaries of grains which does involve frictional resistance and, depending on the density of packing before failure, the assembly of grains can either increase or decrease in density. The volume change which is associated with this change in density is referred to as dilatancy and the parameter used to characterise this change in volume is the dilatancy angle ψ. This angle represents the ratio between the plastic volume change and the plastic shear strain change and is defined by the flow rule and an applicable plastic potential function, $g(\sigma)$.

A material element is considered to be in a plastic state when the so-called yield strength, which is defined by a yield function, $f(\sigma)$, is reached. The most commonly used yield function is the Mohr-Coulomb criterion which defines a critical linear relation between the shear component and normal component of the stresses acting on any (planar) surface as expressed in equation (3.3). Figure 3.4 shows the Coulomb yield function and the Mohr stress circle for a plane state of strain.

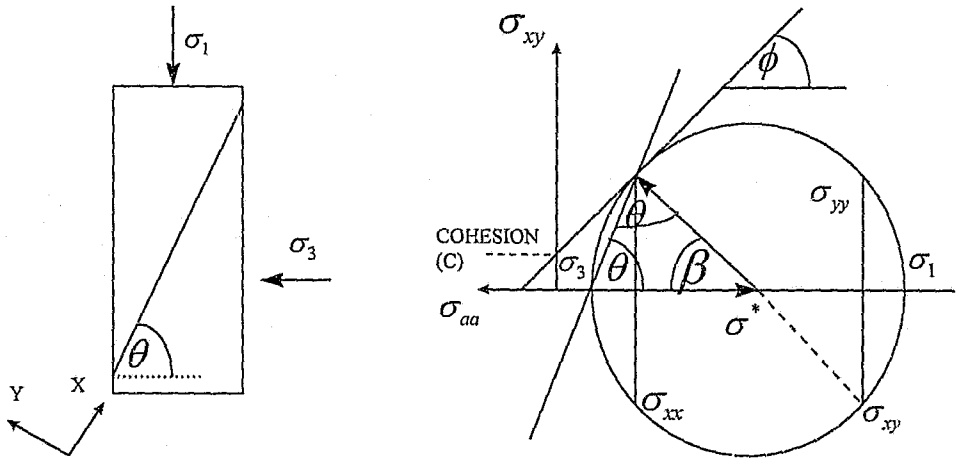

Figure 3.4 Mohr stress circle and Coulomb yield surface

The Mohr stress circles are bound by the Coulomb yield function which can be expressed by an expression which is equivalent to (3.3):

$$\tau^* - \sigma^* \sin\phi - C\cos\phi \le 0 \tag{3.4}$$

where σ^* is the centre of the stress circle,

$$\sigma^* = -\frac{\sigma_{xx} + \sigma_{yy}}{2} \tag{3.5}$$

τ^* is the radius of the stress circle,

$$\tau^* = \sqrt{\frac{(\sigma_{xx} - \sigma_{yy})^2}{4} + \sigma_{xy}^2} \tag{3.6}$$

and ϕ is related to the friction coefficient μ by:

$$\phi = \arctan\mu \tag{3.7}$$

The yield function $f(\sigma)$ is in this case defined as:

$$f(\sigma) = \tau^* - \sigma^* \sin\phi - C\cos\phi \tag{3.8}$$

The flow rule is expressed in terms of the derivatives of the plastic potential function $g(\sigma)$:

$$d\varepsilon^p = d\lambda \frac{\partial g}{\partial \sigma} \tag{3.9}$$

where the superscript p denotes plastic quantities. λ is a non-negative multiplier if plastic loading occurs ($f(\sigma) = 0$ and $df(\sigma) = 0$), otherwise it becomes zero.

The function $g(\sigma)$ is called the plastic potential function and a suitable expression for $g(\sigma)$ is:

$$g(\sigma) = \tau^* - \sigma^* \sin\psi + C \tag{3.10}$$

where ψ is the dilatancy angle as shown in Figure 3.5.

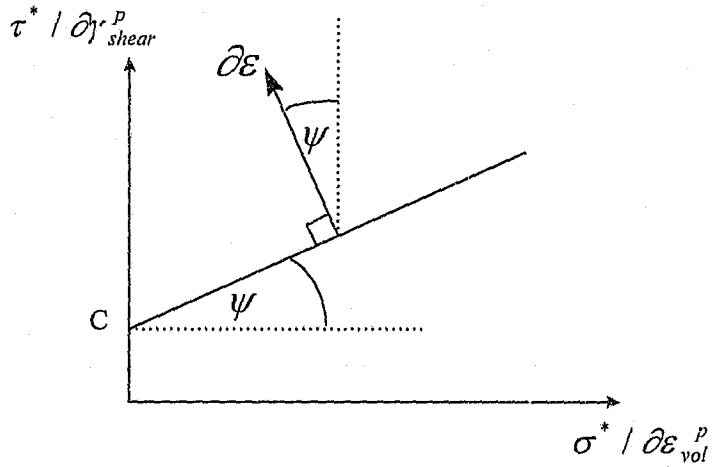

Figure 3.5 Plastic deformations and parameters associated with the plastic potential function

The plastic potential function $g(\sigma)$ in (3.10) has been chosen in such a way that it closely resembles the Mohr-Coulomb yield function $f(\sigma)$. The main difference is the substitution of the angle of internal friction ϕ by a dilatancy angle ψ. In that case a so called co-axial model is operative. In such a model strain rate and stress vectors are aligned, and can be displayed in the same system of axes (Figure 3.5). As the yield function and the plastic potential function are represented in a similar system, the relationship between plastic strains and stresses is relatively simple. The assumption of co-axiality in material behaviour is however a simplification of true material behaviour and may not always be justified.

Differentiating $g(\sigma)$ with respect to the stresses, the flow rule in equation (3.9) can be expressed for plane strain conditions as:

$$\begin{bmatrix} d\varepsilon_{xx}^{p} \\ d\varepsilon_{yy}^{p} \\ d\gamma_{xy}^{p} \\ d\varepsilon_{zz}^{p} \end{bmatrix} = \frac{d\lambda}{2} \begin{bmatrix} (\sigma_{xx} - \sigma_{yy}) / 2\tau^{*} + \sin\psi \\ -(\sigma_{xx} - \sigma_{yy}) / 2\tau^{*} + \sin\psi \\ 2\sigma_{xy} / \tau^{*} \\ 0 \end{bmatrix} \tag{3.11}$$

As the volumetric plastic strain rate is defined as

$$d\varepsilon_{v}^{p} = d\varepsilon_{xx}^{p} + d\varepsilon_{yy}^{p} + d\varepsilon_{zz}^{p} \tag{3.12}$$

and the rate of plastic distortion is defined in a similar way as the shear stress τ^{*} from equation (3.6), bearing in mind that $\gamma_{xy} = 2\varepsilon_{xy}$:

$$d\gamma^{p} = \sqrt{(d\varepsilon_{xx}^{p} - d\varepsilon_{yy}^{p})^{2} - (d\gamma_{xy}^{p})^{2}} \tag{3.13}$$

It can be found that by manipulating equations (3.11), (3.12) and (3.13)

$$d\varepsilon_{v}^{p} = \lambda \sin\psi, \tag{3.14}$$

$$d\gamma^{p} = \lambda \text{ and} \tag{3.15}$$

$$\sin\psi = \frac{d\varepsilon_{v}^{p}}{d\gamma^{p}} \tag{3.16}$$

The volumetric plastic strain rate and the rate of plastic distortion can also be expressed in terms of principal strain rates as:

$$d\varepsilon_{v}^{p} = d\varepsilon_{1}^{p} + d\varepsilon_{2}^{p} + d\varepsilon_{3}^{p} \text{ and} \tag{3.17}$$

$$d\gamma^{p} = \left| d\varepsilon_{1}^{p} - d\varepsilon_{3}^{p} \right| \tag{3.18}$$

As $d\varepsilon_{2}^{p} = 0$ (plane strain), it follows that

$$d\gamma^{p} = \left| 2d\varepsilon_{1}^{p} - d\varepsilon_{v}^{p} \right| \text{ and thus} \tag{3.19}$$

$$\sin\psi = \frac{d\varepsilon_{v}^{p}}{2d\varepsilon_{1}^{p} - d\varepsilon_{v}^{p}} \tag{3.20}$$

this expression is also valid under tri-axial compressive loading conditions if the plastic potential function can be described by the Mohr-Coulomb criterion.

Physically, ψ is associated with the dilation which occurs normal to a plane during sliding along that plane (Figure 3.6). Once sliding is initiated under constant normal stress, the

stresses parallel to the shear plane will be constant, so that both the elastic and plastic strain rates become zero ($d\varepsilon_{xx} = d\varepsilon^{e}_{xx} = d\varepsilon^{p}_{xx} = 0$) and equation (3.20) can be rewritten:

$$\sin\psi = \frac{d\varepsilon^{p}_{yy}}{\sqrt{(-d\varepsilon^{p}_{yy})^2 + (d\gamma^{p}_{xy})^2}} \tag{3.21}$$

and simplified again by

$$\tan\psi = \frac{d\varepsilon^{p}_{yy}}{d\gamma^{p}_{xy}} \tag{3.22}$$

which compares directly to Figure 3.6 in which the normal and shear deformations are related in exactly the same way.

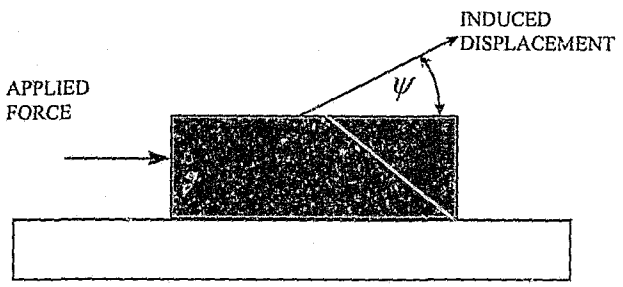

Figure 3.6 Dilation associated with sliding along a plane

In plasticity theory, unstable stress paths can be excluded by a plastic strain rate which is normal to the yield locus $f(\sigma)$. This behaviour was postulated by Drucker and Prager (1952) in order to assure material stability during yield. The postulate also guarantees unique solutions to the controlling equations. By assuming a plastic strain rate that is normal to the yield locus, it is effectively assumed that the dilation angle is equal to the angle of internal friction so that the yield function and the plastic potential function coincide. This is the theory of associative plasticity, which does not reflect observed behaviour in granular materials (Vermeer and de Borst, 1984; Stravropoulou, 1982)

In triaxial and shear testing of granular materials (cemented and uncemented), the results always indicate a lower value for the dilation angle than for the friction angle. In "Non-associated plasticity for soils, concrete and rock", Vermeer and De Borst (1984) abandon the concept of associated plasticity both on empirical and on theoretical grounds. It can be proven that no energy dissipation can take place during plastic deformation in the case of associative plasticity. As plastic deformation without energy dissipation is inconceivable, associative plasticity for granular materials is rejected from a theoretical point of view as well. By abandoning the concept of associated plasticity, material instability becomes possible. A potential for non-unique solutions (bifurcation) of the equations controlling equilibrium and constitutive behaviour therefore exists. Localisation of failure into shear bands is a direct result of the non-uniqueness of the solutions of the controlling equations.

A smoothly varying deformation pattern can suddenly change in such a way that all further deformations are localised in narrow so-called shear bands. If the width of a shear band is taken into consideration, a softening response can be expected, even though material softening may not occur. The explanation for this behaviour is that the material inside the shear band is subjected to different stresses than the material outside the shear band. Elastic unloading of the material outside the shear band is possible due to the development of a stress discontinuity in the stresses parallel to the shear band, between the inside and outside of the shear band, at the point of initiation of failure. Further inelastic deformation will only take place inside the shear band. This phenomenon is associated with the localisation of failure and can be observed in non-cohesive materials (Vermeer and de Borst, 1984).

The subject of localisation has been studied previously by Mandel (1964), Rudnicki and Rice (1975) and Vardoulakis (1980) and similar conclusions with respect to the shear band orientation and the critical hardening modulus have been reached by these researchers. Vermeer and de Borst (1984) however presented a simplified derivation of the localisation conditions in which the total strain rate is related to the total stress rate. In the following discussion the conditions for failure localisation will be investigated and the importance of the dilation angle will be demonstrated.

In plasticity theory a post-failure parameter h is introduced to account for the fact that the post-failure behaviour of materials during yielding is not perfectly plastic, but most often involves an increase in resistance (hardening) or a decrease in resistance (softening). This hardening or softening is a function of the strain and is not uniquely defined by the stresses. An effective strain parameter, $\bar{\varepsilon}^p$ is used to represent the plastic strains (Hill, 1950):

$$\bar{\varepsilon}^p = \int \sqrt{\frac{2}{3}(d\varepsilon_1^p d\varepsilon_1^p + d\varepsilon_2^p d\varepsilon_2^p + d\varepsilon_3^p d\varepsilon_3^p)}\, dt \tag{3.23}$$

and both the yield function $f(\sigma)$ and the plastic potential function $g(\sigma)$ are now defined as $f(\sigma, \bar{\varepsilon}^p)$ and $g(\sigma, \bar{\varepsilon}^p)$. The Mohr-Coulomb plastic potential function (3.10) can thus be rewritten as:

$$g(\sigma, \bar{\varepsilon}^p) = \tau^* - \sigma^* \sin\psi^* + \text{constant} \tag{3.24}$$

in which ψ^* is a function of the effective strain.

Using the flow rule from equation (3.9) and expressing the plastic potential function in terms of principal stresses and strains, it follows that:

$$g(\sigma, \bar{\varepsilon}^p) = \frac{1}{2}(\sigma_1 - \sigma_3) + \frac{1}{2}(\sigma_1 + \sigma_3)\sin\psi^* + C \text{ and thus} \tag{3.25}$$

$$\begin{bmatrix} d\varepsilon_1^p \\ d\varepsilon_2^p \\ d\varepsilon_3^p \end{bmatrix} = \lambda \begin{bmatrix} \frac{1}{2}(1-\sin\psi^*) \\ 0 \\ \frac{1}{2}(1+\sin\psi^*) \end{bmatrix} \tag{3.26}$$

Combining equation (3.23) and (3.26) it follows that

$$d\bar{\varepsilon}^p = \lambda\sqrt{\frac{1}{3}(1+\sin^2\psi^*)} \tag{3.27}$$

This equation provides a relationship between the effective strain, the mobilised dilation angle ψ^* and the plastic multiplier λ. This relationship is useful as it allows the plastic multiplier to be expressed in terms of parameters with a more physical meaning. Recalling that for plastic flow to occur, the stress point has to remain on the yield surface ($df = 0$) and the fact that the yield surface is a function of both the stress and the plastic strain ($f(\sigma, \bar{\varepsilon}^p)$), it follows that:

$$df = \frac{\partial f}{\partial \sigma} d\sigma + \frac{\partial f}{\partial \bar{\varepsilon}^p} d\bar{\varepsilon}^p = 0 \tag{3.28}$$

The post-failure parameter h is commonly referred to as the *hardening* parameter (negative values are related to softening). The hardening parameter h controls the expansion of the yield surface and is related to the plastic strain by:

$$h = -\frac{1}{d\lambda}\frac{\partial f}{\partial \bar{\varepsilon}^p} d\bar{\varepsilon}^p, \tag{3.29}$$

it follows that:

$$d\lambda = \frac{1}{h}\frac{\partial f}{\partial \sigma} d\sigma$$

and the flow rule from equation (3.9) can be rewritten as:

$$d\varepsilon^p = \frac{1}{h}\frac{\partial g}{\partial \sigma}\frac{\partial f}{\partial \sigma} d\sigma. \tag{3.30}$$

The physical meaning of this relation can easily be demonstrated by considering a tri-axial test in which the confining stresses $\sigma_2 = \sigma_3 =$ constant. The total stain rate in the direction of the principal stress is then:

$$d\varepsilon_1 = \frac{1}{E} d\sigma + \frac{1}{h}(1-\sin\psi^*)(1-\sin\phi^*) d\sigma \tag{3.31}$$

If the angles of friction and dilation would vanish, it is clear that the hardening parameter h has an equivalent physical meaning to the elasticity modulus E. The influence of both

internal friction angle and dilation angle lead to a more complicated situation, but the hardening parameter still affects the slope of the stress-strain curves and is therefore often referred to as hardening *modulus*.

With the expressions that have been obtained, localisation conditions will next be analysed and demonstrated, following the analysis of Vermeer and de Borst. The use of a (linear) Mohr-Coulomb failure criterion, a plastic potential of similar form and the assumption of an isotropic hardening rule, which is directly related to an effective plastic strain, is a simplification of real and more complex material behaviour. However, a clearer insight can be obtained by the use of these simple models without affecting the fundamental mechanisms involved in failure localisation.

For plane strain, the relation between the (total) strain rate and the stress rate is:

$$\begin{bmatrix} d\varepsilon_{xx} \\ d\varepsilon_{yy} \\ d\gamma_{xy} \\ d\varepsilon_{zz} \end{bmatrix} = \frac{1}{E}\begin{bmatrix} 1 & -\nu & 0 & -\nu \\ -\nu & 1 & 0 & -\nu \\ 0 & 0 & 2(1-\nu) & 0 \\ -\nu & -\nu & 0 & 1 \end{bmatrix}\begin{bmatrix} d\sigma_{xx} \\ d\sigma_{yy} \\ d\sigma_{xy} \\ d\sigma_{zz} \end{bmatrix} + \frac{1}{h}\frac{\partial g}{\partial \sigma}\left(\frac{\partial f}{\partial \sigma}\right)^{T}\begin{bmatrix} d\sigma_{xx} \\ d\sigma_{yy} \\ d\sigma_{xy} \\ d\sigma_{zz} \end{bmatrix} \tag{3.32}$$

Shear bands (localised failure) which are assumed to form in the local x-z plane, require stress continuity so that

$$d\sigma_{yy} = 0 \text{ and } d\sigma_{xy} = 0 \tag{3.33}$$

Kinematical restrictions which enforce deformation compatibility between the material inside the band and the surrounding material lead to additional constraints:

$$d\varepsilon_{xx} = 0 \text{ and } d\varepsilon_{zz} = 0 \tag{3.34}$$

As the out of plane stress σ_{zz} is the intermediate principal stress and the Mohr-Coulomb criterion is independent of the intermediate principal stress it follows that

$$\frac{\partial g}{\partial \sigma_{zz}} = \frac{\partial f}{\partial \sigma_{zz}} = 0$$

and equation (3.32) can be simplified to:

$$d\varepsilon_{xx} = 0 = \left(\frac{1}{E} + \frac{1}{h}\frac{\partial g}{\partial \sigma_{xx}}\frac{\partial f}{\partial \sigma_{xx}}\right)d\sigma_{xx} - \frac{\nu}{E}d\sigma_{zz} \tag{3.35a}$$

$$d\varepsilon_{yy} = \left(\frac{-\nu}{E} + \frac{1}{h}\frac{\partial g}{\partial \sigma_{yy}}\frac{\partial f}{\partial \sigma_{xx}}\right)d\sigma_{xx} - \frac{\nu}{E}d\sigma_{zz} \tag{3.35b}$$

$$\frac{\partial \phi}{\partial x_1}\frac{\partial \phi}{\partial x_2}\frac{\partial \phi}{\partial x_3} = \left(\frac{1}{r}\frac{\partial \phi}{\partial \psi}\frac{\partial \psi}{\partial r}\right) dx_1 dx_2 dx_3 \tag{۳.۲۲ج}$$

$$dx_1 dx_2 dx_3 - \frac{1}{E}dx_1 dx_2 dx_3 + \frac{\nu}{E}dx_1 dx_2 dx_3 = 0 \tag{۳.۲۲ب}$$

استبدال نتایج رابطه ۳.۲۲ج در رابطه ۳.۲۲ب منجر به

$$\nu = \frac{E - \frac{\partial \phi}{\partial x_1}\frac{\partial \phi}{\partial x_2}\frac{\partial \phi}{\partial x_3}}{4\nu - 1} \tag{۳.۲۵ج}$$

این معادله می‌تواند به صورت تابعی از مشتقات جزئی دوم تابع مشخصه تنش بیان شود که در روابط (۳.۲۰ج) تا (۳.۲۱ج) تعریف شده‌اند:

$$\left\{ \begin{aligned} &\frac{\partial \phi}{\partial x_1} = \left(\frac{1}{r}\right)\left(\frac{\psi_{yy}b - \psi_{xx}a}{r^2 r^*}\right)\left(\frac{1}{r}\right)\left(\phi^* \sin\theta + \frac{\psi_{yy}b - \psi_{xx}a}{r^2 r^*}\right), \quad \frac{\partial \phi}{\partial x_2} = \left(\frac{1}{r}\right)\left(\frac{\psi_{xx}a - \psi_{yy}b}{r^2 r^*}\right)\left(\psi^* \sin\theta + \frac{\psi_{xx}a - \psi_{yy}b}{r^2 r^*}\right), \\ &\frac{\partial \phi}{\partial x_3} = \frac{\psi_{xy}a}{r^2 r^*} \end{aligned} \right. \tag{۳.۲۶ج}$$

که می‌تواند بر حسب زاویه انحراف θ (شکل ۴.۳ را ببینید) به صورت زیر بیان شود

$$\left\{ \begin{aligned} &\frac{\partial \phi}{\partial x_1} = \frac{\partial \phi}{\partial \psi^*}\frac{\partial \psi^*}{\partial x_1} = \frac{1}{r}\left(\psi^* \sin\theta + \delta L\cos\theta\right), \quad \frac{\partial \phi}{\partial x_2} = \frac{\partial \phi}{\partial \psi^*}\frac{\partial \psi^*}{\partial x_2} = \frac{1}{r}\left(\phi^* \sin\theta + \delta L\cos\theta\right), \\ &\frac{\partial \phi}{\partial x_3} = \frac{\partial \phi}{\partial \psi^*}\frac{\partial \psi^*}{\partial x_3} = \frac{1}{r}\left(-\cos\theta + \sin\theta\right), \quad \frac{\partial \phi}{\partial \psi^*} = \frac{1}{r}\left(-\cos\theta + \sin\theta + \delta L\cos\theta\right) \\ &\frac{\partial \phi}{\partial \psi^*} = \frac{\partial \phi}{\partial \psi^*} \\ &\frac{\partial \phi}{\partial \psi^*} = \delta L \sin\theta \end{aligned} \right. \tag{۳.۲۷ج}$$

با جایگذاری دو رابطه اول از (۳.۲۷ج) در رابطه (۳.۲۵ج) برای تنش مماسی بی‌بعد به رابطه زیر می‌رسیم:

$$\eta = \frac{3 - \left(\psi^* \sin\theta + \delta L\cos\theta\right)\left(\phi^* \sin\theta + \delta L\cos\theta\right)}{4(\nu - 1)} \tag{۳.۲۸ج}$$

یا، به طور جایگزین:

$$\delta L\cos\theta = -\frac{1}{L}\left(\psi^* \sin\theta + \phi^* \sin\theta\right) \pm \sqrt{\frac{1}{L}\left(\psi^* \sin\theta - \phi^* \sin\theta\right)^2 - \frac{4(\nu - 1)\eta}{3}} \tag{۳.۲۹ج}$$

این معادله یک راه حل برای یک میدان تنش مماسی بی‌بعد در اطراف یک حفره با شکل عمومی ارائه می‌دهد. تنها جواب‌های مثبت برای η فیزیکی هستند. تمرکز تنش مماسی در مرز حفره برای یک میدان تنش یکنواخت دور از حفره به دست می‌آید

can be initiated. This critical value is such that the expression under the square root sign becomes zero and jump rotation (5E.3) is reached at:

$$\cos\Delta\xi_{cr} = -\frac{1}{\xi}\left(\sin\psi_{cr}\sin\phi_{cr}^{*} + \cos\left(\frac{\psi_{cr}^{*}}{\xi} + \frac{\phi_{cr}^{*}}{\xi}\right)\sin\psi_{cr}^{*}\right) = -\left(\frac{\psi_{cr}^{*}}{\xi} - \frac{\phi_{cr}^{*}}{\xi}\right)\cos(\sin\psi_{cr}^{*}) \tag{6A.3}$$

Assuming that the difference between the modified friction angle ϕ_{cr}^{*} and the modified lateral friction angle ψ_{cr}^{*} remains practically constant at the critical value, the corresponding rotation can be determined from the following relationship at large ξ and small rotations (6A.4):

$$\sin(\Delta\theta_{cr} - 90^{\circ}) = -\sin\left(\frac{\psi_{cr}^{*}}{\xi} + \frac{\phi_{cr}^{*}}{\xi}\right); \text{ for } \theta = \Delta\phi_{cr} + 2n\pi \tag{1A.3}$$

The critical horizontal gradient of the soil mass at which rotation starts can be calculated from (5E.3):

$$\mu_{cr}^{*} = \frac{\Sigma(\sin\psi_{cr}^{*}\sin\phi_{cr}^{*})}{\xi(\gamma^{2} - 1)\delta I} \tag{5A.3}$$

Figure (3.5) shows the relation between the horizontal gradient of the soil mass and the critical rotation angle at the start of rotation. It is assumed that the critical horizontal gradient ($\mu_{cr}^{*} = \psi_{cr}^{*}$) is equal to zero and the soil mass is in a neutral equilibrium. If the soil mass is loaded, the critical horizontal gradient will increase and the soil mass will be in an unstable equilibrium. The more realistic situations, where the modified friction angle is smaller than the modified friction angle, local rotation can in theory be initiated before the theoretical peak strength is reached.

Figure 3.5 Relation between horizontal gradient and shear bond instantaneous, based on jump rotation (5A.3)

While localization is theoretically possible at the critical hardening modulus, according to equation (3.42), and a unique shear band angle, according to equations (3.40) and (3.41), the localization process is normally delayed due to unfavourable boundary conditions. Such a delay would result in the inception of the shear band at values below the critical hardening modulus ($h \prec h_c$) and two possible orientations of the shear band as can be determined from equation (3.39). In the case where the hardening modulus is reduced to zero, while a non-associative flow rule ($\phi^* \prec \psi^*$) is applicable, equation (3.39) leads to the two potential solutions

$$\cos 2\theta = -\sin\phi^* \text{ and } \cos 2\theta = -\sin\psi^* \tag{3.43a}$$

Or, alternatively:

$$\theta = 45^o + \frac{\phi^*}{2} \text{ and } \theta = 45^o + \frac{\psi^*}{2} \tag{3.43b}$$

The first value is termed the Coulomb orientation as this is the orientation which would be obtained from a conventional analysis using the Mohr circle and the Coulomb failure criterion. The second value is called the Roscoe orientation (Roscoe, 1970).

By using the inverse form of (3.32), more information with respect to the behaviour of shear bands can be obtained. If the Poisson's ratio is assumed to be zero, the inverse of (3.32) can be expressed as:

$$\begin{bmatrix} d\sigma_{xx} \\ d\sigma_{yy} \\ d\sigma_{xy} \end{bmatrix} = E \begin{bmatrix} 1 - \dfrac{E\dfrac{\partial g}{\partial \sigma_{xx}}\dfrac{\partial f}{\partial \sigma_{xx}}}{h+d} & -\dfrac{E\dfrac{\partial g}{\partial \sigma_{xx}}\dfrac{\partial f}{\partial \sigma_{yy}}}{h+d} & -\dfrac{E\dfrac{\partial g}{\partial \sigma_{xx}}\dfrac{\partial f}{\partial \sigma_{xy}}}{2(h+d)} \\ -\dfrac{E\dfrac{\partial g}{\partial \sigma_{yy}}\dfrac{\partial f}{\partial \sigma_{xx}}}{h+d} & 1 - \dfrac{E\dfrac{\partial g}{\partial \sigma_{yy}}\dfrac{\partial f}{\partial \sigma_{yy}}}{h+d} & -\dfrac{E\dfrac{\partial g}{\partial \sigma_{yy}}\dfrac{\partial f}{\partial \sigma_{xy}}}{2(h+d)} \\ -\dfrac{E\dfrac{\partial g}{\partial \sigma_{xy}}\dfrac{\partial f}{\partial \sigma_{xx}}}{h+d} & -\dfrac{E\dfrac{\partial g}{\partial \sigma_{xy}}\dfrac{\partial f}{\partial \sigma_{yy}}}{h+d} & \frac{1}{2} - \dfrac{E\dfrac{\partial g}{\partial \sigma_{xy}}\dfrac{\partial f}{\partial \sigma_{xy}}}{2(h+d)} \end{bmatrix} \begin{bmatrix} d\varepsilon_{xx} \\ d\varepsilon_{yy} \\ d\gamma_{xy} \end{bmatrix} \tag{3.44}$$

where $$d = E\left(\frac{\partial f}{\partial \sigma_{xx}}\frac{\partial g}{\partial \sigma_{xx}} + \frac{\partial f}{\partial \sigma_{yy}}\frac{\partial g}{\partial \sigma_{yy}} + \frac{1}{2}\frac{\partial f}{\partial \sigma_{xy}}\frac{\partial g}{\partial \sigma_{xy}}\right) \tag{3.45a}$$

Using the expressions in (3.37) it follows that:

$$d = \frac{E}{2}\left(1 + \sin\phi\sin\psi\right) \tag{3.45b}$$

The parameter d thus has a value which is of the order of magnitude of the elasticity modulus E. The hardening modulus h has a critical (maximum) value which is at least an order of magnitude smaller (see for instance equation 3.42) and can therefore be neglected in equation (3.44).

In the following example a shear band experiment, in which the boundary conditions are such that after the formation of a shear band load shedding is possible, is analysed. The material outside the shear band remains in an elastic state and, due to the possibility of load shedding, elastic unloading may take place outside the shear band. The material inside the shear band must be yielding plastically in order to obtain large shear deformations. Before the onset of shear banding, stress and strain rates are equal throughout the specimen, but as soon as the shear band has developed, discontinuous behaviour may occur. In Figure 3.8 the experiment and the associated loading configuration are shown. The x-axis is chosen along the direction of the shear band and the following conditions need to be satisfied:

$$d\varepsilon_{xx}^{in} = d\varepsilon_{xx}^{out} \qquad \text{(kinematical compatibility)} \qquad (3.46a)$$

$$d\sigma_{yy}^{in} = d\sigma_{yy}^{out};\ d\sigma_{xy}^{in} = d\sigma_{xy}^{out} \qquad \text{(equilibrium requirement)} \qquad (3.46b)$$

$$d\sigma_h = 0;\ d\sigma_v \le 0 \qquad \text{(external loading conditions)} \qquad (3.46c)$$

where the *in* and *out* superscripts refer to conditions inside and outside the shear band respectively

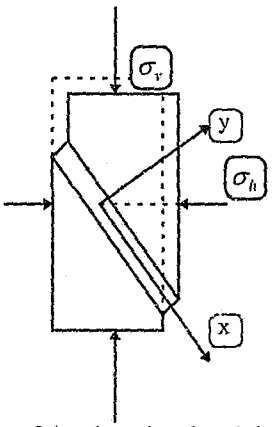

Figure 3.8 Orientation of the shear band and the local axes

Using Mohr's circle (Figure 3.4) and the condition $d\sigma_h = 0$, it follows that the stress rates outside the band can be expressed in terms of the vertical stress rate:

$$d\sigma_{xx}^{out} = \frac{1}{2}(1-\cos 2\theta)d\sigma_v$$

$$d\sigma_{yy}^{out} = \frac{1}{2}(1+\cos 2\theta)d\sigma_v \qquad (3.47)$$

$$d\sigma_{xy}^{out} = \frac{1}{2}\sin 2\theta \sigma_v$$

The stress rates inside the shear band are given by equation (3.46) so that

$$\begin{aligned} d\sigma_{yy}^{in} &= \left(-\frac{E(-\cos 2\theta + \sin\psi)(\cos 2\theta + \sin\phi)}{2(1+\sin\phi\sin\psi)}\right)d\varepsilon_{xx} \\ &+\left(E - \frac{E(-\cos 2\theta + \sin\psi)(-\cos 2\theta + \sin\phi)}{2(1+\sin\phi\sin\psi)}\right)d\varepsilon_{yy} \\ &+\left(\frac{E}{2} - \frac{E(-\cos 2\theta + \sin\psi)\sin 2\theta}{2(1+\sin\phi\sin\psi)}\right)d\gamma_{xy} \end{aligned} \tag{3.48}$$

and

$$\begin{aligned} d\sigma_{xy}^{in} &= \left(-\frac{E(\sin 2\theta)(\cos 2\theta + \sin\phi)}{1+\sin\phi\sin\psi}\right)d\varepsilon_{xx} \\ &+\left(\frac{-E(\sin 2\theta)(-\cos 2\theta + \sin\phi)}{1+\sin\phi\sin\psi}\right)d\varepsilon_{yy} \\ &+\left(\frac{E}{2} - \frac{E\sin^2 2\theta}{1+\sin\phi\sin\psi}\right)d\gamma_{xy} \end{aligned} \tag{3.49}$$

As the Poisson's ratio has been chosen to be equal to zero and the parallel strain rate outside the shear band is equal to the parallel strain rate inside the band (4.47a) it follows that

$$d\varepsilon_{xx}^{out} = d\varepsilon_{xx}^{in} = \frac{d\sigma_{xx}}{E} \tag{3.50}$$

Substituting this expression in (3.48) and (3.49) ultimately results in the following proportionality

$$d\sigma_{v(ertical)} \propto E(\cos 2\theta + \sin\psi)(\cos 2\theta + \sin\phi)d\gamma_{xy} \tag{3.51}$$

This proportionality indicates that, at the *onset* of shear banding, the vertical stress does not change for two particular values of θ, namely

$$\cos 2\theta = -\sin\psi \text{ so that } \theta = 45^o + \frac{\psi}{2} \text{ (Roscoe orientation)}$$

$$\cos 2\theta = -\sin\phi \text{ so that } \theta = 45^o + \frac{\phi}{2} \text{ (Coulomb orientation)}$$

For shear band orientations outside the range of the R oulomb orientations the vertical pressure should increase, which would ·· on of elastic unloading outside the shear band. For this reason only in Roscoe-Coulomb range

are possible. Intermediate inclinations all result in an initial decrease of the vertical pressure and the maximum rate of softening is obtained for the intermediate inclination $\theta_A = 45^o + \frac{\phi + \psi}{4}$.

The stresses *inside* the shear band have to remain on the yield surface during plastic yielding. This consistency condition can be expressed as

$$\frac{\partial f}{\partial \sigma} = \frac{\partial f}{\partial \sigma_{xx}} d\sigma_{xx} + \frac{\partial f}{\partial \sigma_{yy}} d\sigma_{yy} + \frac{\partial f}{\partial \sigma_{xy}} d\sigma_{xy} = 0 \tag{3.52}$$

Substituting the values from (3.47) for $d\sigma_{yy}^{out}$ and $d\sigma_{xy}^{out}$, and recalling that these stress rates are equal to the stress rates inside the shear band, according to condition (3.46b), it follows that

$$d\sigma_{xx}^{in} = \frac{1}{2}\left(\frac{1 + \cos 2\theta + \sin^2 2\theta - \sin\phi - \cos 2\theta \sin\phi}{\cos 2\theta + \sin\phi}\right) d\sigma_v \tag{3.53}$$

The band parallel stress rate outside the shear band can be found from equation (3.47) as well and the difference between the band parallel stress rate inside and outside the shear band can be expressed as

$$d\Delta\sigma_{xx} = d\sigma_{xx}^{in} - d\sigma_{xx}^{out} = \frac{1 - \sin\phi}{\cos 2\theta + \sin\phi} d\sigma_v \tag{3.54}$$

and, by substituting the vertical stress rate proportionality (3.51):

$$d\Delta\sigma_{xx} \propto (\cos 2\theta + \sin\psi) d\gamma_{xy} \tag{3.55}$$

The last equation shows that a stress discontinuity will develop across the boundaries of a shear band except for the case where $\cos 2\theta + \sin\psi = 0$ (Roscoe orientation). An extreme value for the stress discontinuity will be obtained for the Coulomb orientation:

$$d\Delta\sigma_{xx} \propto (-\sin\phi + \sin\psi) d\gamma_{xy}. \tag{3.56}$$

Although, at the onset of shear banding the vertical stress rate is zero for the Coulomb orientation (see equation 3.51), a discontinuity in the stress rate parallel to the shear band arises. This discontinuity in band parallel stress is associated with a rotation of the principal stresses inside the shear band, which therefore also reaches a maximum in the case of a Coulomb shear band orientation. In fact, the principal stresses inside the shear band will rotate with increasing shear deformation until they assume an orientation which corresponds to the Roscoe orientation (Figure 3.9). At that stage all stress rates vanish and no further softening is possible as residual values have been reached. The rotation of principal stresses inside the shear band involves a reduction of the band parallel stress, and consequently also of the principal stresses themselves. A maximum rotation can be

obtained from a shear band which has assumed the steepest orientation, namely the Coulomb ($\theta = 45^o + \frac{\phi}{2}$) orientation ($\theta_C$). This rotation also involves the largest reduction in principal stresses (Figure 3.9) and thus leads to the maximum amount of softening. The Roscoe orientation (θ_R) does not lead to any stress changes as no stress rotations inside the band can be accommodated for this orientation and is therefore not associated with a softening response. Any intermediate orientation will result in an intermediate amount of softening. Of particular interest is the intermediate orientation $\theta_A = 45^o + \frac{\phi - \psi}{4}$, which results in a maximum initial rate of softening. The previously described shear band orientations have been used in the following Figure 3.9 to demonstrate their effect on the stress changes and rotations after the onset of bifurcation, together with the associated shear band formation.

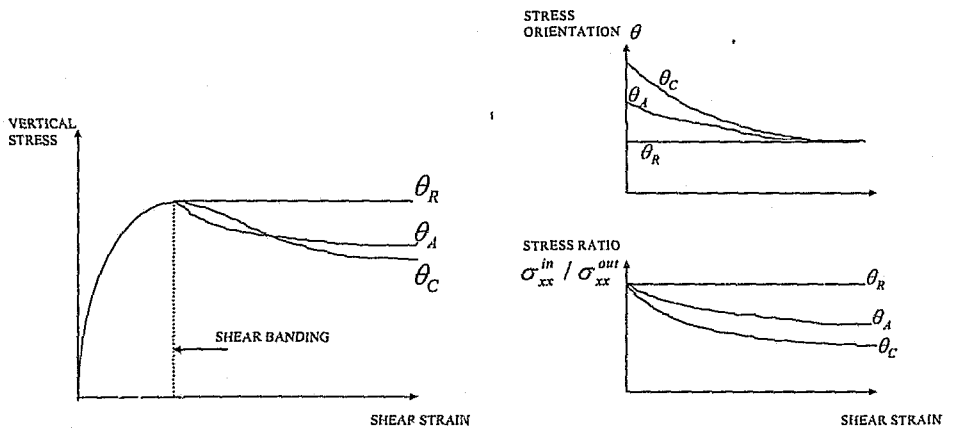

Figure 3.9a Stress-strain relations for various possible shear band orientations (after Vermeer and de Borst, 1984)

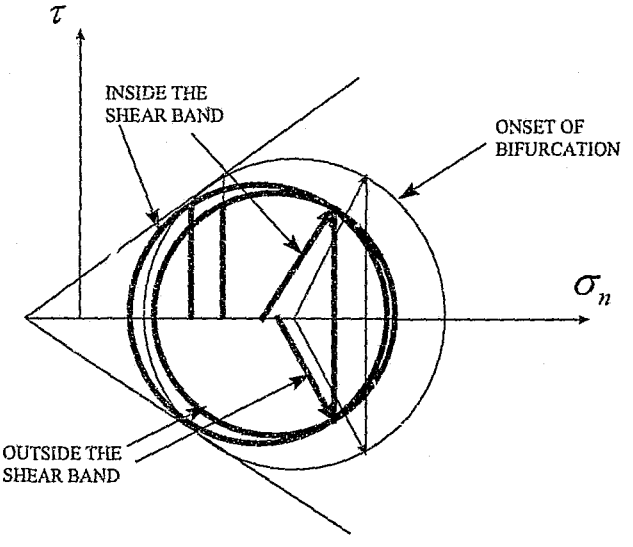

Figure 3.9b Bifurcation with associated softening and stress rotations inside the shear band (non Roscoe orientation)

Another way of describing the softening behaviour of the shear band is by analysing the effective friction angle α of the shear band. The definition of this parameter for a cohesion-less material is:

$$\tan\alpha = \left(\frac{\sigma_{yy}}{\sigma_{xy}}\right) \tag{3.57}$$

Recalling the yield function from (3.8) and using the condition $f(\sigma) = 0$ it follows, with the aid of the Mohr circle in Figure 3.4, that

$$\tan\alpha = \frac{\sin 2\theta \sin\phi}{1+\cos 2\theta \sin\phi} \tag{3.58}$$

This equation implies that the effective friction angle is directly related to the orientation of the shear band with respect to the principle stresses *inside* the shear band. If a shear band assumes the Coulomb orientation it follows from equation (3.58) that $\tan\alpha = \tan\phi$ which coincides with the Coulomb theory of a shear failure plane in the most critical orientation. However, after the process of stress rotations inside the shear band has been completed, a residual value for the effective friction angle can be derived from (3.58):

$$\tan\alpha = \frac{\cos\psi \sin\phi}{1-\sin\psi \sin\phi} \tag{3.59}$$

The effective friction angle accounts for the fact that inside the shear band, stress rotation has resulted in a reduction in principal stresses. In the case of a non dilating material ($\psi = 0$), equation (3.59) results in $\tan\alpha = \sin\phi$, while in the case of an associative flow rule ($\psi = \phi$) the residual ratio would again be $\tan\phi$ as in the case of the critical Coulomb orientation. No stress discontinuity or stress rotation is associated with these cases as can also be appreciated from equation (3.56). If the orientation of the shear band itself is at the Roscoe angle ($\theta = 45^0 + \frac{\psi}{2}$), it follows that the effective friction angle is expressed by equation (3.59). The reduced friction angle can in this case be explained directly from the fact that the orientation of the shear band is less critical than would be predicted from the Coulomb theory. In order to initiate shear failure in this direction, with the same loading conditions, a reduction in the effective resistance along the shear band as expressed by (3.59) is required. The lowest residual stresses will be obtained for that case where the residual effective friction angle as per (3.59), in combination with an admissible orientation of the shear band, would lead to a minimum (residual) value for the vertical stress. This condition is met when the shear band is orientated in the steepest possible angle, which is the critical Coulomb orientation. The reduction in strength is simply the ratio between the residual vertical stress and the peak vertical stress. As the horizontal stress is not allowed to vary, it follows from the Coulomb criterion and Mohr's stress circle that:

$$\sigma_v = \frac{1+\sin\alpha}{1-\sin\alpha}\sigma_h \tag{3.60}$$

If the shear band assumes the critical Coulomb orientation the effective friction angle α at peak strength is equal to the internal friction angle ϕ according to equation (3.58) and the residual strength is associated with a residual friction angle which can be derived from (3.59). Using equation (3.60), the ratio between the residual vertical stress and the peak vertical stress can be expressed as:

$$\text{ratio} = \frac{1+\sin\alpha}{1-\sin\alpha}\frac{1-\sin\phi}{1+\sin\phi} \tag{3.61}$$

whereby α can be obtained from (3.59)

Typical values for the effective friction angle α, and the ratio between residual and peak stress are listed in table 3.1

ϕ (degrees)	ψ (degrees)	α (degrees)	maximum stress ratio
30	0	26.57	0.87
30	10	28.33	0.94
30	20	29.55	0.98
30	30	30	1.00
40	0	32.73	0.73
40	10	35.47	0.82
40	20	37.75	0.90
40	30	39.36	0.97
40	40	40	1.00

Table 3.1 Relation between internal friction angle, dilation angle, effective friction angle and the ratio between the peak and residual stress (Coulomb shear band orientation)

Table 3.1 reflects the extreme case of stress rotations and associated softening for the Coulomb orientation of a shear band ($45^o + \phi/2$). The other extreme case in which no stress rotations or associated softening takes place, occurs when the shear band assumes the Roscoe orientation ($45^o + \psi/2$). Intermediate orientations would lead to intermediate values for softening and stress rotations. The term softening in this context only refers to softening which is directly induced by stress rotations and does not address material softening related to physical process such as bond breakage.

The onset of failure is assumed to initiate at a point in the medium when the stress state σ reaches a critical condition satisfying a yield function $f(\sigma) = 0$. Once this critical condition has been reached and failure is initiated, the total strain can be expressed as

$$\varepsilon = \varepsilon^e + \varepsilon^p \tag{3.62}$$

where ε^e represents the elastic strain tensor and ε^p the non linear plastic strain tensor.

The inclination of the shear bands varies between the limits of the so-called Roscoe orientation of $45^o + \psi/2$ and the Coulomb orientation of $45^o + \phi/2$, whereby the last one corresponds to the lowest residual strength and therefore appears to be the preferred orientation. The theoretical analysis in combination with the results from biaxial experiments indicates, however, that the drop in parallel stresses inside the shear bands results in out-of-balance forces at the extremities of the shear bands which may or may not be equilibrated locally. In the case of relatively thick shear bands (coarser granular material) these out-of-balance forces will be relatively large, in which case the weakest failure mechanism is suppressed and the inclination of the shear band will tend to approach the steeper Roscoe inclination, which is associated with higher residual stresses. In real situations, with complex mechanisms and constraints, any orientation between the two limiting extremes can be expected. The onset of localisation (bifurcation of the solution) in a hardening granular material is possible before the peak strength has been reached if non associative plasticity is assumed. In the case of associative plasticity (dilation angle = angle of internal friction) localisation is only possible during softening of the material, after the peak strength has been reached.

In order to evaluate possible applications of the theory, relevant numerical simulations will be analysed in the next section. As the theory does not address fracture growth, but only predicts potential fracture locations, it can be expected that the processes which lead to the formation of shear bands are still not sufficiently captured by this theory. The issue of material softening is also not addressed by the theory, although it is implicitly assumed that the theory is suitable both for (cohesion-less) soils as well as for cemented granular materials such as concrete and rock. The breaking of bonds in the cemented materials ultimately leads to material softening and thus brittle failure. According to the theory, failure localisation can occur *before* the peak strength has been reached and softening has initiated. This immediately implies that failure localisation in brittle materials can be simulated even if the softening processes are ignored. These issues are also addressed in the next section.

3.3 NUMERICAL SIMULATIONS OF SHEAR LOCALISATION

The computer programme FLAC has been used to analyse (shear) failure localisation in uniformly stressed tri-axial tests. The main advantage of this particular programme is its efficiency in dealing with unstable processes, due to the formulation of its dicretisation and solution schemes (Marti and Cundall, 1982). FLAC is a two dimensional, explicit, finite difference code. Plane strain is the standard condition, but plane stress and axi-symmetry can also be selected. A grid, which is formed by individual elements, or zones, can be adjusted to fit the shape of the object to be represented. A Lagrangian formulation, in which incremental displacements are added to the grid nodes at each iteration, allows for simple accommodation of large strains and displacements. The Mohr Coulomb failure model, with effective hardening (and softening) behaviour, has been applied in the following simulations.

In order to encourage localization of failure to occur in a "natural" way, a small random deviation of the internal friction angle was imposed in the first series of simulations. Such a condition allows for failure to initiate at arbitrary locations inside the material rather than at locations which can be affected by minor non-uniformities, such as the boundaries. Three parameters have been investigated, namely the friction angle, the dilation angle and the confining stress. Figure 3.10 shows the results from a simulation in which a friction angle of 40° (deviation 1°) and a dilation angle of 0° was used. No horizontal confining stress was applied in this case and vertical load was applied by forcing the top boundary slowly down (displacement controlled). All the models presented in the following consisted of 50x150 square elements.

Localisation of failure occurs in the form of a pattern of shear bands which appear to be orientated somewhere between the extreme theoretical values of 45° and 65° for the Roscoe angle and the Coulomb angle respectively. Of interest also, is the stress-strain relationship which indicates a (small) decrease in stress during the post failure stage. The unstable nature of this graph cannot readily be explained, but may be associated with excessive loading velocities in the numerical model. The softening behaviour is however represented and can be attributed to stress rotations inside the shear bands which assume orientations of approximately 50°.

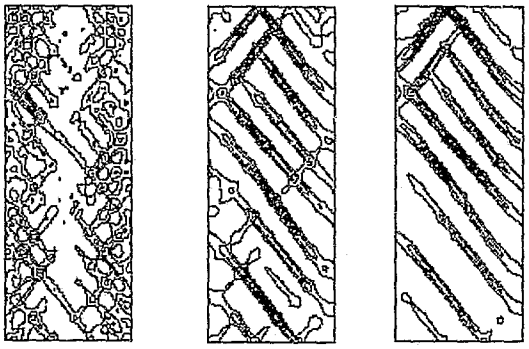

Figure 3.10 Consecutive stages of failure localisation in a uni-axially loaded specimen (FLAC). Cohesion=10MPa, friction angle = 40° and dilation angle = 0°.

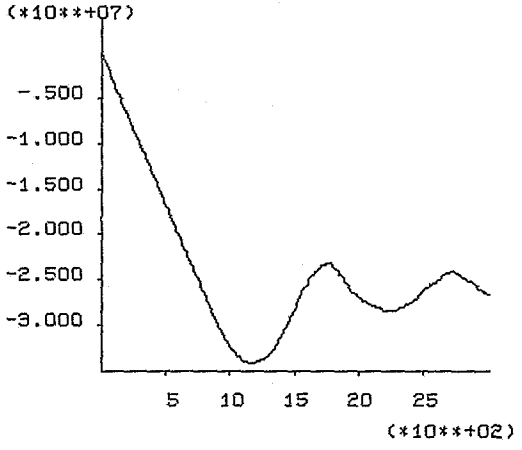

Figure 3.11 Stress-strain relation for the simulation shown in Figure 3.10

Figure 3.12 shows the results of a simulation in which the dilation angle was increased to 30° while the other parameters remained unchanged. The theoretical values range from 60° for the Roscoe angle to 65° for the Coulomb angle in this case. Localisation of failure does not appear to occur spontaneously as in the previous case and only limited evidence of strain softening can be noticed. The orientation of the shear band is steeper in this case with values of about 55°, which can be attributed to the effect of the dilation angle. The minimum theoretical value, the Roscoe angle, is however slightly larger, namely 60°.

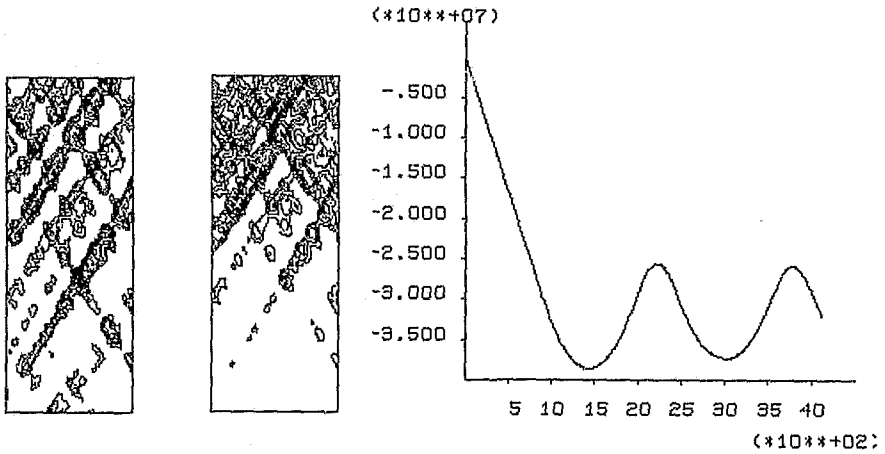

Figure 3.12 Results from a simulation in which the dilation angle was increased to 30^0

In another simulation, properties were uniform except for a single weak flaw that was introduced in the centre of the specimen. The results, which are shown in Figure 3.13, demonstrate how the theory of plasticity also effectively controls the propagation of shear bands in a numerical application. The theory itself does not address the development of failure localisation, but only deals with potential shear band orientations.

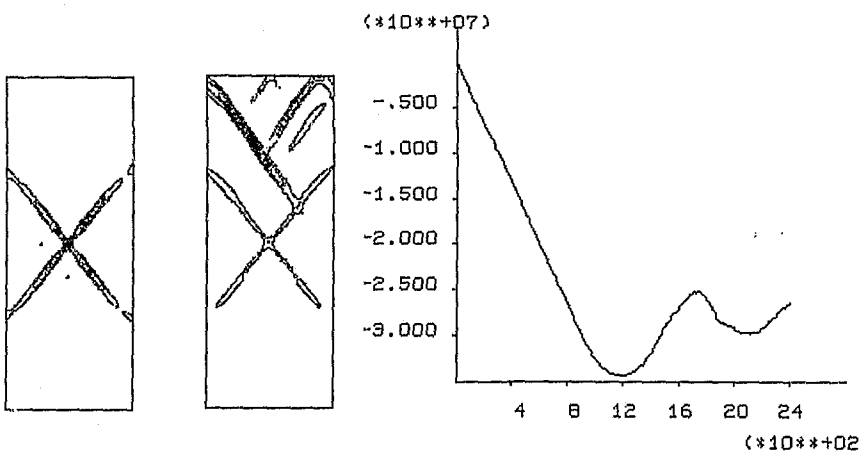

Figure 3.13 Development of shear zone from a flaw in the centre of the specimen; no confinement, friction = 40° and dilation = 0°

It is clear from figure 3.13 that an initial development of shear failure from the flaw in the centre of the specimen is followed by the failure localisation initiating from the top corners

of the specimen. In both cases propagation of failure can be observed and the orientation of the band is approximately 50° as in the first example without the central flaw.

These results indicate the potential application of the theory of plasticity with respect to failure localisation in a continuum. As has been mentioned before, brittle failure is assumed to occur after failure localisation has taken place. In the following examples a so-called strain softening model is used. Brittle failure is simulated by allowing the material strength to decrease as a function of plastic strain. The parameter which controls the strength is the cohesion and two cases have been simulated with varying relations between the cohesion and the plastic strain. In the first case (Figure 3.14), a relatively slow decrease of strength with respect to plastic strain is simulated, while in the second case (Figure 3.15) a more rapid decrease of strength with respect to plastic strain, is assumed.

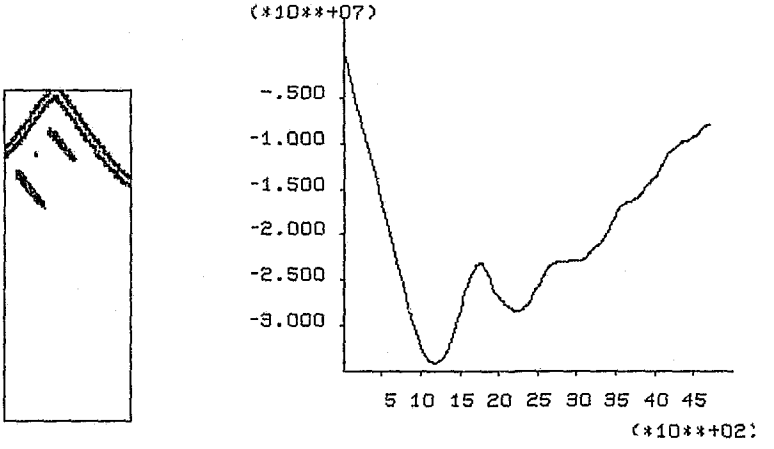

Figure 3.14 Contours of damage and the stress-strain relation for a strain softening model. no confinement, angle of internal friction = 40° and dilation angle = 0° cohesion reduces from 10MPa to 0MPa as the material undergoes plastic strains between 0.5% and 1%.

The amount of plastic strain required to induce strength loss and thus damage is relatively large in the simulation of Figure 3.14. Only a few bands near the top of the specimen are "frozen" and become permanently damaged. The reason for the location of these bands near the top is unfortunately related to the fact that deformations are introduced there as this is the position of the "loading platen". This influence appears to become increasingly dominant with advanced deformation. Similar effects can also be observed in Figures 3.10, 3.12 and 3.13. Slower loading rates may overcome this (numerical) problem as can be appreciated by comparing Figure 3.15 with Figure 3.16. The loading velocity used for the result in Figure 3.16 has been decreased to 10% of the velocity which was applied in the model represented in Figure 3.15. This serves to demonstrate how sensitive the localisation process is with respect to irregularities in stress distribution.

In the next two examples the softening rate has been increased in order to investigate the effect of an increased "brittleness".

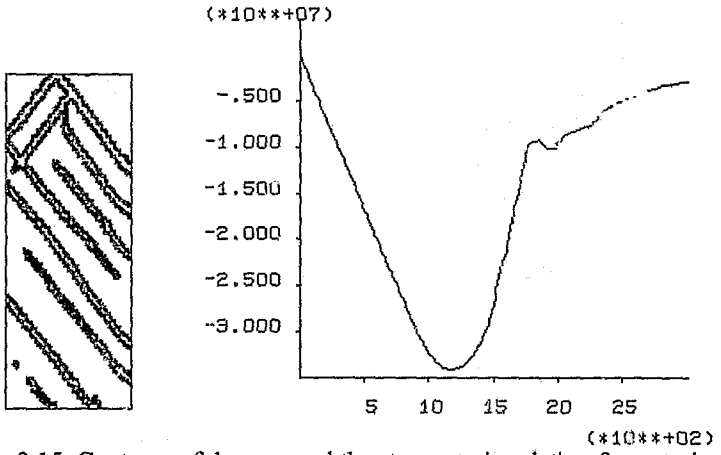

Figure 3.15 Contours of damage and the stress-strain relation for a strain softening model. no confinement, angle of internal friction $=40^{o}$ and dilation angle $=0^{o}$ cohesion reduces from 10MPa to 0MPa between a plastic strain of 0.1% and 0.2%

While the amount of plastic strain required to induce damage is relatively small in this example, shear bands become affected at an early stage of the deformation process, which results in a more regular distribution of cohesion-less shear bands. It is of interest to note that the spacing of these shear bands seems to be related to the loading rate as well This is demonstrated in the next simulation in which the loading rate has been reduced to 10% of the loading rate which was applied in this example. All other parameters remained unchanged.

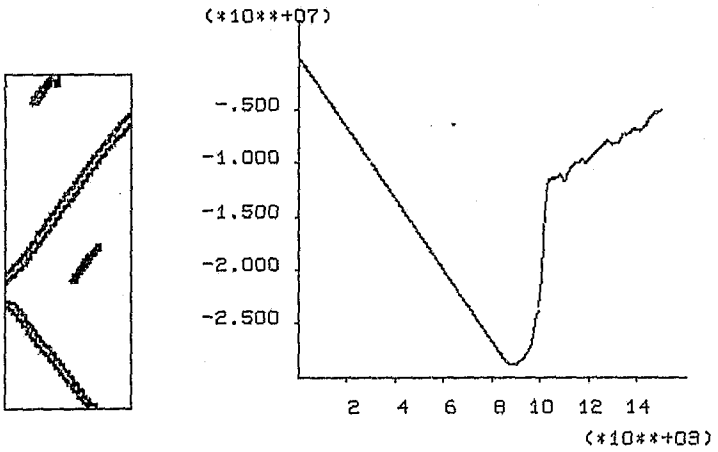

Figure 3.16 Contours of damage and the stress-strain relation for a strain softening model. no confinement, angle of internal friction = 40° and dilation angle = 0° cohesion reduces from 10MPa to 0MPa between a plastic strain of 0.1% and 0.2%; loading rate reduced to 10% with respect to Figure 3.15

As the loading rate is reduced, a reduced number of shear bands appear to dominate. The explanation for this phenomenon is likely to be found in the stress distribution associated with both the fast and slow loading rates. In the case of the fast loading rate, the influence of (plastic) failure spreads with a relatively low speed compared to the loading velocity. As a consequence, the influence of a shear band is only noticed in its immediate environment and spacing between individual shear bands is therefore relatively small. With a slow loading rate, the influence of a developing shear band can spread much further and a larger spacing between individual shear bands can be obtained. Both cases are of interest as rapid loading may be realistic under certain circumstances and apparently could lead to the formation of a multitude of shear bands and fractures, while a reduced loading rate appears to limit the number of these features.

In the following example an irregular stress distribution has been simulated by introducing a horizontal slot in the specimen. Stress concentrations near the tip of the notch will cause the initiation of failure at that location and numerical artefacts will be dominated to a large extent by the high stress gradient in this case. The same softening parameters are used as in the previous two examples and the relative velocity which was selected is the slower one. The tip of the notch is located exactly in the middle of the specimen.

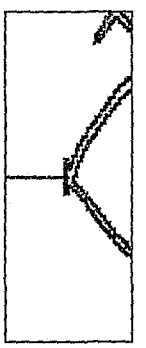

Figure 3.17 Shear fractures propagating from the tip of a compressed notch. Properties as in Figures 3.15 and 3.16

The initiation and propagation of a shear fracture, from a location of high stress concentration, has effectively been reproduced in this example. Localisation of failure is caused by plastic processes, after which brittle damage takes place in those localised areas of failure.

3.4 CONCLUSIONS

While the theory of failure localisation addresses the formation of shear bands in materials which undergo plastic deformations, it remains questionable whether the micro fracture processes which ultimately lead to failure in cemented materials can also be described adequately by this theory. If localisation of failure occurs before brittle failure has initiated, it makes perfect sense to apply plasticity theory in order to determine potential failure

localisation. However, if brittle failure processes control the localisation of failure it becomes very questionable whether the theory of plasticity can be applied to represent the localisation of failure. As has been shown in the numerical simulations, growth of shear bands is effectively represented and some form of "plastic process zone" precedes the formation of the shear band. This does not automatically follow from the theory, but is a logical and useful extension of the theory when applied in a suitable numerical model.

Shear fractures must have undergone some form of brittle failure during or after their formation in cemented materials. The use of a so called strain softening model should in theory be able to represent this brittle (softening) behaviour as well. The examples which have been presented in the previous section have demonstrated that numerical applications can also reproduce such brittle behaviour by inducing damage in localised failure zones which are subjected to excessive plastic straining. This is an additional extension to the theory of plasticity as implemented in the numerical model used here. In summary, a tool is available for the simulation of shear fracture formation and propagation which is based on the assumption that the material can be represented as a continuum, that failure takes place due to excessive shear stresses and that post failure deformations take place according to a "flow" rule. Brittle behaviour does not directly affect the fracture formation processes, but can be included as a property which affects the behaviour of the fracture after formation.

However, the use of strain softening models can lead to numerical problems. While these problems have been avoided in the examples presented here, they can easily occur and affect the results. The major problem is associated with the grid influence on shear band angles. As the softening rate is related to the (plastic) strain and the strain is inversely proportional to the thickness of the shear band, it follows that the narrowest possible bands will be favoured. The smallest width that can be resolved by the grid is one element if the band is parallel to the grid or approximately three elements if the band cuts across the grid in any other direction. It is for this reason that shear bands prefer to align themselves with the grid. A related problem is the dependency of the resulting load deformation relation on the size of the zones being used. Smaller zones will lead to a more brittle behaviour as narrower bands are generated.

The problems indicated in the previous paragraph are directly related to the continuum formulation of the plasticity theory. The thickness of shear bands is not defined within this theory, although a non zero width is required to meet physical requirements of the volumetric representation. The minimum band width is dictated by the element size in a numerical model, while internal features, such as grain size, may determine the thickness of a shear band in a particular material. It is therefore necessary that some sort of length scale is included in any constitutive model which is to represent internal material features.

Finally, the fact that large numbers of elements have to be used in order to accommodate these shear bands and the fact that the loading rate may also have an effect on the occurrence of these bands results in major demands on computing time and power.

While it has been demonstrated that the simulation of shear fractures is theoretically possible with the use of the localisation theory, it is not clear that such simulated fractures are representative of physical behaviour. If a particular material can effectively be treated

as a continuum before the onset of brittle failure, it may be feasible to describe the behaviour of such a material with the use of plasticity theory. In that case relatively simple constitutive models can be calibrated against observed material responses. If, on the other hand, the localisation of failure in a particular material is directly influenced and controlled by its micro structure, the theory of plasticity may not be (directly) applicable. In that case the micro structure has to be represented explicitly.

In the following section the assumption of plastic failure preceding the brittle failure processes is abandoned and an attempt is made to represent shear fracturing directly by alternative fracture criteria. The advantage of such an approach is that it would allow a far more efficient means of representing shear fracturing by discrete elements in an elastic continuum. This approach is an alternative to the localisation theory and it does not address the problems which localisation theory involves with respect to the effect of a controlling micro structure. The medium in which the discontinuity is located is assumed to be a linear elastic continuum and fracture propagation is determined by the (elastic) stress distribution around the fracture tip.

4.0 THE SEARCH FOR A SHEAR FRACTURE CRITERION

4.1 INTRODUCTION

Although the terms shear fracture and shear band have been used rather arbitrarily throughout this thesis, a clear distinction should be made between the two concepts. Shear bands are associated with the localisation of failure in more or less uniformly stressed materials and are preceded by micro fracturing processes in brittle materials. Uniformly distributed shear deformations become ultimately concentrated in relatively narrow zones or bands assuming inclinations which appear to be favourable for the dissipation of strain energy. The Mohr-Coulomb theory is well suited to capture this mechanism which has been described in the previous chapters. The formation of shear bands in brittle materials has not been reproduced directly with any of the previously discussed models, as the softening models in FLAC do not reproduce the micro fracturing in any detail. It is, however, suggested that the mechanism of shear band formation is, in principle, similar in plastic and in brittle materials. The difference is associated with the micro fracturing processes which precede the formation of a shear band in brittle materials. Once a critical density of micro fractures has been obtained and non linear and non elastic (shear) deformations can be accommodated by the micro fractured material, the localisation process can be initiated in such a material as well. Brittle failure subsequently occurs when rock bridges between individual micro fractures collapse and cohesion effectively disappears. Shear banding is defined here as a *collapsing* mechanism whereby localisation of failure takes place in areas which have previously undergone more or less uniform, plastic deformations. Although *propagation* of shear bands has been represented with the numerical models in the previous chapter, it is questionable if propagation of plastic failure is realistically reproduced with these models.

Shear fractures are defined here as individual fractures which propagate in a direction which is inclined with respect to the major principal stress axes. The processes which control this propagation are concentrated near the fracture front in an area which is termed the process zone. Shear fractures are not only mode II fractures in which shear slip along the fracture is the source of the stress concentrations around the fracture tip, but they also propagate approximately along a path which is an extension of the initial mode II fracture. This distinguishes them from mode II fractures which propagate typically in the form of wing cracks. These wing cracks are effectively opening mode fractures which follow a propagation path which is most suitably simulated by a fracture criterion which is controlled by critical tensile strength. These fractures are often inappropriately termed 'shear fractures'. An alternative fracture criterion needs to be applied in order to simulate true shear fracturing as defined here, especially if the medium is assumed to be a continuum.

Various alternatives can obviously be used, but a very likely criterion appears to be the "Excess Shear Stress" (ESS) criterion, which is based on the Mohr-Coulomb criterion and which states that fracture propagation takes place in a direction which assumes a particular inclination with respect to the principal stresses. This inclination is that one at which the difference between the shear stress acting along the fracture plane and the frictional resistance induced by the normal stresses across that plane is maximal. Fracture propagation is activated once a critical value for the ESS is reached. The angle between the

major principal stress and the direction of fracture propagation can be derived by differentiating the Coulomb yield function (3.8) with respect to the inclination θ. Both shear and normal stress can be expressed as functions of θ by applying stress transformation equations to the case shown in Figure 3.4. This results in the critical Coulomb orientation:

$$\theta = 45^0 - \frac{\phi}{2} \tag{4.1}$$

where ϕ is the friction angle which represents the frictional resistance along the fracture surface.

The ESS criterion itself is expressed by

$$ESS = |\tau| - \sigma_n \tan\phi \tag{4.2}$$

where τ is the shear stress acting along the fracture plane and σ_n is the normal compressive stress acting perpendicular to the fracture plane. The (shear) fracture plane is defined as being parallel to the direction of the intermediate principal stress which, in plane strain applications, is assumed to be the out of plane direction.

It is assumed indirectly that the fracture plane orientates itself in such a way that the shear stresses will be most efficiently employed. No further physical interpretations of the fracture processes are incorporated into this fracture criterion which in effect is a direct application of the Mohr-Coulomb failure criterion. While the Mohr-Coulomb failure criterion is adequately suited to reproduce localisation of failure in the form of shear bands in a continuum model, it appears that it is more applicable to materials which demonstrate a certain amount of ductility, rather than to extremely brittle materials (Labuz et. al., 1996). Failure in the more brittle materials consists of complex interactions of micro cracks which are more likely to cause macroscopic shear fracture. Thus an appropriate (macro) shear fracture criterion should be able to capture the essential effects of these interacting mechanisms in a global sense. While it remains questionable if a macroscopic shear fracture can be represented by a single propagating fracture, as the coalescence of micro fractures is not directly associated with propagation but rather with some form of collapsing mechanism, an attempt has been made to formulate an "empirical" macro shear fracture criterion, which would simulate these shear fractures relatively simply.

The stresses around a mode II fracture tip (Figure .4.1) are expressed in terms of polar co-ordinates as tangential and shear stresses (after Lawn and Wilshaw, 1975), whereby the tangential stresses ($\sigma_{\theta\theta}$) operate tangential to a circle with the crack tip as centre point and the shear stresses ($\sigma_{r\theta}$) act along the radius of that circle:

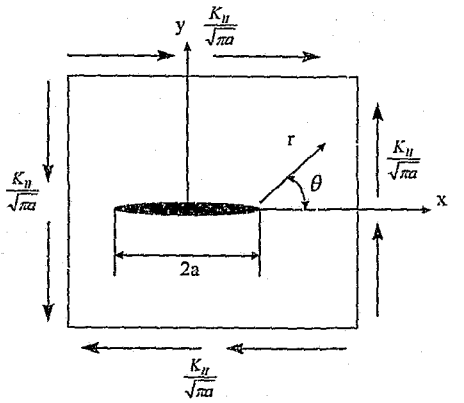

Figure 4.1 Mode II fracture conditions

$$\sigma_{\theta\theta} = \frac{K_{II}}{\sqrt{2\pi r}}\left(-3\sin\left(\frac{\theta}{2}\right)\cos^2\left(\frac{\theta}{2}\right)\right) \tag{4.3}$$

$$\sigma_{r\theta} = \frac{K_{II}}{\sqrt{2\pi r}}\left(\cos\left(\frac{\theta}{2}\right)\left(1-3\sin^2\left(\frac{\theta}{2}\right)\right)\right) \tag{4.4}$$

whereby K_{II} is the stress intensity due to an external shear loading

Both functions are graphically displayed in Figure 4.2

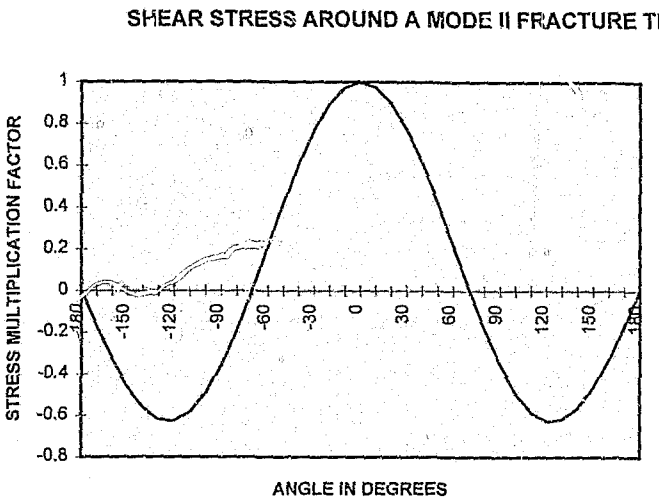

a) Shear stress distribution

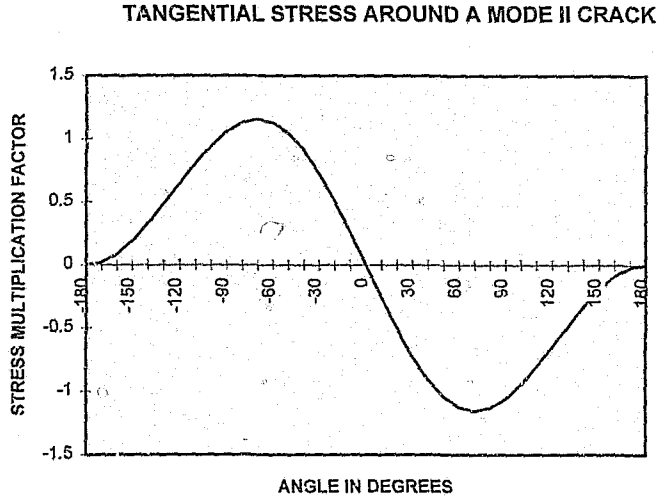

b) tangential stress distribution

Figure 4.2 Stresses around a mode II fracture tip

As the ESS criterion is expressed in similar terms, it is possible to use equations (4.3) and (4.4) in order to identify those conditions for which the ESS criterion reaches a maximum.

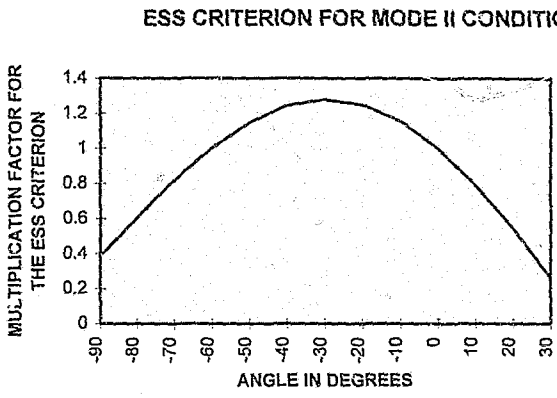

Figure 4.3 ESS criterion for pure mode II conditions. Coefficient of friction = 0.7; the angle refers to the situation in Figure 4.1

It is clear from Figure 4.3 that a maximum for the ESS criterion is reached when the fracture extension angle is approximately -30 degrees (Figure 4.1). Lower and higher frictional resistance would result in smaller (minimum 0) or larger extension angles.

Compressive tangential stresses ($\sigma_{\theta\theta}$) reduce the values of the ESS criterion while tensile stresses theoretically increase these ESS values. The contribution of tensile tangential stresses towards shear failure is rather difficult to interpret in a physical sense, but is nonetheless directly implied by the Excess Shear Stress (and the Mohr-Coulomb) criterion if non zero values for the cohesion parameter are applicable. In the DIGS application the mean stress (the average of principal stresses) is not allowed to become tensile, otherwise the ESS criterion is assumed to be invalid.

In practical applications a tension cut-off strength, which limits the potential value of the tensile tangential stresses, is implemented. Pure mode II conditions are, however, not conducive to shear failure as tangential stresses normal to the crack tip reach high tensile values under such conditions. The extreme values for the tangential stresses can be derived by differentiating expression (4.3) with respect to the angle θ. A maximum value of $\frac{1.15K_{II}}{\sqrt{2\pi r}}$ for $\theta = -70.54^{o}$ and a minimum value of $-\frac{1.15K_{II}}{\sqrt{2\pi r}}$ for $\theta = 70.54^{o}$ is thus obtained. The first condition would typically lead to the formation of a tensile (mode I) fracture as the value of the tangential stress near the fracture tip would exceed the tensile strength of the material before the shear strength is reached, especially if one assumes that the shear strength is substantially larger than the tensile strength. In this context, shear strength is defined as the resistance against failure in *shear* as a result of mode II loading, which is not necessarily the same as the resistance against fracturing as a result of mode II loading. As has been discussed previously, such fracturing is most likely due to excess *tensile* stresses and is therefore not associated with shear failure. It is therefore necessary to suppress tensile fracturing in order to enable shear fracturing to occur. By applying compressive stresses, tensile fracturing will be more effectively suppressed than shear fracturing.

A maximum for the ESS criterion in (4.2) is found for $\frac{d\sigma_{r\theta}}{d\theta} = \tan\phi \frac{d\sigma_{\theta\theta}}{d\theta}$, so that

$$\tan\phi = \tan\left(\frac{\theta}{2}\right)\left[\frac{-8}{3(1-3\cos\theta)}+1\right] \tag{4.5}$$

Inserting various values for the fracture extension angle θ in (4.5), a matching friction angle ϕ can be found. Table 4.1 shows a range of possible combinations.

Fracture extension angle (degrees)	Friction angle (degrees)
0	0
-10	11.7
-20	23.5
-30	35.6
-40	44.2

Table 4.1 Matching values for fracture extension and friction angle under mode II loading conditions

The values in table 4.1 are only applicable to situations where stress concentrations can occur; in other words the original discontinuity must have been mobilised. The theoretical fracture extension angle according to the Mohr-Coulomb criterion is $45^o - \frac{\phi}{2}$ from the direction of the major principal stress. As the principle stress is oriented at 45^0 from the original defect, it follows that the theoretical Mohr-Coulomb "shear fracture" should deviate $\frac{\phi}{2}$ degrees from the defect. It is clear from table 4.1 that fracture extensions are not representative of shear band orientations as defined by a Mohr-Coulomb criterion.

An alternative to the excess shear stress criterion is the so called energy criterion (SIMRAC report GAP029, 1996) in which it is assumed that fracture extension will take place in such a way that a maximum amount of energy is dissipated due to deformation associated with slip or opening along or across the (extended) shear fracture. The energy criterion is also expressed in terms of local shear and tangential stresses as

$$\sigma_{r\theta}^2 - (\tan^2\phi)\sigma_{\theta\theta}^2 \qquad \text{if} \sigma_{\theta\theta\leq} 0$$

and (4.6)

$$\sigma_{r\theta}^2 + \sigma_{\theta\theta}^2 \qquad \text{if } \sigma_{\theta\theta} \geq 0$$

Under pure mode II conditions, expression (4.6) results in values as shown in Figure 4.4.

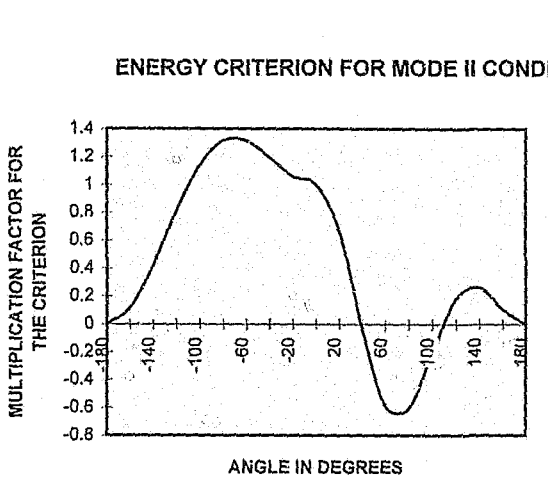

Figure 4.4 Relative value for the energy criterion around a mode II crack tip.
A value of 0.5 has been assumed for $\tan^2 \phi$.

Figure 4.4 indicates a maximum value for the energy criterion for positive tangential stress. In order to find extremes for the energy criterion the zero values of the derivative with respect to the fracture extension angle θ have to be found:

$$\frac{d\left(\sigma_{r\theta}^2 + \sigma_{\theta\theta}^2\right)}{d\theta} = 0 \qquad (\sigma_{\theta\theta} \geq 0) \tag{4.7}$$

Inserting the following equations into (4.7)

$$\frac{d\sigma_{\theta\theta}^2}{d\theta} = 2\sigma_{\theta\theta}\frac{d\sigma_{\theta\theta}}{d\theta} \tag{4.8}$$

$$\frac{d\sigma_{r\theta}^2}{d\theta} = 2\sigma_{r\theta}\frac{d\sigma_{r\theta}}{d\theta} \tag{4.9}$$

and substituting the expressions in (4.3) to (4.6) it can be found that

$$3\sin^2\left(\frac{\theta}{2}\right) = 1 \tag{4.10}$$

so that the maximum is found for a value of -70.53 degrees

If pure mode II conditions are combined with a compressive, hydrostatic stress field, the situation changes and tensile tangential stresses can either be completely or partially suppressed. Figure 4.5 shows the results for complete suppression of global tensile stresses.

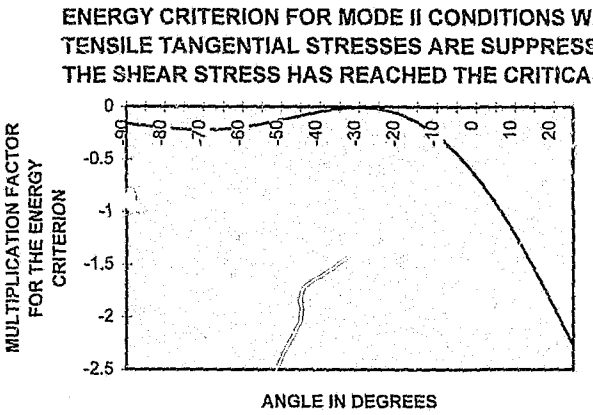

Figure 4.5 Relative values for the energy criterion when tensile tangential stresses are completely suppressed by a compressive hydrostatic stress field ($\tan^2 \phi = 0.5$) and the shear stress has reached the critical level for shear slip

It is clear from Figure 4.5 that when tangential stresses are compressive, the energy criterion reaches a peak value at approximately -30 degrees. This angle is however dependent on the magnitude of the hydrostatic stresses. The situation whereby tangential tensile stresses are completely suppressed is not realistic as fracture propagation under such conditions may not be feasible.

Error! Not a valid embedded object.

Figure 4.6 Relative values for the energy criterion when tensile tangential stresses are partially suppressed by a compressive hydrostatic stress field ($\tan^2 \phi = 0.5$)

In Figure 4.6 tensile tangential stresses occur for angles less than -15 degrees and a maximum value for the energy criterion is obtained at a fracture extension angle of around -9 degrees. The magnitude of the hydrostatic stress determines over what region the tangential stresses will be positive and they affect the location of the maximum value in a similar way as in the previous example. It is interesting to note that the Energy criterion predicts (initial) fracture extension angles which are equal or smaller than the inclination of the original flaw, while the angles predicted by the ESS criterion are consistently smaller.

The reason for this difference in predicted (initial) fracture extension angles is related to the fact that the level of hydrostatic stress affects the fracture propagation angle in the Energy criterion, while the fracture propagation angle as predicted by the ESS criterion is insensitive to the value of the hydrostatic stress. Only in the limiting case of critical shear slip (Figure 4.5), is the predicted extension of the initial fracture element equal for both the Energy and the ESS criterion. In the next section both these criteria will be used in numerical simulations and their potential for shear fracture reproduction will be investigated by allowing multiple increments to take place

4.2 SHEAR FRACTURE GROWTH FROM NUMERICAL SIMULATIONS

Results from applications of both The Excess Shear Stress and the Energy criterion have been obtained for mode II fracture simulation as discussed in the introduction. While initial conditions could be represented by relatively simple analytic solutions, this is not the case when fracture growth is involved. For this reason, results from DIGS simulations have to be used in order to investigate the suitability of both criteria further.

Figure 4.7 shows the resulting fractures according to both criteria under pure mode II loading conditions. The principal stresses are indicated in this Figure and they result from shear tractions which are applied along the boundaries of the block in which the horizontal flaw is located.

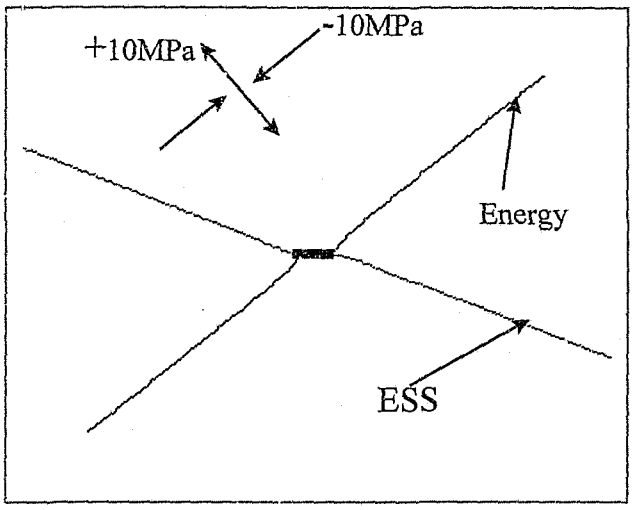

Figure 4.7 Resulting fractures for (pure) mode II conditions.

The resulting fracture from a flaw which is activated in pure mode II (shear only) resembles a tensile fracture according to the energy criterion, while the ESS criterion produces quite a different result (Figure 4.7). The result from the energy criterion is according to the condition of tensile tangential stresses around the crack tip and represents in fact an opening mode fracture. This results appears to be quite realistic, whereas the ESS criterion does not lead to an appropriate result, due its the inability to deal adequately with tensile stress conditions.

When a (moderate) amount of compressive hydrostatic pressure is added, a situation which is more conducive to shear failure is obtained. Figure 4.8 shows resulting fracture patterns for both the ESS and the Energy criterion in that particular case. In each simulation 100 fracture increments have been accommodated and these results are therefore quite representative of the further fracture development. Fracturing is initiated from a sliding flaw as in the previous example and the friction angle was assumed to be 20 degrees in this case. The principal are orientated along diagonals with respect to the horizontal and vertical axes.

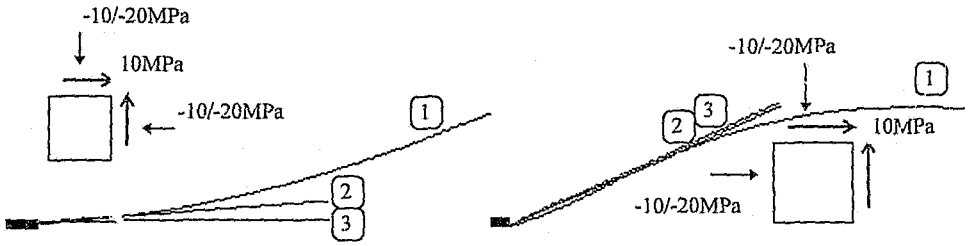

a) Energy criterion: 1 -10MPa, no dilation
2 -20MPa, no dilation
3 -20MPa, with dilation

b) ESS criterion: 1 -10MPa, no dilation
2 -20MPa, no dilation
3 -20MPa, with dilation

Figure 4.8 Fracture geometry for mode II loading conditions with varying additional hydrostatic compressive stresses for both criteria (20° friction angle)

The results in Figure 4.8 correspond better to the theoretical shear band angle derived from continuum plasticity than the results shown in Figure 4.7. The fact that none of the principal stresses is tensile obviously plays a major role in this respect. It should be noted however that none of the results matches the theoretical values correctly, although it was found that while the results from the Energy criterion were always stable, the results of the ESS criterion only showed stable behaviour in the case of the higher compressive stresses (-20MPa). In the case of the -10MPa hydrostatic stress, results were quite erratic for this criterion and this behaviour can most likely be associated with the presence of tensile mean stresses at the search radius. As has been mentioned previously, the ESS criterion cannot deal appropriately with such conditions and this situation should therefore be avoided in numerical applications. .

The stable results of the ESS criterion (case 2 and 3 in Figure 4.8b) led to a fracture path which show a "wavy" appearance; an initial fracture angle of 15° is followed by a stable increase until a maximum value of 33° is obtained, after which a stable decrease to 27° is followed by another stable increase to a final value of 30°, after the maximum number of increments has been reached. While the results of the energy criterion always appear to be stable, in the sense that the fracture path is continuous, a wavy fracture path is also associated with the presence of higher (-20MPa) compressive stresses (case 2 and 3 in Figure 4.8a); an initial fracture angle of 2.08° is followed by a stable increase until a maximum of 5.47° is reached, after which a minimum of 5.24° leads to a final value of 5.25°. It is apparent that in both cases the results tend to converge to a particular value; a relatively large angle of approximately 30° in the case of the ESS criterion and a smaller angle of just over 5° in the case of the Energy criterion.

The lower (-10MPa) compressive stresses (case 1 in Figure 4.8) resulted in an initial fracture angle of 2° which continuously increased to approximately 30° in the case of the Energy criterion after which the maximum number of 100 increments was consumed. As has been discussed in the previous section, the magnitude of the stresses around the fracture tip determine to a large extent the direction of fracture propagation. It is therefore

likely that, in the case of relatively low hydrostatic compressive stresses, fracture propagation may lead to the development of a stress field around the fracture tip which becomes increasingly tensile, resulting in a fracture path which tends to approach the direction of the major principal stress. Similar results were obtained for simulations in which a friction angle of 35° was used.

It can thus be concluded that although both the ESS and the Energy criterion can in principle represent propagating shear fractures, the ESS criterion can not adequately deal with tensile stresses around the propagating fracture tip. As the presence of tensile stresses is not directly associated with failure in a (global) compressive stress environment, such conditions may be assumed to be exceptional and therefore of minor importance. However, in the case of brittle fracturing, such an assumption can not be considered, as tensile stresses will almost certainly develop. This is also demonstrated by the numerical simulations which indicated the presence of tensile stresses even in the absence of global tensile stresses. If brittle failure is assumed to control the failure processes, it is of major importance to consider the presence of tensile stresses and the ESS criterion is thus not suitable. The Energy criterion does allow for a (smooth) transition from compressive to tensile stress conditions around the fracture tip and can therefore be used to represent brittle fracture propagation.

The use of a crack opening dilation angle may have an effect on the results. In Figure 4.8 results are shown for the case where sliding along the fracture surfaces is associated with deformations normal to the fracture surface as well. In these simulations a dilation angle of 5° has been used and the results are marked as case number 3 in Figure 4.8. While the effect is rather pronounced for the Energy criterion, the ESS criterion does not seem to be affected by dilation of the fracture. According to the theory of failure localisation as described in Section 3.2, the dilation angle may or may not have an effect on the orientation of the shear band angle, depending on the conditions at which the band is formed. However, according to this theory, if the dilation angle does influence the orientation of the shear band angle, its effect is similar to an increased friction angle, namely an orientation which becomes more aligned with the direction of the principal stresses. The opposite effect can be observed in Figure 4.8, namely an orientation which deviates more from the direction of the principal stresses. As propagating shear fractures do not form under comparable conditions as assumed in the shear band theory, it is not obvious if and how dilation should influence the orientation of shear fractures.

A fundamental difference between the Energy criterion and the ESS criterion is the influence of the hydrostatic (mean) stress level on the fracture propagation direction. It is not completely obvious how this influence affects the results in the case of multiple increments, as simulated in the numerical models, but it is clear that the results from the Energy criterion are more consistent with the formation of a shear failure plane than the results from the ESS criterion.

In a mode II experiment with FLAC, the effect of plastic deformations around a fracture tip have been investigated. Figure 4.9 shows the results of a simulation in which no plastic deformations were allowed in the continuum (Figure 4.9a) and the results of a simulation in which excessively stressed areas were allowed to deform plastically and shed load. A Mohr-Coulomb failure criterion was applied and perfect plasticity was assumed (no

hardening or softening). The parameters used were: cohesion 6MPa, angle of internal friction 30° and dilation angle 0°. It can be observed that stress rotations take place inside the failure zone and that the maximum tensile stresses become concentrated in the same failure zone. This suggests that the potential for tensile, brittle failure exists in a larger area than the direct fracture tip, due to stress redistribution. Plastic deformation may therefore have an influence on the location of subsequent brittle failure.

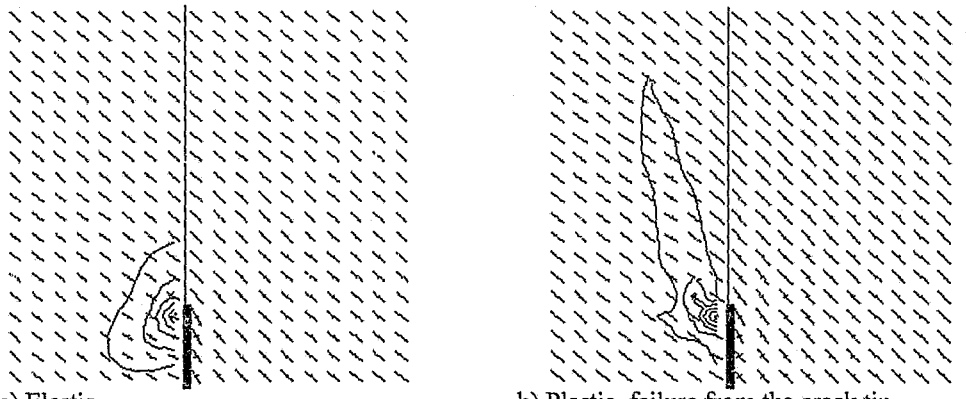

a) Elastic b) Plastic, failure from the crack tip, contours of maximum tensile stresses (equal values for both cases)

Figure 4.9 Stress distribution around a mode II fracture tip. Additional hydrostatic loading of equal magnitude to the shear loading. Crack tip is indicated (FLAC)

4.3 CONCLUSIONS

Although the processes which lead to shear fracturing and shear failure localisation may be extremely complex and not directly amenable to numerical simulation, an attempt has been made to use simplified models in order to represent these structures. The theory of plasticity is based on shear failure and describes the formation of shear bands quite well. If localisation of failure occurs before the onset of brittle failure, it can be argued that typical fracturing processes do not play a role in the location of shear fractures, which is controlled by plastic deformations in that case, as has been discussed in Chapter 3.

If brittle failure is assumed to precede the formation of a shear fracture, it appears to be logical to use the theory of fracture mechanics in order to represent the damage processes around a propagating fracture tip. As can be appreciated from Chapter 2, linear elastic fracture mechanics, in combination with a fracture criterion based on limited tangential tensile stresses, can not reproduce shear fractures. This still leaves various alternative options, of which only one has been explored in this Chapter. Linear elasticity in a continuum has been assumed in all the numerical models presented here and only the fracture criterion has been allowed to vary. The assumption of a continuum is mainly driven by a need for simplicity and is difficult to justify when a rock mass is considered at a small scale (fracture tip). The same applies to the assumption of (linear) elasticity, although alternatives can relatively easily be accommodated by current numerical models.

A numerical model (FLAC) in which plastic deformations were allowed to occur around a fracture tip which was loaded in mode II (shear), resulted in stress rotations and changes in tensile stress distribution. This could explain alternative fracture paths, which seems to suggest that a (simple) process zone model may be effective for the simulation of shear fracturing. At this stage it is not fully understood if shear fractures can be represented by individual fractures or if some form of (micro) fracture coalescence has to be incorporated. Shear fracturing currently appears to be associated with brittle failure and the processes which precede the formation of a shear fracture have not been investigated in sufficient detail. The main question in this respect is the issue of plastic deformations. If plastic deformations are required to precede the formation of a shear fracture and these plastic deformations can be represented by a continuum, then the relatively simple numerical models which have been presented can be used. If plastic deformations cannot be represented by a continuum formulation, or if plastic deformations are not relevant to this problem, alternative models have to be selected. In the next Chapter an attempt has been made to represent the discontinuous nature of a small scale rock mass.

The assumption of alternative fracture criteria is rather empirical and it has to be appreciated that no fracturing processes are directly represented by any of the criteria which have been evaluated here. The detailed physical processes taking place in the process zone are ignored and the criteria are only based on global theories of minimising shear resistance (ESS criterion) or maximising the amount of energy released, by simplified deformation processes, according to the Energy criterion. The initial shear fracture propagation direction from a flaw, loaded under mode II conditions, is not influenced by the level of hydrostatic stresses, according to the ESS criterion. The Energy criterion, however, predicts a distinct influence on the shear fracture propagation direction by the value of the hydrostatic stress. This fundamental difference may explain the different numerical results as well to a certain extent. It is, at this stage, unclear which of these two criteria is most appropriate to represent shear fracture propagation.

Although such empirical and simplified models may seem to reproduce observed fractures, it is not clear if and under which circumstances they are valid. Further research should be directed towards determining the physical occurrence of shear fractures under controlled conditions and in various materials, in order to obtain a reliable database for reference and calibration purposes. At present it is extremely difficult to analyse reported shear fractures as boundary conditions etc. are generally very poorly assessed. In cases where the global stress field is supposed to be uniform, minor (unforeseen) disturbances can affect the failure mechanism significantly. It is therefore proposed to use mode II experiments, similar to the numerical experiments shown here, in order to promote shear fracturing and suppress tensile (mode I) fracturing.

The process of shear failure has been represented in this chapter by single discontinuities which are assumed to represent shear *fractures*. In the previous chapter 3, the bifurcation theory has been used to predict and simulate the formation of shear *bands* in a continuum. It is not clear if any of these representations is realistic with respect to shear failure in brittle materials. The representation of shear failure by a single discontinuity implies that shear fracture propagation takes place, while the representation of shear failure in a continuum by plasticity theory does not necessarily lead to expansion of shear failure in the form of a shear fracture (or band). Areas which have been subjected to a homogeneous

distribution of shear failure may subsequently collapse into localised shear bands as a result of bifurcation, but this is not necessary in order to allow expansion of shear failure.

As has been argued before, brittle shear failure is the result of coalescence and interaction processes between multiple imperfections and it may be necessary to represent these imperfections in more detail in order to simulate shear fracturing in a realistic way. In the following chapter a method, which allows for the representations of imperfections in the form of randomly distributed discontinuities, is introduced and applied.

5.0 OBSERVATIONS FROM LABORATORY EXPERIMENTS IN RELATION TO FRACTURING OF ROCK

Laboratory experiments on the fracturing processes in rock which is subjected to compressive stresses are described and analysed in this section. Only experiments in which stress concentrations are artificially and purposefully introduced have been selected, because the fracture and failure processes in most other experiments will often be dominated by unknown stress concentrations from boundary effects, weaknesses in the specimen etc. The following types of experiments have been selected as being the most representative for mining applications:

- fracturing around cylindrical openings
- fracturing around slots
- experiments designed to induce shear fracturing

5.1 FRACTURING AROUND CYLINDRICAL OPENINGS IN ROCK SUBJECTED TO COMPRESSION

Stress distributions and the associated failure processes around circular openings can be considered the most important single problem in rock mechanics (Jaeger and Cook, 1979) and it is for this reason that it is included here. Failure of borehole walls: so-called borehole breakouts (petroleum industry), sidewall spalling/slabbing (mining) or even "dogearing", is a common occurrence due to the high stresses at depth and has been the subject of many studies. Other fracturing processes in the form of primary and remote fractures can also occur if confining stresses are sufficiently low.
Carter et. al. (1991) classify the observed fractures around a circular openings in a block of rock which is subjected to an increasing uniaxial load and a relatively low confining stress as follows:

1. primary tensile fractures
2. secondary or remote fractures
3. side-wall slabbing or compressional failure

The primary tension fractures form in response to tensile stress concentrations which can be predicted by elasticity theory. Failure in the area of compressive stress concentrations is typically observed around highly stressed openings. The existence of secondary or remote fractures has been demonstrated through physical model tests by Hoek (1964), Lajtai (1971), Gay (1976) and Ingraffea (1977). Their existence around mining excavations may be obscured by the fact that, as their name implies, they form some distance from the opening and do not intersect the excavation boundaries. Ingraffea and Heuze (1980) were the first to analyse the formation of remote fractures by appropriate numerical modelling and demonstrated that these fractures are effectively extension fractures which originated from areas away from the opening in which tensile stress concentrations developed due to a stress redistribution resulting from primary fracture growth. The fact that this type of fracture is not observed in artificial materials such as glass and brittle plastics is explained by the absence of critical flaws in the nucleation zone inside the specimen. Flaws in artificial materials are only present at the surface, due to the process of preparation of such materials, while natural rock contains natural flaws which are distributed throughout the

volume as envisaged by Griffith (1924). In fact, Griffith postulated that artificial materials such as glass also contain internal natural flaws, but this obviously contradicts current understanding.

A numerical simulation with DIGS clearly demonstrates the potential for remote, secondary fracture formation around a circular opening. Figure 5.1 shows the resulting fracture pattern in a uni-axial stress field. Primary fracturing takes place at the crown and the bottom of the opening, but after a limited extension of these fractures, four distinct zones of global tensile stress concentration can be observed (Figure 5.1a). Macro fracturing can be expected to be initiated within these zones from pre existing flaws. This is shown in Figure 5.1b where secondary fracturing has been allowed to take place as well from open flaws which are used as seed points. The tensile strength has been selected as 16MPa. A similar process of fracturing is described in section 5.2 in more detail.

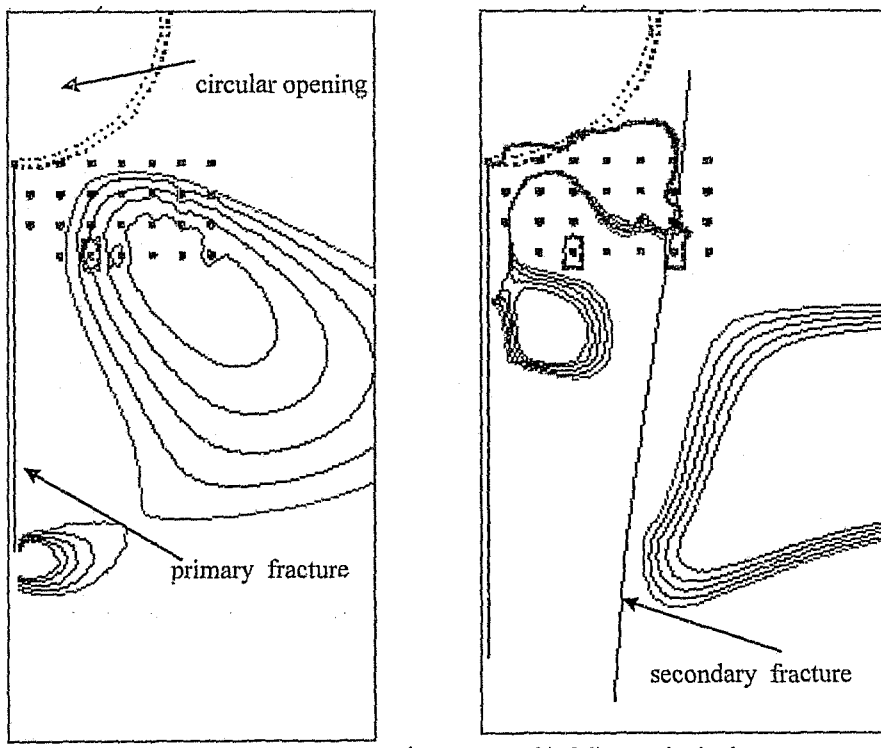

a) Minor principal stress distribution after the formation of the primary fracture; load = 14MPa

b) Minor principal stress distribution after the formation of the secondary fracture; load = 120MPa

Figure 5.1 Numerical simulation of the fracturing around a uni-axially loaded specimen containing a circular opening; contours represent values between 1MPa and 2MPa (DIGS, double symmetry)

In experiments by Carter et al (1991) a 200x200x60 mm block of (Lac du Bonnet) granite was used to obtain quantitative information on the nucleation of the primary, remote and

compressional fracture processes. Strain gauges were strategically positioned to signal the initiation of fractures after a 36mm opening was drilled in the centre of the specimen. Primary fractures formed at a uniaxial load of 16MPa which is 2MPa higher than the Brazilian tensile strength of this granite. Theoretically, assuming linear elasticity, these fractures should initiate at 14MPa. The higher load necessary to initiate the primary fracture suggests that the stress gradient effect is noticeable at this scale. The average crack propagated to a length of approximately 43mm at a load of 135MPa and extended another 4mm by the end of the test at the final load of 157MPa. The secondary or remote fractures initiated at 119MPa and propagated both towards and from the opening with increasing load.

The remote fractures are not necessarily continuous cracks but often form in a step wise fashion and can also be observed to exist parallel to other remote fractures. Figure 5.2 shows the fracturing around a circular opening of 60mm diameter in a 300x300x300mm block of Timeball Hill quartzite which was subjected to a vertical stress in excess of 200MPa and an out of plane stress of 10MPa. The U(ni-axial) C(ompressive) S(trength) of this quartzite is slightly more than the applied stress, namely approximately 250MPa. The primary, remote and compressional fractures can be observed here as well and are quite similar to the results obtained by Carter et al. In order to analyse the initiation and propagation of primary and remote fractures numerical models have been used. Figure 5.1 shows the distribution of minor principal stresses before and after the formation of a primary fracture from the borehole crown. It is clear that the location of the secondary fractures is directly controlled by the stress redistribution taking place in response to the primary fracturing.

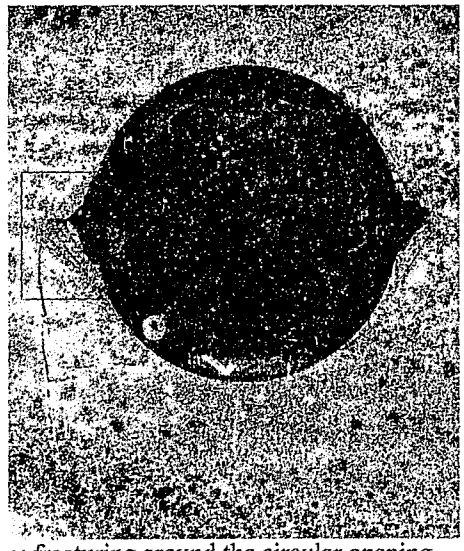

a: fracturing around the circular opening



b: detail of fracturing in the notch

Figure 5.2 Fracturing around a hole in a large specimen of Timeball Hill Quartzite

Failure in the compression zone in the form of slabbing or spalling initiated at a load of 126MPa in the granite specimens. Theoretical analysis, again assuming linear elasticity,

would predict failure in this zone to initiate at one third of the uniaxial compressive strength which would amount to approximately 75MPa for this particular granite. The steep stress gradient may again be used to explain the difference between theoretical and actual values, but Santarelli and Brown (1987) propose that a variation of Young's modulus with confining pressure is the mechanism which affects and controls the (non-linear) elastic stress distribution around openings in compressed rock.

They explain the high loading stresses, which are associated with the onset of failure in the compression zone, as being due to a stress redistribution which is controlled by an increasing elasticity modulus with increasing confining stress. As the confining stresses, which are the radial stresses in this case, increase from zero at the wall of the opening to a maximum value further inside the material, so does the stiffness increase with increasing distance from the wall of the opening. This increasing stiffness will result in a redistribution of stresses from areas of low stiffness to areas of increased stiffness. In the case of a circular opening in a compressed medium this would lead to a decrease of tangential stresses close to the boundary of the opening and an increase of tangential stresses further away from the opening. As failure is assumed to be initiated at, or at least very close to, the opening, the reduction of tangential stresses should result in a delay in the onset of failure and an apparent increase in strength as observed in the experiments which have been described here.

The effectiveness of this mechanisms obviously depends on the amount of stiffness increase with an increase in confining pressure. Some rocks appear to be more sensitive than others and data from Stravropoulou (1982) suggests that variations in stiffness of 50% for sandstone, 30% for norite and 25% for quartzite are possible. (figure 5.3) In the case of porous rock (sandstone) an explanation for this increase in stiffness can easily be found in the closure of pores during hydrostatic compression which makes the rock material more compact and thus stiffer. In the case of crystalline rocks (norite and quartzite) the explanation must also be sought in the microstructure, although the details are most likely more complex.

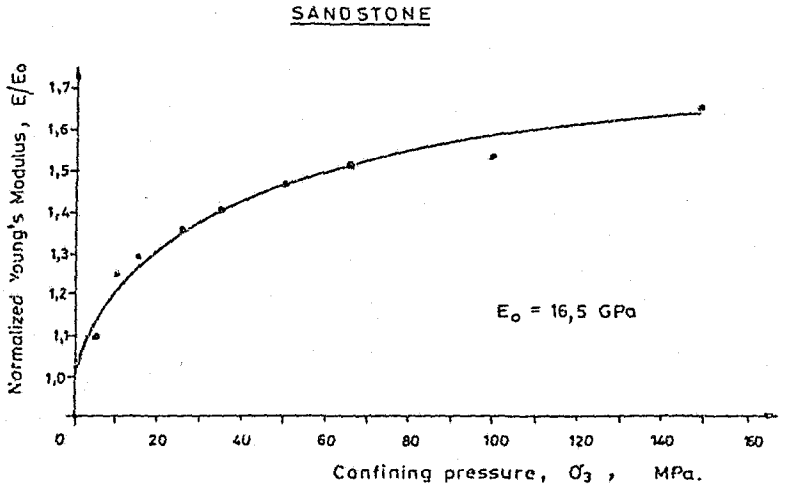

a) Relation between confining pressure and the Elasticity Modulus of sandstone

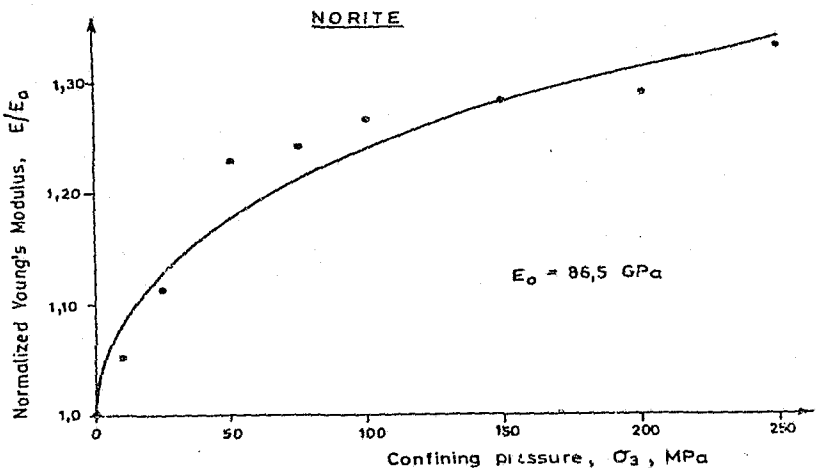

b) Relation between confining pressure and the Elasticity Modulus of norite

Figure 5.3 Effect of confinement on the stiffness of various rocks (after Stavropoulou, 1982)

The sensitivity of Young's modulus to confining pressure has also been observed for Lac du Bonnet granite and is described by Martin (1993). Martin associates the variation of elastic stiffness with damage due to microfracturing of the rock upon retrieval from its natural environment. He found that the Young's moduli of rock samples which were retrieved from relatively shallow depths were less sensitive to confining pressures than rock samples which were removed from greater depths. Although the evidence for non linear elastic behaviour appears to be quite convincing, it is not often considered as a potential mechanism in mining applications.

The focus of attention has been mainly on the fracture processes in the compression zone. Lee and Haimson (1993) studied borehole breakouts in specimens of Lac du Bonnet granite subjected to a constant confining stress and an increasing principal stress and observed an initial formation of subparallel transcrystalline micro cracks near the borehole wall. The density of these micro cracks decreases with increasing distance from the borehole wall and thin layers of rock flakes, subparallel to the tangential stress direction are formed in this way. After the principal stress has been increased sufficiently, these micro cracks continue to grow, coalesce into wider fractures, or branch into multiple cracks forming a complex network of discontinuities. The first spall is then created by the separation of a rock flake between the borehole wall and the nearest crack due to buckling in the middle or shearing off at the ends of the flake. A stress redistribution around the new free surface of the hole leads to the separation of the next flake in a similar fashion and the process repeats itself until the breakout stabilises into a deep and pointed notch, also referred to as a "dog-eared".

Very similar behaviour was observed in a underground circular tunnel in the same rock (Martin, 1993). The only difference was a 300% lower strength of the in situ tunnel compared to the laboratory experiment. This difference in strength can be attributed to scale effects, but alternative explanations are given by Martin (1993) and Martin et. al. (1996). They suggest stress corrosion, creep, humidity and even stress rotations as possible mechanisms contributing to an effective decrease in strength.

Ewy and Cook (1990) tested thick walled, hollow cylinders of Berea sandstone and Indiana Limestone, which were subjected to axi-symmetric pressures on the inner and outer diameters and constrained to plane strain (no axial deformation allowed). They also describe non-linear, recoverable, elastic deformations before the onset of failure at locations of low compressive strength in the tangential direction. Although they also observed an increase of overall stiffness with higher pressures, they suggest an alternative model to that of Santarelli and Brown (1987), as some of their observations could not be reproduced by this model. They propose a model which would account for the dependence of moduli on the 3-D stress state and stress path. In analysing various models which might capture the observed pressure dependant stiffness they note that the maximum tangential stress may not necessarily occur at the borehole wall, but could be located further inside the rock.

This possibility has also been suggested by Santarelli and Brown (1989) and Maury (1987) and has been used to explain failure initiation at a certain distance away from the borehole surface rather than at the borehole surface (Figure 5.4). Although this may be a possible explanation, such a behaviour does not appear to be observed in actual breakouts The observations are however not detailed enough to allow a conclusive judgement and the precise origin of the failure processes is yet unknown. Another problem with respect to this explanation is the effect of the minor (and intermediate) principal stresses on failure initiation. This effect of confining stresses has been completely ignored in the pressure dependent elastic model as shown in Figure 5.4. Although it is known that the confining stress has a considerable effect on rock strength, the model only takes the magnitude of the tangential stress into account.

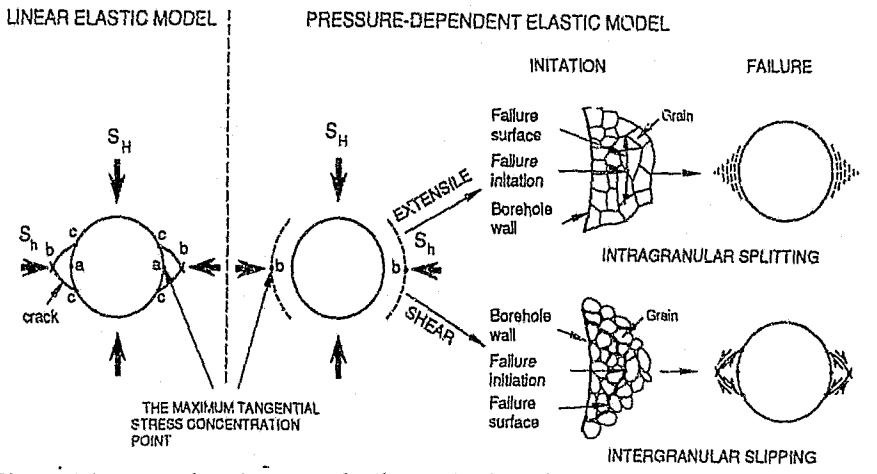

Figure 5.4 Comparison between the linear elastic and pressure dependent elastic model (after Maury, 1987)

Ewy and Cook (1990) also refer to results of Haimson and Herrick (1989) for different size holes in Alabama limestone, which suggests that a size effect alone can account for the apparent strengthening. Many more similar tests are, however, required in order to obtain any conclusive evidence for this scale effect. With respect to the actual fracturing processes, they also observe an initiation of small spitting cracks close to the opening in an area with the highest stress/strength ratio. As these cracks open and thus cause a certain area of the rock to dilate, the stress field around such an area will be affected. Such a zone of dilating fractures could "....promote the formation of a macroscopic en echelon feature intersecting the surface..."(Ewy and Cook, 1990). At a critical stress these en echelon fractures, which intersect the surface, are formed. As these en echelon fractures allow stress relieving deformations, due to the fact that they are inclined with respect to major principal stress direction and allow for shear displacement, further cracking is likely to occur in response to the stress redistribution associated with the development of these en echelon fractures.

Coalescence of small splitting cracks into macroscopic splitting fractures, which join the en echelon fractures, allow fragments of rock to detach. This process repeats itself until a stable breakout zone is obtained. Zheng et. al. (1989) simulated the formation of a such breakout zone with a numerical model which only considers the elastic stress distribution around progressively spalling holes and obtained very realistic results by successively removing over stressed areas around the simulated opening. Their model predicts triangular breakout zones with pointed tips

The size of the detached fragments of rock is associated with the spacing of the macroscopic fractures. One explanation for this spacing has already been discussed, namely the initiation of failure away from the borehole surface due to a pressure sensitive stiffness of the rock; this explanation appeared to be inadequate however. Another explanation is that the fracture spacing is related to some internal length of the material, such as the grain size. This approach has been applied to the formation of splitting

fractures around holes within the framework of bifurcation analysis (Papanastasiou and Vardoulakis, 1989).

Ewy and Cook suggest that the volume of rock to be detached must be of some finite volume if sufficient strain energy is to be made available for the formation of the fractures which allow it to detach. In this respect it is interesting to note that the slab thickness around underground tunnels is larger than the thickness observed in (small scale) laboratory experiments. This seems to indicate that the microscopic structure does not affect the spacing of the macroscopic fractures, but that some larger scale mechanism controls this parameter. When the holes are supported by an internal support pressure the splitting fractures are suppressed in their growth and the macroscopic splitting fractures *do not* form. With increasing load however larger and larger areas will be subject to the nucleation of micro fractures and finally micro crack interaction appears to result in the formation of localised shear bands. These shear bands are assumed to initiate near the hole wall and to progress deeper into the rock with increasing stress. Most of these shear fractures or bands seem to stabilise at some distance into the rock. A few of these shear fractures are able to intersect corresponding shear fractures and thus allow the detachment of some rock from the surface of the opening.

Haimsong and Song (1993) describe the borehole breakout of a rock in which the formation of macroscopic splitting fractures was not observed. The Cordova Cream limestone used in these tests consists of grains which are stronger than the (cementing) matrix in which they are embedded. This is unlike the granite where the entire mass is occupied by randomly distributed bonded crystals of similar material properties. They also observed pronounced non-linear behaviour between the applied load and the tangential strain recorded at the borehole wall long before any acoustic signals or other evidence of failure initiation could be detected. Haimsong and Song (1993) compare this observation to observations by Santerelli and Brown (1989) and suggest that pressure dependant elastic behaviour can explain this strain non-linearity.

However, the strain non-linearity which they observed in the Cordova Cream limestone is different from the one described by Santerelli and Brown in the sense that the tangential strain deviates from linearity in exactly the opposite direction. Instead of indicating a stiffness *reduction* at the borehole wall, the measurements suggest an *increase* in stiffness. This is not in agreement with the pressure dependant stiffness model proposed by Santarelli and Brown and therefore this behaviour cannot be explained with that model. The first fractures to be noticed were intergranular cracks which initiated at the surface of the borehole wall. These cracks advanced into the rock with increasing load. Behind the borehole wall, these extending cracks occasionally turned into extensile fractures sub-parallel to the borehole wall. With further loading conjugate cracks, which are inclined with respect to the major principal stress direction, intersect and effectively create a breakout. Contrary to the other rocks which have been discussed previously, no multiple splitting fractures and associated coalescence took place, but individual intergranular fractures appear to initiate from the borehole wall and grow into the rock. This process can be associated with the initiation and propagation of a shear fracture and is apparently controlled by the microstructure of the rock.

Santarelli and Brown (1989) also observed macroscopic splitting fractures in a Gebdykes dolomite resulting in the formation of thin (0.25mm) slabs parallel to the surface of the opening, but they noticed a different failure development in a Doddington sandstone where neither such slabs nor the localised shear fractures as seen in the Cordova Cream limestone could be observed. Instead, macroscopic failure appeared to be diffuse because micro crack propagation was inhibited by the micro structure of the rock. This particular rock consists of strong quartz grains in a weak matrix where the volume of grains almost completely makes up the volume of rock. The propagation of inter granular cracks is believed to be inhibited because the number of blocking grain boundaries is bound to be high in this case. Failure in uniaxial tests of this sandstone also showed the development of a large number of loosely clustered micro cracks leading to complete damage of parts of the specimens rather than failure along discrete surfaces as observed in most other rocks. Santerelli and Brown (1989) found a very strong parallel between rock behaviour in triaxial compression and that in hollow cylinder tests for both the Gebdykes dolomite and Doddington sandstone.

Observations from an underground tunnel in massive homogeneous Lac du Bonnet granite (Martin, 1993) revealed that the initial failure can be described as "crushing" near the centre of the potential breakout zone. The next stage in the failure process is the splitting of thin slabs parallel to the tunnel wall and on either side of the crushed region. This process repeats itself until the notch reaches some stable depth. Figure 5.2 also shows evidence of such a sequence. The horizontal fractures which can be observed on both sides of the opening in this figure most likely formed during unloading, but are most likely associated with "crush" zones which developed during loading. If it is assumed that the crushing process is associated with an effective plastic behaviour due to non localised micro mechanical fracturing and damage processes, then the formation of the macroscopic splitting fractures can be explained as a secondary process in response to the stress redistribution resulting from the initial, primary crushing process. The driving force for the macroscopic splitting fractures can be identified as induced tensile stresses by this crushing zone.

This process has been simulated with DIGS in a rather simplistic way by representing the crushing zone as a horizontal slot and results are shown in Figure 5.5. Discrete macroscopic fractures are generated because tensile stresses are induced below and above this horizontal slot. These tensile stresses allow fractures to propagate directly from the slot and also at other locations where high tensile stresses are induced. Seed points have been selected at locations with the highest stresses. Although fracture initiation is still assumed to be caused by stress concentrations on a microscopic scale, the propagation of the fracture can be analysed on a larger scale, because it is believed that the availability of a global tensile stress will dominate any micro mechanical influences.

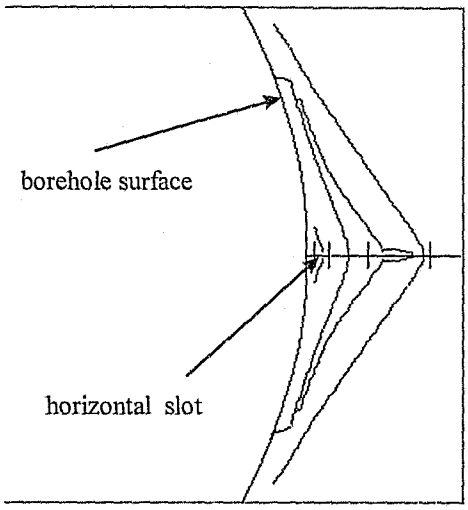

Figure 5.5 Simulated (tensile) fracture pattern due to the presence of a horizontal "crushing" zone in the sidewall of a circular opening. (DIGS, uni-axial loading in vertical direction)

Discrete fracturing and failure localisation in the presence of tensile stresses takes place on a macroscopic scale, which appears to be in contrast with many of the formerly described laboratory observations, in which the microstructure was believed to control the fracturing and shear localisation processes. A possible explanation for these contradictory observations may be found in the size of the models being analysed in relation to the grain size of the rock. It can be argued that, if the ratio between model size and grain size is relatively small, the microstructure of the rock will dominate the fracturing and failure processes, whereas with this ratio being relatively larger, the failure processes which take place at the micro level can be considered as resulting in homogeneous failure in relation to the macro fracturing processes which are taking place due to global stress influences.

Although micro fracturing processes are often assumed to control the macro fracturing as well, it has never been demonstrated how, under conditions of confinement, macroscopic extension fractures can develop by a mere "coalescence" process of micro fracturing. Also, if a more realistic three dimensional flaw model is considered, it becomes even more difficult to envisage the formation of macroscopic splitting fractures in the absence of global tensile stresses. It seems, therefore, more realistic to investigate the possibility that such global tensile stresses may in fact be *present*.

5.2 FRACTURING AROUND RECTANGULAR OPENINGS IN ROCK SUBJECTED TO COMPRESSION

Although all potential failure and fracture mechanisms can in principle be observed around cylindrical openings, a rectangular opening is more closely related to a long-wall mining stope and the fractures which are induced around such a slot may resemble the fractures which are generated around typical deep long-wall stope faces. Gay (1976) found that the fracturing which he observed around slots in uni- and bi-axially loaded sandstone and

quartzite specimens followed similar patterns of development in all the experiments. The first cracks to form were tensile fractures initiating in the centre of the hanging- and foot-walls. Simultaneously with, or shortly after the formation of these cracks, spalling or slabbing of the rock at the abutments of the slot started. With increasing stress, this zone of fractured rock extends further into the rock, both in the horizontal and in the vertical direction. An increase in stress is achieved in these experiments by maintaining a constant vertical load and by increasing the span of the opening in increments.

The third phase of fracture development appears at higher stresses and thus larger spans in the form of large cracks which propagate out of the zone of spalling. (Figure 5.6) These cracks mainly aligned themselves with the direction of expected principal stresses, but on occasion fractures which were inclined with respect to this direction could also be observed in the sandstone specimens. Such fractures are typically associated with shear deformations across them and may relate to shear fractures which have been observed around underground stopes. Gay does however note that these shear fractures or shear zones are often influenced by the boundary conditions, although he also observed shear fractures which did not appear to be influenced by boundary conditions. The formation of the shear fractures could only be observed when the length of the slot reached a certain value, which is explained by Gay as being related to higher induced stress levels at the ends of the slots. Such an explanation is however not completely satisfactory, as the stress distribution around a slot surrounded by a damaged zone can differ substantially from an elastic stress distribution. The fact that larger openings can more easily interact with the boundaries is another factor which could influence the formation of the shear fractures.

Summarising, it is not clear if observed shear fractures can be entirely associated with the effect of the slot, because boundary conditions may have influenced the fracturing processes to a large extent in the described experiments. The extension fractures, which align themselves with the principal stress direction, can be explained from the presence of tensile stresses. Fracture initiation is typically assumed to take place at a flaw, where locally very high tensile stresses can be induced. Fracture propagation can subsequently take place if global tensile stresses perpendicular to the fracture path are present.

The results of these laboratory experiments produce fractures which may have some resemblance to the fracture pattern around deep level longwall stopes. The differences between the laboratory specimens and a typical mining excavation are however numerous. The most obvious ones are the smaller scale and the absence of geological features in the laboratory tests. The bi-axial loading conditions are also unrealistic as the presence of on out of plane stress is not included in the laboratory tests. The excavation process, which includes blasting cycles, is obviously also not represented in these experiments. Nevertheless, these experiments have been used to test the capability of the numerical models and to gain additional insight in fundamental rock fracturing processes.

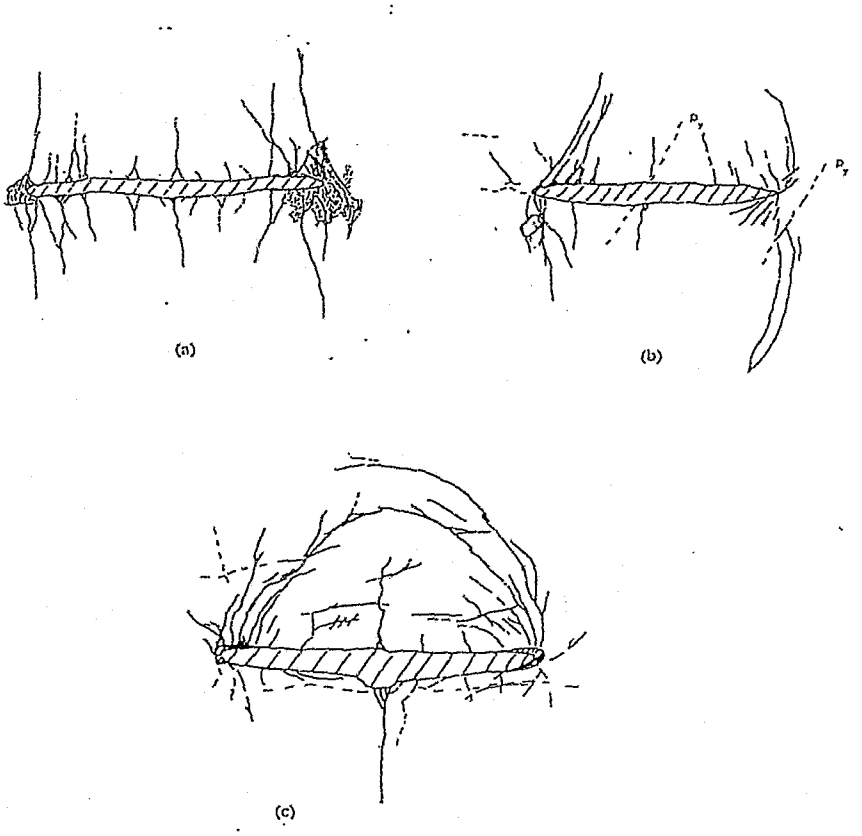

Figure 5.6 Fractures induced in sandstone specimens due to bi-axial loading (after Gay, 1976)
a) uni-axial loading (surface of specimen)
b) ratio between horizontal and vertical load ~ 0.2 (surface of specimen)
c) ratio between horizontal and vertical load ~ 0.5 (surface of specimen)

In Figures 5.7 to 5.9 the results from numerical simulations with DIGS are shown. The fractures which have been simulated here are opening mode (mode I) fractures which fail according to a critical tangential tensile stress at their tip. Only a single mining step has been analysed in these numerical models. Primary fractures initiate from the centre of both hanging- and foot-wall and propagate vertically into the rockmass. After increased loading, secondary fractures initiate from locations inside the rockmass and also from other positions along the hanging- and foot-wall. The so-called remote fractures inside the rockmass initiate from seeds which have been placed at locations where the highest tensile stresses occurred. Seeds could unfortunately not be placed randomly, as the interaction between propagating fractures and seeds often leads to numerical problems. The results presented here have therefore been obtained by a process in which the stress distribution after the formation of the primary fracture had to be analysed first. From this stress distribution locations of potential fracture initiation had to be selected for the placement of seeds.

From these results it can be observed that the secondary fracture orientation is sensitive to the ratio between applied horizontal and vertical stresses (K-ratio), similar to the observed experimental results. Most of the laboratory experiments were conducted under uniaxial conditions, while those which were subjected to bi-axial stress conditions only experienced maximum effective K-ratio's of approximately 0.4. As typical K-ratio's in deep South African gold mines range between 0.5 and 1.0, the resulting fracture patterns may not be directly representative for fracturing around longwall stopes although the fracture mechanism may be comparable. Unfortunately, the maximum confining pressure which could be applied to the specimens was limited to 40MPa, and fracturing could only be initiated at relatively high vertical pressures and associated small K-ratio's.

Ozbay (1987) conducted similar experiments with multiple slots separated by small areas of solid rock (pillars). He observed similar fracturing as in the single slot experiments with most of the large scale fractures resembling tensile fracturing while some large scale fractures seem to be associated with shear fractures. Boundary effects can however also not be excluded in this case. An interesting phenomenon in the last experiments is the presence of fractures splitting the specimen perpendicular to the out of plane direction. No confinement was applied in this direction and fractures appear to initiate from the pillar edges. It is not known if similar fractures occurred in Gay's experiments, but the formation of such fractures can at least be expected to limit the stresses which can be applied to the specimen and thereby reduce the potential for the formation of shear fractures.

Experiments in which realistic poly-axial stress conditions can be reproduced would therefore be more desirable, but results from such experiments were not available at the time of writing this thesis.

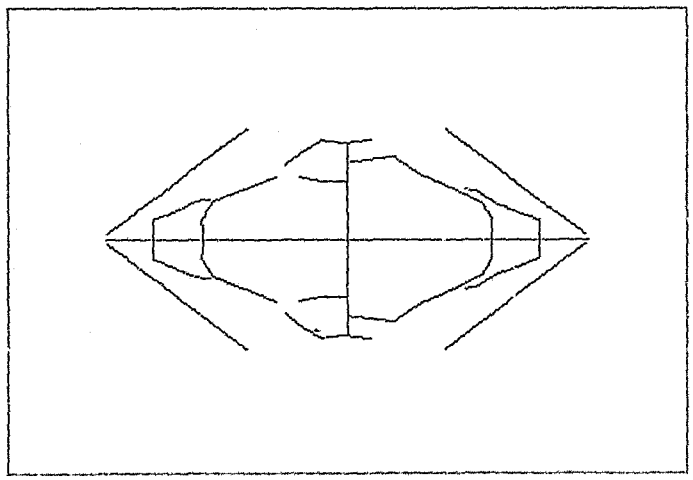

Figure 5.7 Tensile fracturing around a horizontal slot. Ratio of horizontal versus vertical stress = 0.4 (numerical simulation with DIGS)

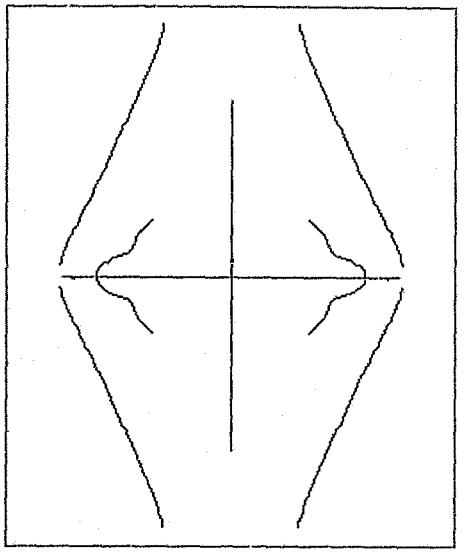

Figure 5.8 Tensile fracturing around a horizontal slot. Ratio of horizontal versus vertical stress = 0.0 (numerical simulation with DIGS)

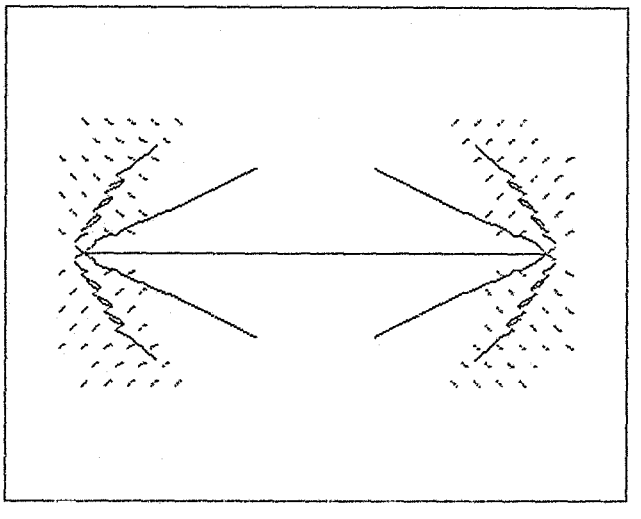

Figure 5.9 Tensile fracturing around a horizontal slot from seeds which are represented by stress raisers (pores). Ratio between horizontal and vertical stress = 0.4 (numerical simulation with DIGS)

In Figure 5.9 additional flaws have been introduced in the model. These flaws have been distributed regularly in areas of high failure potential. From these flaws (micro) fractures were also allowed to initiate and grow incrementally. When Figure 5.9 is compared with Figure 5.7, where the fracture initiation is not assumed to be associated with local stress concentrations, it is clear that micro mechanical processes may influence the formation of macro fractures. The en echelon fractures in Figure 5.9 for instance are steeper than the corresponding fractures shown in Figure 5.7.

While the model shown in Figure 5.9 is an attempt to represent micro mechanical processes, it is obvious that the representation of the micro structure of rock requires a more rigorous treatment. By constructing a random assembly of dislocations the micro-structure of granular materials such as rock or concrete may be represented (Napier and Pierce, 1995). After the generation of random geometric centres in a region which covers the area of interest, a mesh is created by the formation of polygons around the random centres. This technique is also used in the following numerical models in an attempt to consider the micro structure of the rock. Two types of polygons are available in the current DIGS programme, namely hexagonal and triangular polygons.

The choice of polygon has a major influence on the fracture formation (Napier and Pierce, 1995). Propagation of fractures is more easily accommodated by the sharp, triangular elements than by the more rounded hexagonal polygons. This results in a more brittle response of the models in which triangular elements have been used and it is for this reason that most of the following models apply the triangular elements. The sides of each of each of the polygons is represented by a displacement discontinuity which can be activated by excess stresses. Any criterion for activation could in principle be selected, but in the current application a failure criterion which is based on the Mohr-Coulomb criterion is used.

By the choice of parameters it is possible to allow for tensile failure only (high cohesive strength combined with a relatively low tension cut-off), or to allow for shear failure only (no friction and unlimited tensile strength), or any combination between those two failure modes. Pre and post failure properties can be selected to represent hardening, softening and perfect plastic behaviour. In this way a large variety of possible models is available, allowing the user a wide choice in failure criteria, parameters and micro structure. Post failure behaviour in DIGS does not allow for *strain* hardening or softening behaviour as the post failure properties are immediately assigned as soon as a critical strength is reached. Subsequent deformations do not influence the associated parameters.

The main reason for the application of these so-called tessellation models in the following simulations is their potential for the analysis of the effects of shear failure in combination with the ability to reproduce tensile fracturing. The effect of strength parameters and the choice of the mesh on the resulting fracture geometry is analysed with those models.

The simulations, which are shown in Figures 5.10-5.17, show first and foremost that shear failure takes place in a non localised way, in the sense that discontinuities which have been mobilised in shear appear to fill an area of high stress concentrations, rather than to concentrate in a discrete failure plane. Only discontinuities which have been mobilised in tension appear to be able to reproduce large scale fractures

This result, which is derived from both the softening and the non softening models, suggests that (initial shear) damage is uniformly distributed. These results also imply that the formation of discrete shear fractures cannot be associated with the propagation of a failure zone or plane, but has to be controlled by another mechanism, which is most likely similar to the shear localisation process in cohesionless, granular materials. This mechanism can however not be reproduced directly with this numerical model, but is more effectively represented by a non elastic continuum model (which does not suffer from

numerical problems such as grid dependence etc.!). Although shear localisation is not represented in the results from these tessellation models, the effect of the uniformly distributed shear failure is captured and manifests itself in the induction of additional tensile fractures. These additional tensile fractures are obviously due to the stress redistribution associated with the shear failure. Similar results may be expected from models which represent the pre-failure (micro) damage by reducing the stiffness modulus (damage models). No attempt has been made however to reproduce such models here.

Figure 5.10 shows the underlying tessellation scheme of potential fracture locations. This mesh is constructed from triangular so-called Delaunay elements, which promote a more brittle behaviour than a more rounded mesh such as the honeycombed so-called Voronoi mesh (Napier and Pierce, 1995). In all the models in this section a quarter symmetry has been simulated and friction and dilation angle have been set at 30 and 0 degrees respectively. An in situ stress field of 60MPa vertical and 40MPa horizontal stress has been imposed (K-ratio 0.67) except if stated otherwise. Fractures which are shown in black have opened and fractures which are shown in grey have slipped, but not opened. The thickness of the lines representing the activated discontinuities indicate the relative magnitude of the slip or opening.

The relevant properties which have been used for the failure and residual strength in the models are listed underneath the corresponding figures. Activation of discontinuities takes place incrementally in such a way that only the most favourable element is allowed to activate at each increment.

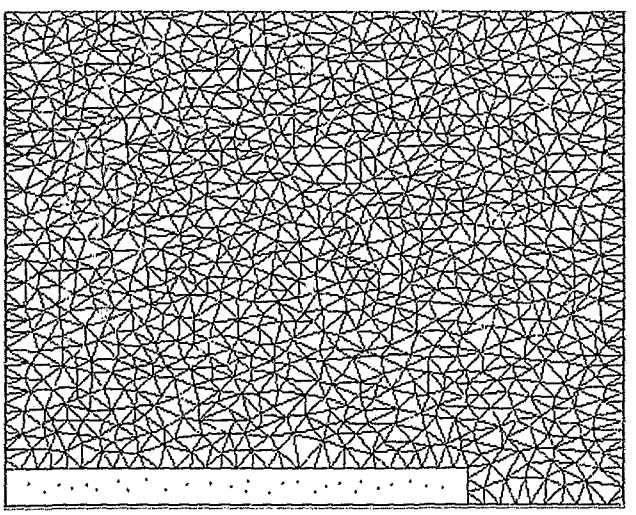

Figure 5.10 Tessellation scheme of potential fracture locations used in the following numerical simulations of fracturing around slots in a compressive stress field

The results of the simulations from the model in Figure 5.10 are shown in Figures 5.11 to 5.17. The most remarkable aspect of these results is that shear failure takes place in a non localised way, in the sense that discontinuities which mobilised in shear, appear to fill an area of high stress concentrations, rather than to concentrate in a discrete failure plane.

This result, which is derived from both the softening (Figures 5.12,5.13 and 5.17) and the non softening (Figures 5.12 and 5.13) models, suggests that shear damage expands homogeneously from a location of high stress concentration. This results also implies that the formation of large scale shear fractures cannot be associated with the propagation of a failure zone or plane, but has to be controlled by another mechanism. As has been discussed in Chapter 3 and 4, such a mechanism is most likely associated with a shear localisation process as opposed to a shear propagation mechanism. The reproduction of large scale shear localisation, which results from the gradual concentration of shear deformation into narrow zones or bands, may involve post failure mechanisms such as large strains, internal rotations, *strain* softening, etc. Such mechanisms are, at present, not explicitly catered for by the model.

Although large scale shear localisation is not represented in the results from these tessellation models, the effect of the uniformly distributed shear failure is captured and manifests itself in the induction of additional tensile fractures. These additional tensile fractures are obviously due to the stress redistribution associated with the shear failure. Similar results may be expected from models which represent the pre-failure (micro) damage by reducing the stiffness modulus (damage models). No attempt has been made however to reproduce such models here.

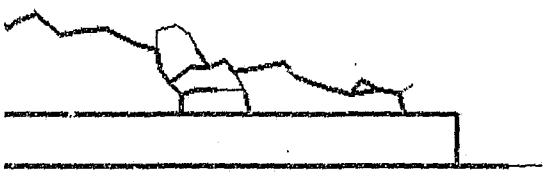

Figure 5.11 Tensile failure; cohesion before failure=900MPa (practically infinite); cohesion after failure = 0MPa; tensile strength = 1MPa

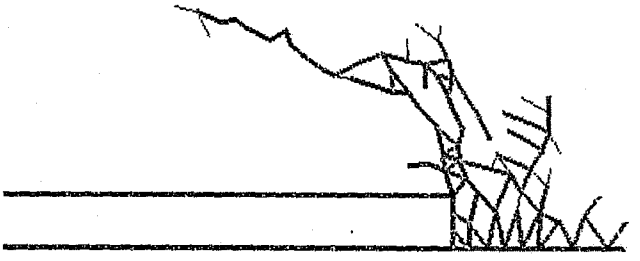

Figure 5.12 Cohesion softening with high tensile strength; cohesion before failure = 20MPa; cohesion after failure = 0MPa; tensile strength = 20MPa

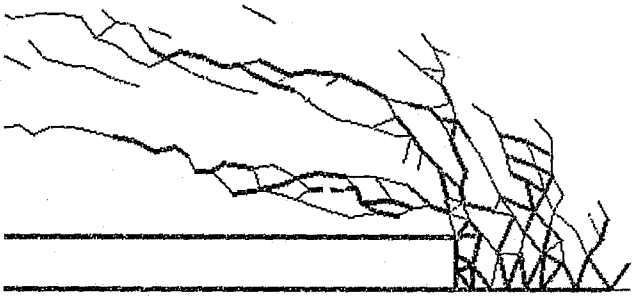

Figure 5.13 Cohesion softening with low tensile strength; cohesion before failure = 20MPa; cohesion after failure 0MPa; tensile strength = 1MPa

Figure 5.12 and 5.13 demonstrate the effect of homogeneous shear deformation on the formation of discrete tensile fractures. This non localised distribution of shear failure appears to be a natural form of shear damage expansion from a location of high failure potential such as the abutments in this case.

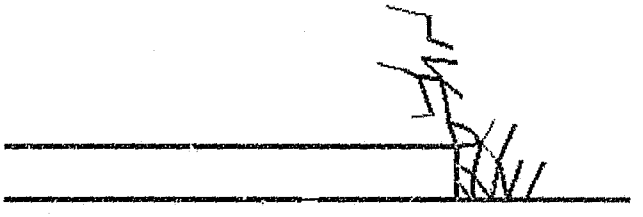

Figure 5.14 Perfectly plastic with high tensile strength; cohesion before failure = 20Mpa; cohesion after failure = 20MPa; tensile strength = 20MPa

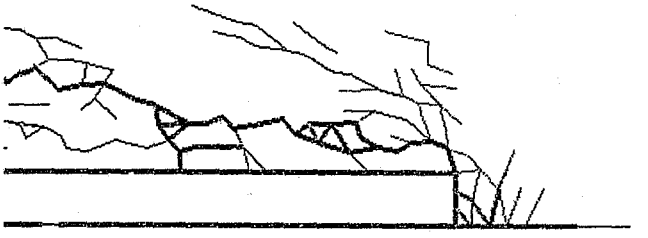

Figure 5.15 Perfectly plastic with low tensile strength; cohesion before failure = 20MPa; cohesion after failure = 20MPa; tensile strength = 1MPa

Figures 5.14 and 5.15 show similar effects as Figures 5.12 and 5.13 with respect to the distribution and expansion of shear failure and its influence on subsequent tensile fracturing. The effects are, however, less pronounced in the latter cases due to the limited amount of shear deformation which is associated with non softening behaviour.

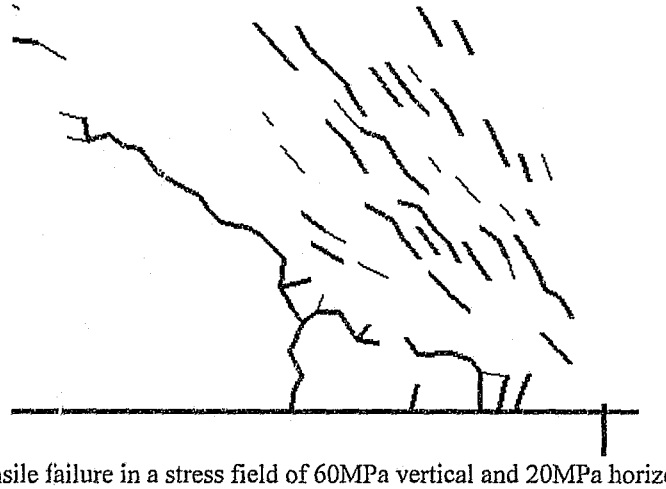

Figure 5.16 Tensile failure in a stress field of 60MPa vertical and 20MPa horizontal stress (K=0.33)

Figure 5.16 demonstrates the effect of the stress ratio on the fracture distribution in a similar way as Figures 5.7 to 5.9. Only tensile failure was allowed in this particular case, which can directly be compared with the result shown in Figure 5.11, where a stress ratio of K =0.5 was assumed. It is interesting to note that the formation of tensile fractures is associated with the initiation and growth of numerous relatively small fractures in the case of the lower confinement (Figure 5.16), whereas the larger confinement (Figure 5.11) only leads to the formation of a few large fractures. It may be that the potential for secondary fracture growth, from locations removed from the opening, is larger in the case relatively low horizontal stresses.

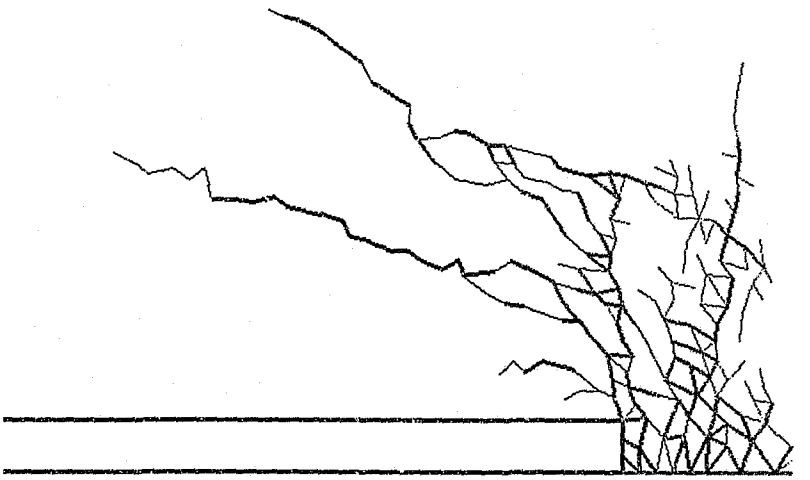

Figure 5.17 Cohesion softening with high tensile strength and a double slot length; cohesion before failure = 20MPa; after failure = 0MPa; tensile strength = 20MPa

Figure 5.17 compares directly with Figure 5.12 in the sense that the same strength parameters have been used. The only difference is the increased span of the opening, and thus the induced stresses around it, in the latter case. The result shown in Figure 5.17 also appears to indicate that shear failure expands in a more or less uniformly distributed fashion while tensile failure can be observed in the form of relatively large fractures above the opening and also in the form of smaller fractures inside the area of shear failure. A similar result was in fact also obtained from a model with half the span and a lower tensile strength of 1MPa (Figure 5.13).

In order to investigate the influence of the matrix geometry, an additional numerical model, in which the tessellation matrix was generated from a regular distribution of points, instead of random distribution, has been constructed (Figure 5.18). The results of this model are shown in Figure 5.19 and it can be seen that the regular mesh influences the fracture geometry to a large extent. In the brittle, strain softening case, a vertical fracture is generated, which cuts through the entire mesh. While it can be argued that such a regular mesh is not realistic and that this result should thus be disregarded, this simulation demonstrates to what a large extent results be affected by the choice of the mesh. The question of whether a random mesh of any arbitrary shape would be a more realistic choice remains therefore very much an open one. It could be argued for instance that a realistic representation requires some form of organised structure which is not necessarily obtained with a random mesh.

The perfectly plastic model leads to a result which can easily be related to a yielding zone and the mesh dependency appears to be limited in this case. It can therefore be expected that strain softening would in general lead to results which are dependent on the detailed structure of the mesh, whereas decreasing softening, or brittleness, would result in a less sensitive behaviour.

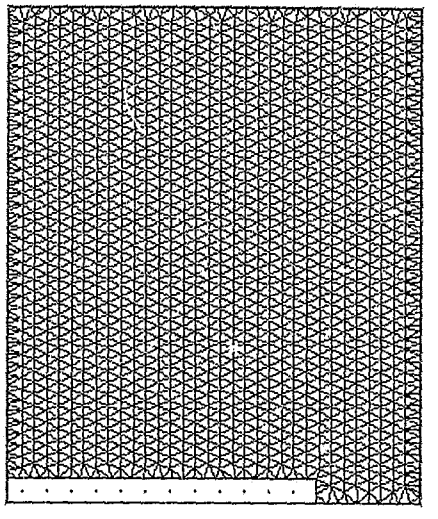

Figure 5.18 Regular mesh of Delauney triangles selected for the simulations shown in Figure 5.19

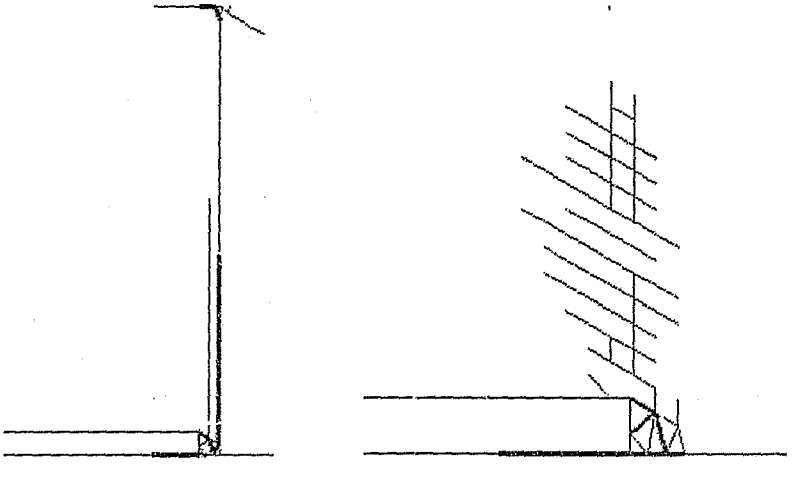

Cohesion softening (from 20MPa to 0) Perfectly plastic: cohesion = 20MPa

Figure 5.19 Results from the regular Delaunay mesh; tensile strength = 20MPa

As the regular mesh leads to a fracture geometry which can be substantially different from the random Delaunay mesh, it was decided to investigate the effect of a different mesh type as well. For this purpose an assembly of discontinuities, corresponding to regular hexagonal polygons, was used and is shown in Figure 5.20

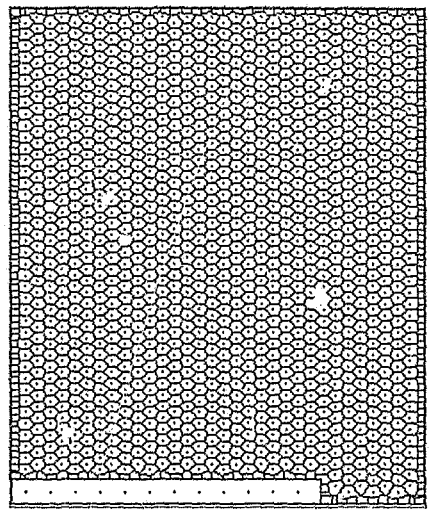

Figure 5.20 Regular hexagonal mesh used in the following simulations

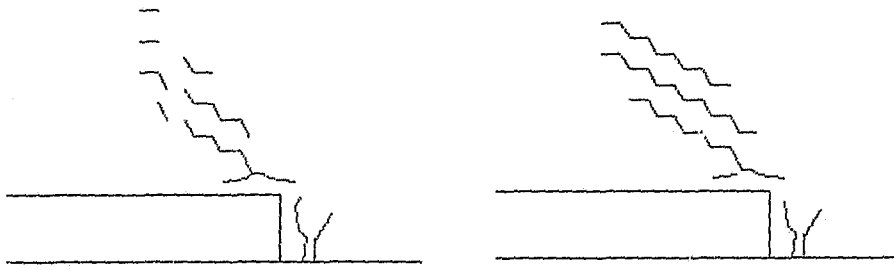

Cohesion softening (from 20MPa to 0) Perfectly plastic, cohesion = 20MPa

Figure 5.21 Results from a regular hexagonal mesh; tensile strength = 20MPa

Figure 5.21 is again noticeably different from Figure 5.19, in which a regular triangular mesh has been used, and Figures 5.14 and 5.17, in which a random triangular mesh has been used. The difference between the softening model and the plastic model is very small in the case of the hexagonal mesh. However, in the case of the softening model, failure does not occur along a continuous path, but discontinuities, which are not connected to previously activated discontinuities, are mobilised. This form of damage expansion is obviously very inefficient in terms of stress relaxation and failure remains limited to a small area around the edge of the opening. In order to allow for additional failure, a similar model, in which the material strength has been reduced, has been investigated as well. The resulting fracture pattern of this model is depicted in Figure 5.22

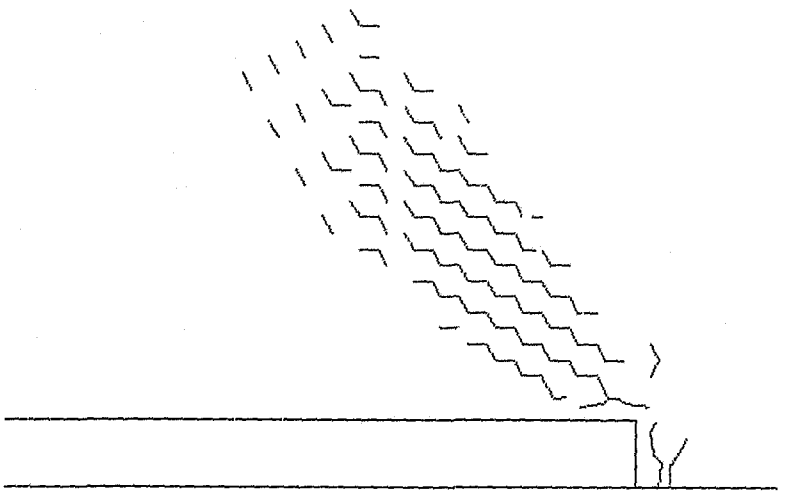

Figure 5.22 Results from a regular hexagonal mesh with reduced strength
(Cohesion before failure =5MPa; after failure = 0; tensile strength = 20MPa)

Figure 5.22 demonstrates how failure development takes place in a regular hexagonal mesh when the material strength has been reduced substantially. As has been argued before, (shear) failure does not appear to result in global softening in this mesh type as the fracture paths are staggered and discontinuous. Deformations along the sheared discontinuities are very limited as large scale deformations are restricted. Some form of failure localisation can be observed, but it is unclear to what extent the grid alignment affects these results. The activated discontinuities are more or less aligned with the orientation of the principal stresses and would therefore be associated with extension fractures rather than with shear fractures. This conclusion, which is based on the global orientation of the fractures, ignores the fact these fractures do not open. Tensile fracturing is thus not reproduced and the shear failure localisation does not appear to be realistic.

What is demonstrated clearly by the previous simulations, is the effect of the selected mesh on the resulting fracture pattern. A mesh in which planar and continuous failure paths are available (regular triangles) can result in the formation of (unrealistic?) fractures along such paths, especially if material softening is allowed. A random triangular mesh reduces the possibility of smooth and continuous failure paths and the observed shear fractures appear to be more uniformly distributed, both in the case of plastic post failure behaviour and softening, brittle post failure behaviour. A regular hexagonal mesh appears to inhibit smooth and continuous failure paths and shear failure does therefore not occur in an efficient way. The difference between a plastic and a softening, brittle post failure response is hardly noticeable, but failure localisation does take place in a way that appears to be strongly affected by the mesh orientation. While mesh dependency points to a strong influence of the detailed micro structure of a particular material, it is not clear if any of these tessellation schemes offer a realistic representation of any micro structure. A very important fact in this respect is also the two dimensional, plane strain, geometry which is used in the numerical models. Three dimensional models may lead to different results with

the use of similar tessellation schemes. Further research is required to investigate the effect of realistic micro structure representation in a three dimensional model.

In the following example large scale flaws have been introduced in order to represent geological structures. For this particular case bedding planes have been selected. It is expected that these natural flaws will influence the large scale stress distribution to a large extent and in such a way control fracture formation. The effects of geological structures on the formation of fractures is similar to the effect of a zone of shear failure in the sense that the limited resistance against shear deformation causes a redistribution of stresses in both cases.

Figure 5.23 shows the effect of bedding planes on the fracture geometry. The friction angle across the bedding planes is 30 degrees and no cohesion is assumed. The tensile strength of the rock material is set to 5MPa. Fracturing is initiated from the top surface of the hangingwall beams near the abutment due to bending of these beams towards the opening This deformation mechanism is associated with the limited shear resistance along the bedding planes and a similar pattern can be expected in a bedded footwall (numerical simulations are based on symmetry). Fractures initiating from the bottom surface of the beams can also be observed above the opening. These fractures can be associated with increased tensile stresses at the lower surface of the beams in response to the fracturing induced near the abutments as mentioned previously. This scenario can easily be explained from simple beam theory by comparing the stress distribution in a beam which is not allowed to rotate at its ends (clamped) with the stress distribution in a beam which is allowed to rotate at its ends. The former case relates to the situation before fracturing has occurred, while the latter can be associated with the post-fracture situation. Only a single mining step is simulated in this example which demonstrates how the presence of bedding planes leads to the formation of relatively steep fractures near the abutment.

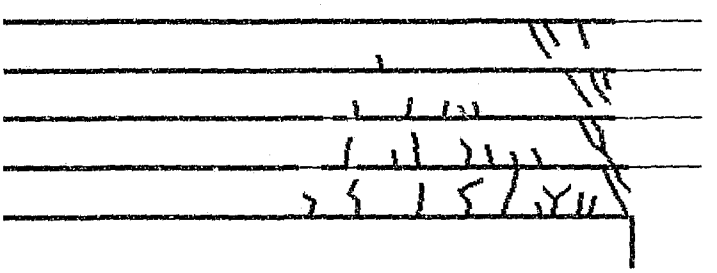

Figure 5.23 Fracture pattern due to the presence of bedding planes parallel to a stope. (quarter symmetry, K-ratio=0.67)

5.3 EXPERIMENTS DESIGNED TO INDUCE SHEAR FRACTURING

5.3.1 INTRODUCTION

It is clear from the previous section that it remains questionable whether shear fractures, which can be associated with the influence of a single opening only, have been reproduced in any of the described laboratory experiments. This issue is an important one, as the formation of shear fractures is generally associated with violent energy release (rockbursts)

and may significantly affect the stability around mining excavations. In typical triaxial and even uniaxial tests, shear fractures can often be observed. The mechanism of formation is associated with an initial uniform distribution of micro fracturing, after which some micro fracture coalescence process leads to the formation of a localised shear plane. This process can be described by localisation theory (Vermeer and De Borst, 1984) and is associated with the contraction of a damaged zone into a localised shear band. This typically occurs in approximately uniformly stressed specimens in which stress/strain gradients are negligible and micro fracturing can spread uniformly.

This mechanism is unlikely to occur in specimens where steep stress/strain gradients can be expected, because damage cannot be uniformly distributed in such a case. The failure processes have to be concentrated in local areas of excessive stresses and localised failure must take place in the form of propagating fractures. Failure takes place in the process zones of these fractures and the propagation direction may be influenced by such a process zone. Mode I (opening mode) and mode II (shear mode) fractures which fail according to a tensile criterion have repeatedly been demonstrated to exist; however the existence of mode II fractures which supposedly fail according to some other failure criterion has not been proven beyond any reasonable doubt.

According to Melin (1986), high confining stresses promote mode II growth in shear, while materials such as rock are more susceptible to this type of fracture growth than materials such as metals. Although he states that "traces of mode II growth are often detected at or after earth-quake slipping", he also mentions that the pre-existence of a fault segment in a favourable direction for mode II growth is assumed in such a case and states that experimental data on mode II failures are rare and difficult to obtain. Both statements are unsatisfactory; the existence of pre-existing discontinuities should *not* be a prerequisite for mode II failure and it is of course experimental data which could shed some light on the subject. This section therefore focuses on experiments which are designed to reproduce mode II shear fractures in homogeneous brittle materials

5.3.2 FRACTURING AROUND INCLINED SLOTS IN BIAXIALLY LOADED SPECIMENS

Petit and Barquins (1988) analysed the resulting fracture patterns around inclined slots in bi-axially loaded specimens of PMMA (polymethyl methacrylate) and sandstone. The experiments were designed to induce mode II loading conditions at the slot tips. Although tensile fractures in the form of wingcracks also occurred, shearing 'structures' could be induced from the slot tips under sufficient confinement, while branch or wing cracks were increasingly suppressed by increasing confinement (figures 5.24-5.25).

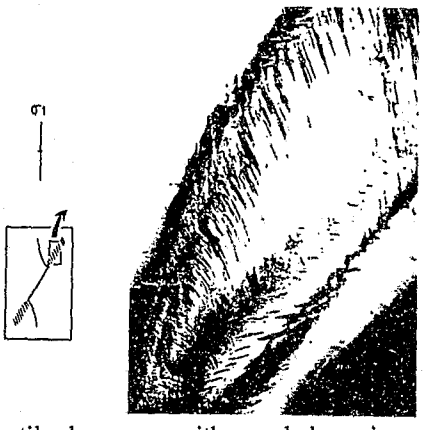

Figure 5.24 Ductile shear zone with en echelon micro cracks developed in PMMA under uni-axial loading. Horizontal cracks appeared during unloading. (after Petit and Barquins, 1988)

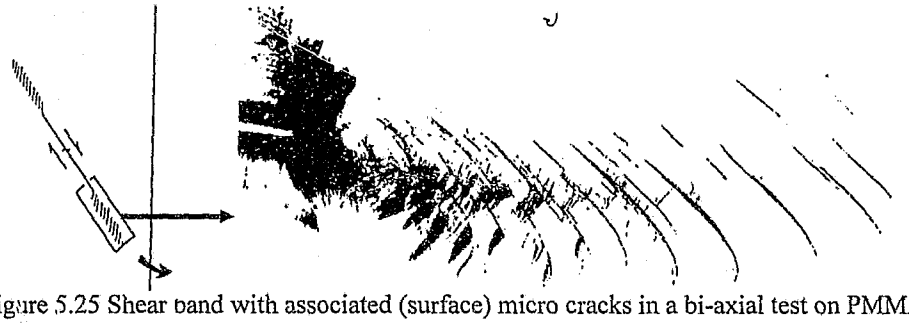

Figure 5.25 Shear band with associated (surface) micro cracks in a bi-axial test on PMMA (after Petit and Barquins, 1988)

Petit and Barquins found that a shear structure is not the mere prolongation of the defect (slot) by a single coplanar fracture, but is a macroscopic phenomenon involving opening mode I micro fractures. Such micro fractures initiate from defects such a grain boundaries and pores in the sandstone, while in the PMMA such defects behave like dislocations. The flaws are mobilised by stress concentrations at the slot tips resulting in inter- and intra-granular fractures in the sandstone while plastic deformations take place in the PMMA. The subsequent strain softening which follows the cataclasis (general mobility of defects on a grain scale) in the sandstone leads to the propagation of a shear zone from the defect. In PMMA such brittle behaviour could not be detected, although en echelon micro fractures which marked the presence of a shear zone, could be generated by application of alcohol to the surface of the PMMA specimens. The alcohol acts on surface defects to nucleate tensile fractures, which develop in response to the local stress field. The observed distribution of micro fractures in the shear zone is due to the relaxation of tensile stresses which were induced by the elasto-plastic deformation inside that shear zone; the elongated shape of the shear zone indicated how plastic deformations are controlled by the defect.

In their conclusions Petit and Barquins (1988) identify two conditions for mode II propagation, namely the presence of sufficient confinement to inhibit large scale mode I fracturing and a very dense population of defects which are orders of magnitude smaller

than the pre-existing major defect. They refer to pre-fractured rock and especially to layered sedimentary ones as satisfying this last condition and also indicate the influence of joints on the initiation of mode II shear zones. They also suggested quantification of other physical factors such as relevant rock properties by systematic experiments, but unfortunately these suggestions did not result in such experiments. Their observations and suggestions are in fact similar to the modelling results from the previous section 5.2, in which uniformly distributed (micro) damage was found to cause stress redistribution and subsequent (tensile) fracturing. Both cases indicate that localisation of shear failure in brittle materials must be preceded by a homogeneous damage process, while the formation of tensile fracturing can be influenced by such a process.

In related laboratory experiments on marble plates, Chen et. al. (1992) found that two types of fractures could be identified, namely primary fractures in the form of wing cracks and secondary fractures which manifest themselves in the marble in two ways: in the case of a single notch, vertically inclined fractures appear to propagate from the slot ends (Figure 5.26a), while in the case of closely spaced slots the direction of the secondary fractures could be influenced by the surrounding slots in such a way as to allow the formation of coalescing cracks (Figure 5.26b). An additional failure process was also observed in the experiments on the marble plates. Chen et. al. (1992) describe this process as the occurrence of an "X" shaped micro crack band from the end of the slots which propagated to cause the failure of the specimen. Such a process could most likely be interpreted as the formation of a shear band and be treated as such (Figure 5.26a).

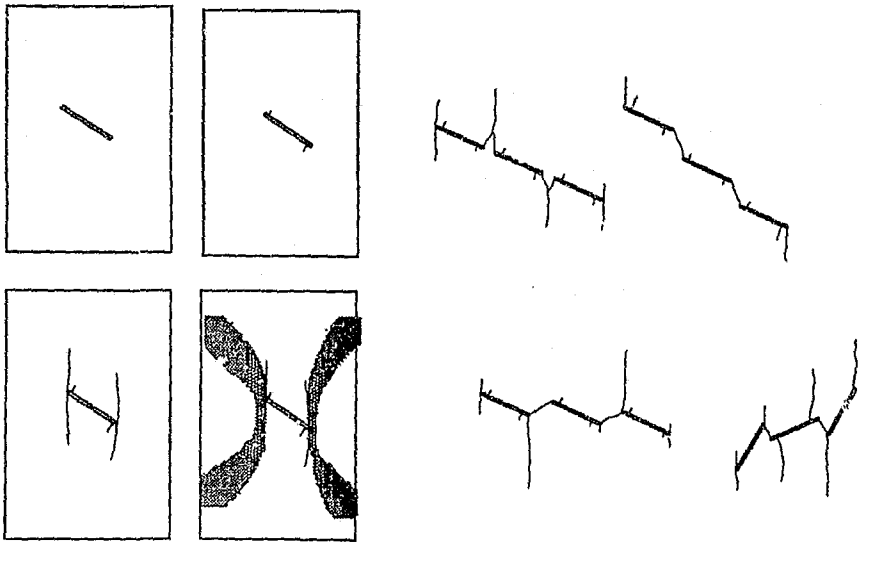

a) Fracture development around a single inclined slot

b) Fracture development and coalescence with multiple slots

Figure 5.26 Results from uni-axial tests on marble plates (after Chen et. al., 1992)

Similar experiments by Shen (1995) on gypsum specimens resulted in the formation of relatively large primary fractures, but secondary fracturing could only be seen in the form of coalescing cracks between two neighbouring slots (figure 5.27).

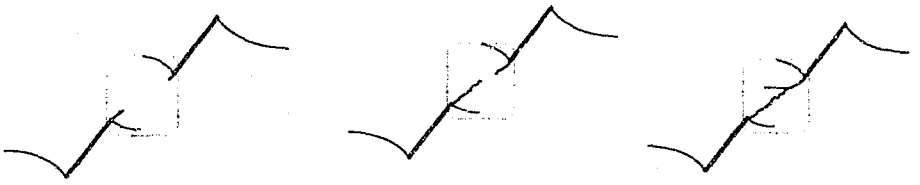

Figure 5.27 Progressive formation of primary and secondary fractures around inclined slots in gypsum plates subjected to horizontal loading (after Shen, 1995)

The formation of the primary and secondary fractures around the individual slots can be related directly to brittle fracture processes. The initiation of the primary wing cracks can be explained by analysing the stress concentrations around the slot and applying fracture mechanics theory, while the initiation of the vertically inclined secondary fractures can be explained from an analysis of the stress concentrations around the slot after the formation of the wing cracks (Figure 5.28) in the same way as has been done for the analysis of circular openings in section 5.1. Figure 5.28 shows four potential fracture initiation locations of tensile stress concentration.

In order for these locations to compete with the stress concentrations around the primary wing fracture tips, the wing fractures have to reach a length which is substantially larger than is observed in the marble specimens. The stress concentrations around the tips of relatively short wing cracks are substantially higher, which would not be favourable for the initiation of secondary fracturing. The fact that secondary fractures do initiate and propagate, while the wing fractures are still relatively short, indicates the presence of flaws, or alternative stress raisers. The effect of such stress raisers can be accounted for by selecting a lower tensile strength for fracture initiation than for fracture propagation. This is a simplified way to represent the influence of potential flaws and other stress concentrators without explicitly simulating them. In Figure 5.28 the resulting fracture pattern is shown after fractures have been allowed to initiate and grow from the potential initiation sites. Figure 5.28 compares relatively well with the observed fracture pattern around a single opening in marble (Figure 5.25) and the simulation of this type of secondary fracture seems to be quite representative.

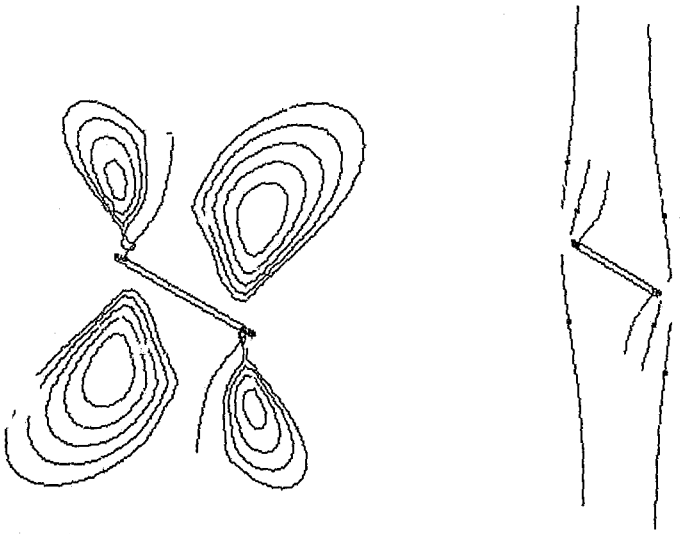

a) Minor principal stress distribution before the onset of secondary fracturing

b) secondary fracturing

Figure 5.28 Simulated fracture pattern around an inclined slot in a uni-axial stress field

The formation of the coalescing fractures which link adjacent openings in both the marble and gypsum experiments warrants a different explanation which will be attempted by additional numerical simulations. The formation of shear bands in both the experiments on marble specimens by Chen et. al. (1992) and on the sandstone and perspex specimens by Petit and Barquins (1988) are also analysed in the following numerical experiments. Numerical simulations of these laboratory experiments have been carried out with the use of continuum models which allowed for plasticity and brittle failure (FLAC) and discrete fracture models in which a structure of pre-existing weaknesses is assumed to represent the micro structure of the rock material (DIGS, tessellation scheme). The last approach allows for a general failure criterion in which a failure envelope is specified which determines whether certain pre-existing weaknesses are subjected to excessive stresses or not. Both shear and tensile failure conditions can be accommodated simultaneously. Post failure behaviour can be prescribed in all models by the specification of values for parameters relating to residual strength and the associated deformation (strain-hardening or -softening).

Four simulations with FLAC are presented. One of the parameters which has been addressed here is the change of cohesion in relation to the post failure strain. This change of cohesion effectively results in *strain* softening if the cohesion decreases after failure or alternatively in *strain* hardening if the cohesion increases with increasing strain after failure. In the DIGS simulations no *strain* hardening or softening has been represented as the post failure values for the cohesion are independent of deformations. In fact only two values are assigned to the failure parameters in DIGS, namely the one associated with the

failure strength and the one associated with the residual strength. Cohesion softening is thus independent of inelastic strain in the DIGS models.

In the FLAC simulations, the post failure values for the cohesion are related to the accumulated plastic strain. In this way a wide variation of strain softening and hardening models can be represented. The rate of softening can be expected to control the post failure behaviour to a large extent. Rapid softening will lead to a more violent load shedding than more moderate softening rates. Results will thus depend on the particular relation between plastic strain and the assigned cohesion values as is demonstrated by following results.

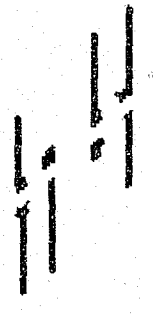

Figure 5.29 Uni-axial load (FLAC)
Tensile failure
cohesion 10MPa
tensile strength 0.5MPa
angle of internal friction 35°



Figure 5.30 Uni-axial load (FLAC);
Perfectly plastic;
cohesion 1MPa
tensile strength very high
angle of internal friction 30°

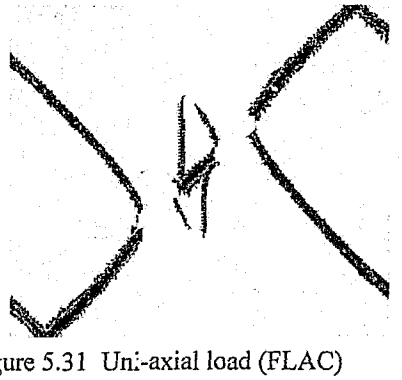

Figure 5.31 Uni-axial load (FLAC)
Gradual softening
cohesion before failure 1MPa
@0.1% strain: 0.5MPa
@0.5% strain: 0.1MPa
@1.0% strain: 0MPa

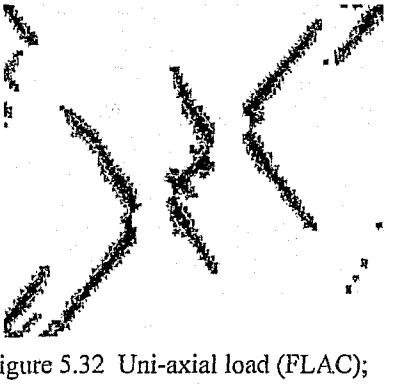

Figure 5.32 Uni-axial load (FLAC);
Rapid softening
cohesion before failure 1MPa
@0.001% strain 1MPa
@0.005% strain 0MPa

The FLAC simulations show the development of failure zones around two neighbouring slots in a uni-axially loaded medium. Figure 5.29 shows the development of tensile failure

zones on *both* sides of the slots. It is not clear to what extent plastic (shear) failure preceded the initiation of tensile failure, but this result resembles to a certain extent the observed fractures shown in Figure 5.25. This result has to be considered with some care however, as it is clear that grid alignment has taken place in Figure 5.29. Figure 5.30 shows the development of yielding zones around the two slots; no tensile failure takes place and it can be observed how large scale localisation is obtained from local yield zones which expand and coalesce with each other and the boundaries.

Cohesion softening is simulated by using two different *strain* softening rates; Figure 5.31 shows the damaged regions for a model in which slow softening takes place, while in Figure 5.32 the results from a relatively rapid softening model are shown. Both models do not appear to suffer from mesh dependency and these results may therefore be considered to be representative. Figure 5.31 shows a relatively large damaged area (grey colouring), while the damage in Figure 5.32 is more concentrated in a narrow zone. The mechanism of failure propagation is however similar to the one which controls the perfectly plastic model, namely a gradual expansion of a yield zone from the slot. The area in between the slots does not seem to attract failure and damage in preference to the other edges of the slots. This is in contradiction with the observed fracture patterns where coalescence between adjacent slots did take place while shear failure at the outer edges could not be observed. A potential explanation could be that the relation between the tensile strength and the shear strength (cohesion) is critical to this behaviour. While shear failure is promoted in the area between the slots, tensile failure is more likely to occur at the outer edges of both slots. This can also be observed in Figure 5.29. No attempt has been made however to analyse this relation between shear and tensile strength.

The plastic model, as well as the softening models, show the formation of a gradually expanding yield zone. It is not clear from the laboratory models if failure took place in a controlled fashion or not, but the results from these numerical models suggest that shear failure can propagate in a localised area, even if brittle behaviour is taken into account. Although mesh dependency has to be avoided in FLAC simulations, as grid alignment can easily occur when brittle failure is represented, no such problems were encountered with the simulations shown in Figures 5.31 and 5.32.

While these results demonstrate a potential for shear fracture simulation, it is certainly not obvious that realistic fracture patterns are reproduced. One of the most fundamental assumptions in the FLAC representation is that the material is assumed to behave as a continuum. In a different approach, using DIGS, it is assumed that the micro structure of the material plays a dominating role in the failure process. By using this approach a particular mesh is generated in which multiple fractures can be activated. The method has also been used in section 5.2 to simulate fracturing around a horizontal slot.

The Mohr-Coulomb criterion is used within a tessellation scheme (Napier and Pierce, 1995), in which potential fracture paths are restricted to a chosen mesh of discontinuities. The advantage of this approach is the fact that fracture intersections are not affected by numerical constraints. It is also possible to allow for shear failure along discontinuities and in this way effective plastic behaviour may be simulated. As the results may be sensitive to the selected tessellation (Figure 5.33 and Figure 5.34), no variation with respect to the

geometry of the mesh has been analysed in each series of models, in which only the effects of strength parameters has been investigated.

In the following simulations a mesh of so called Delaunay triangles has been used. The results in Figures 5.35-5.44 have been obtained from a random mesh which is shown in Figure 5.33, while the results of Figure 5.45 and 5.46 have been obtained from the regular mesh which is shown in Figure 5.34. In all simulations only the most favourable discontinuity is activated at each increment until no excess stresses are available to activate any of the discontinuities. Loading of the models is done through controlled displacement of both vertical boundaries in horizontal direction. Confinement is applied in the form of vertical stresses applied to the horizontal boundaries.

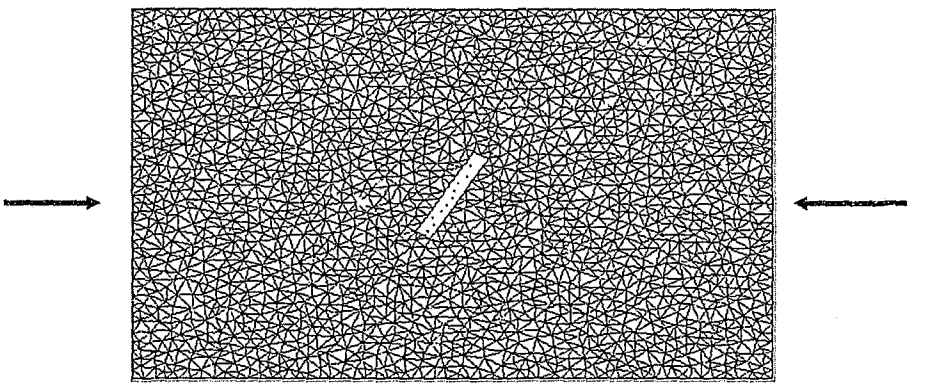

Figure 5.33 Random mesh of Delaunay triangles used in simulations 5.34 to 5.45; loading is in a horizontal direction

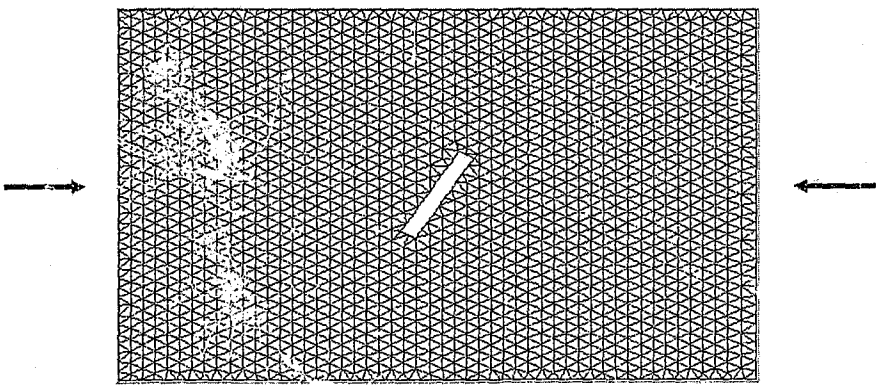

Figure 5.34 Regular mesh of Delaunay triangles used in simulations 5.46 and 5.47

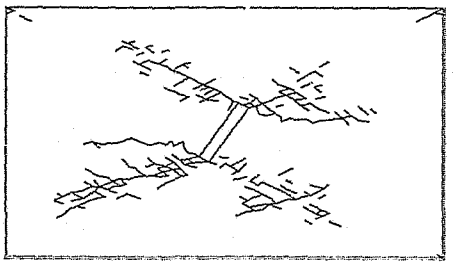

a) unconfined.

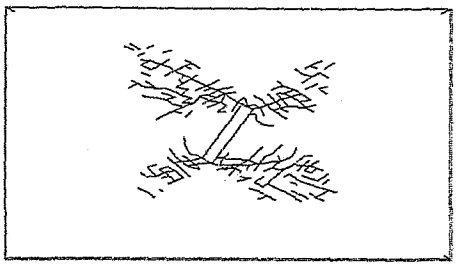

b) confined by a vertical stress of 10MPa

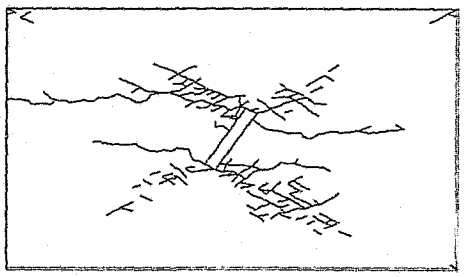

c) unconfined, tensile strength reduced to 10MPa

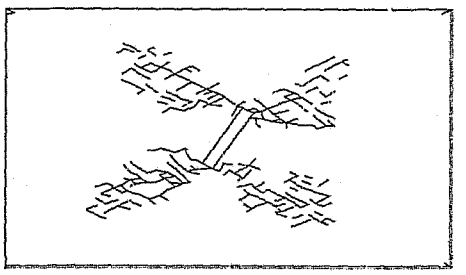

d) unconfined, dilation angle = 30degrees

Figure 5.35 Perfectly plastic; Cohesion = 20MPa, friction angle = 30 degrees; tensile strength = 20MPa

Figure 5.35 demonstrates how confinement suppresses the development of tensile fracturing (typical extended wing cracks) and how shear failure extends in a almost homogeneous, uniform fashion. The effect of dilatation (Figure 5.35d) is not very pronounced, but it appears that tensile failure is also inhibited due to dilatation. This mechanism may be similar to the one which operates in the confined situation (Figure 5.35b). The effect of tensile strength on the development of the brittle, tensile fractures can also be noticed as a reduction in tensile strength leads to in increase in tensile fracture length (Figures 5.35a and 5.35c).

The potential for tensile failure, in the case where shear failure is not allowed to occur, is demonstrated in Figure 5.36. Both uni-axial and bi-axial loading conditions have been simulated.

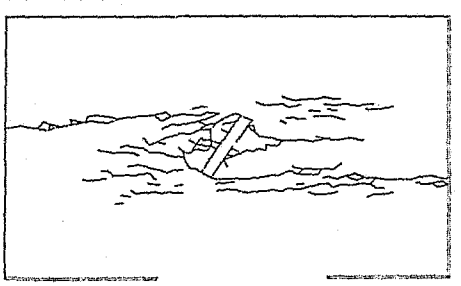

a) unconfir

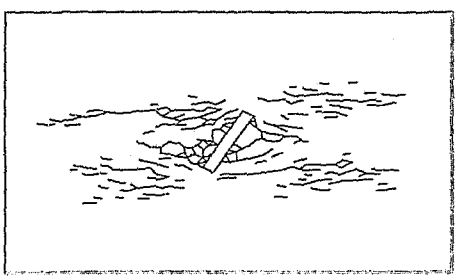

b) Confined by a vertical stress of 10MPa

Figure 5.36 Te .ohesion = 900MPa; tensile strength = 20MPa

The potential for pure tensile failure around on opening in a compressed specimen can be appreciated from the results shown in Figure 5.36. Even in the case of bi-axial compression and without the presence of pre-existing flaws is it possible to generate tensile failure. Tensile fractures, however, become smaller and more distributed when a confining stress is applied. In the case of the unconfined specimen (Figure 5.36a) a final average stress of approximately 300MPa was induced in the model, while final average stresses induced in the confined specimen reached double that value (600MPa).

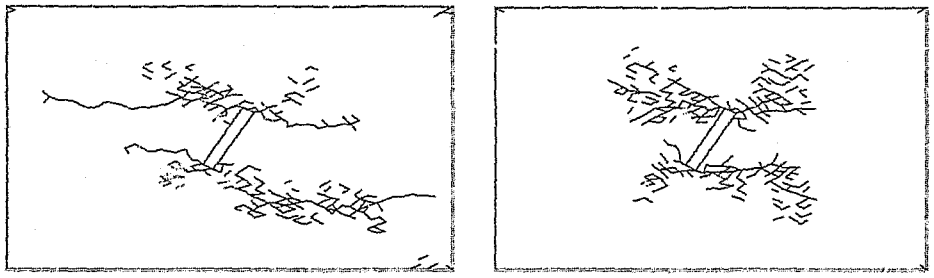

a) unconfined. b) vertical confinement of 10MPa

Figure 5.37 Hardening; cohesion before failure = 20MPa; after failure = 30MPa; tensile strength = 20MPa

In the unconfined case (Figure 5.37a) the induced final average horizontal stress was approximately 60MPa while a stress of approximately 85MPa was induced in the confined model (Figure 5.37b). It is of interest to note that in the simulation of hardening behaviour as shown in Figure 5.37, relatively large tensile (brittle) fractures occur again. The explanation for this phenomenon is the fact that hardening has only been applied to the cohesive strength, whereas the tensile strength has been kept constant. The tensile strength therefore becomes relatively small with respect to the increasing cohesive strength. As a consequence, tensile failure is favoured over shear failure at later stages in the failure development. For this reason, tensile failure may occur at locations which would not be expected from an elastic stress distribution as the preceding shear failure has caused a redistribution of stresses. Similar observations have also been made with FLAC simulations.

The discontinuities which are depicted in all these results are those discontinuities which become activated during accumulative displacement increments of the vertical boundaries. In the case of the hardening model in Figure 5.37, it is possible that discontinuities, which are activated during a particular displacement increment of those boundaries, cannot be mobilised any further due to their post failure strength increase. No distinction has been made in Figure 5.37 between discontinuities which were activated and subsequently could not be mobilised any further and discontinuities which were activated and remained activated upon further loading.

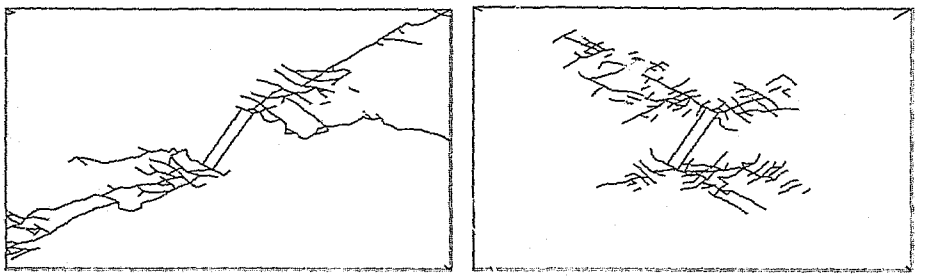

a) unconfined b) confined by a vertical stress of 10MPa

Figure 5.38 Moderate softening; tensile strength 20MPa;
cohesion before failure = 20MPa; after failure = 15MPa;
friction angle = 30degrees)

Figure 5.38 shows suppression of brittle failure when a confining stress is applied. The unconfined situation results in large, brittle fractures, which not only follow the direction of the major principal stresses (wing cracks), but also appear to form in an inclined orientation which is more typical of shear fractures. The average final horizontal stress is about 60MPa in the unconfined situation (Figure 5.38a) and approximately 80MPa in the confined situation (Figure 5.38b)

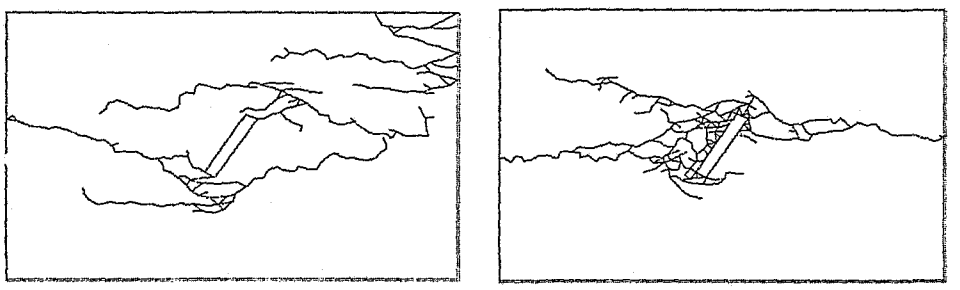

a) unconfined b) confined by a vertical stress of 10MPa

Figure 5.39 Complete softening; tensile strength 20MPA;
cohesion before failure = 20MPa; after failure = 0;
friction angle = 30 degrees

The failure associated with complete softening clearly involves larger individual fractures instead of a large number of smaller fractures. In the unconfined case (Figure 5.39a) an average horizontal stress of approximately 45MPa was finally induced while a n average horizontal stress of about 90MPa was induced in the confined case (Figure 5.39b). The confining stress does not appear to inhibit the formation of large individual fractures completely and some of these fractures even intersect the boundary finally. Fracturing initiating from the boundaries does occur in the unconfined case, but is suppressed in the confined case. It is not clear if any of the large scale fractures can be classified as a shear fracture.

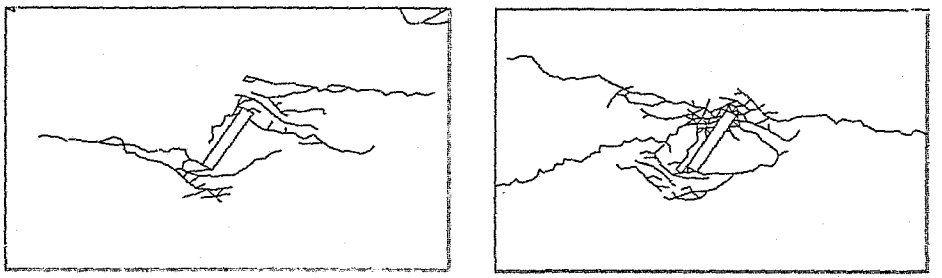

a) Unconfined b) confined by a vertical stress of 10MPa

Figure 5.40 Complete softening; tensile strength 10MPA;
cohesion before failure = 20MPa; after failure = 0;
friction angle = 30 degrees

The difference between Figure 5.39 and 5.40 is the tensile strength which has been assigned to the models. The effect of a reduced tensile strength does not seem to affect the final fracture geometry. The only noticeable difference took place in the final average horizontal stress induced in the confined case. While this stress reached approximately 90MPa in the case of a relatively high tensile strength (Figure 5.39b), a value of about 80MPa was obtained in the case of the reduced tensile strength (Figure 5.40b).

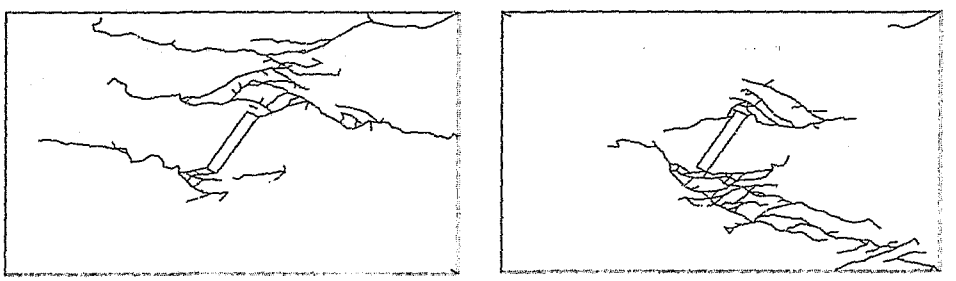

a) Unconfined b) Confined by a vertical stress of 10MPa

Figure 5.41 Complete softening; tensile strength 35MPa
cohesion before failure = 20MPa; after failure = 0;
friction angle = 30 degrees

Figures 5.39 to 5.41 show the effect of tensile strength in relation to cohesive strength in situations of total cohesion softening. An increase in tensile strength under unconfined conditions leads to an increase in failure associated with, and initiating from, the boundaries of the specimens. While initial failure takes place around the slot due to the stress concentrations which occur locally, subsequent failure can be triggered from the boundaries as well. Confinement suppresses boundary failure, but the effect of an increase in tensile strength can still be noticed in the differences between Figures 5.39b, 5.40b and 5.41b. In the last case the long, brittle fractures are replaced by relatively short fractures which occur in the pattern of a shear band. Although some failure appeared to be associated with the boundary in this particular case as well, the development of this shear band seems to be driven mainly from the slot. In the last simulation with the highest tensile strength of 35MPa (Figure 5.41), the final induced average horizontal stresses are 45MPa and 90MP for the unconfined and the confined case respectively. The same values were obtained for the simulation with the 20MPa tensile strength, which is shown in Figure 5.39.

In the following simulations a different post failure behaviour has been implemented in one of the simulations and its influence on the resulting fracture geometry is addressed.

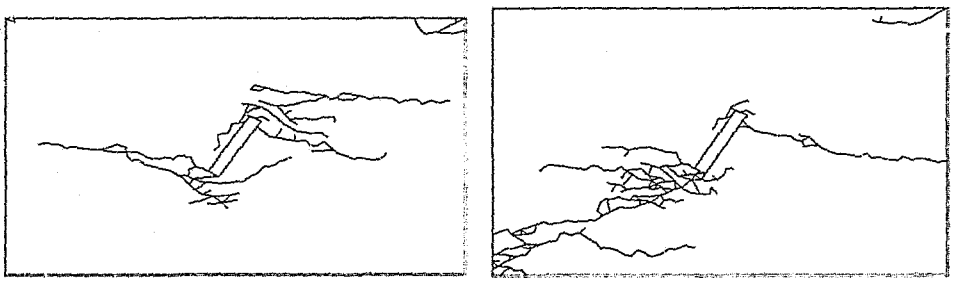

a) original post failure behaviour b) alternative post failure behaviour

Figure 5.42 Complete softening; tensile strength 20MPa; unconfined;
cohesion before failure = 20MPa; after failure = 0;
friction angle = 30 degrees

Figure 5.42 shows the results of two simulations with the same failure parameters. The difference between model a) and b) is the post failure response. Model b shows the result which has been obtained by introducing a minor adjustment to the post failure behaviour. In the original formulation the tensile strength is treated in such a way that when shear failure occurs under conditions of tensile minor principal stress, the tensile strength is reduced to zero. Model b is different in the sense that under similar conditions shear failure does not affect the tensile strength, but only the cohesive strength. This subtle difference leads to a substantial difference in the resulting fracture geometry as can be noticed be comparing Figure 5.42a with Figure 5.42b.

In the following simulation the effect of a reduced frictional resistance along the discontinuities is analysed. Both confined and unconfined situations have been modelled and a relatively high tensile strength has been assigned to the models.

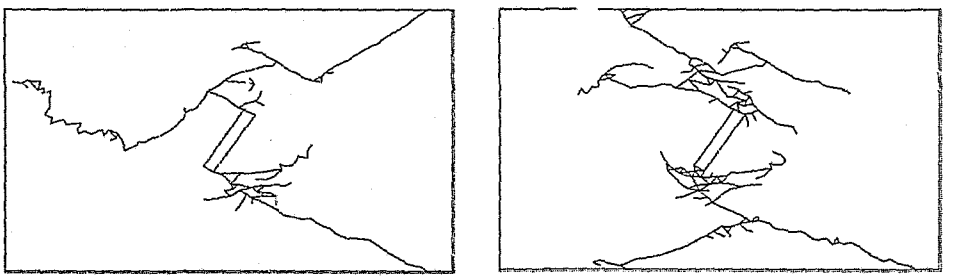

a) Unconfined b) confined by a vertical stress of 10MPa

Figure 5.43 Complete softening, friction angle 20 degrees;
cohesion before failure = 30MPa; after failure = 0; tensile strength = 50MPa

Figure 5.43 demonstrates the effect of a reduced friction angle under conditions of cohesion softening. Relatively large fractures are generated in both the unconfined and the confined situation. These fractures are mainly inclined with respect to the horizontal direction in which the major principal stresses operate and can therefore be associated with shear failure. The development of typical tensile fractures such as the wing cracks cannot be observed in these models and failure is only associated with the slot itself. The effect of the confinement is not immediately clear, although the resulting fracture geometry is affected by the presence of a confining stress and a larger number of fractures appear to be generated as well.

In the following examples some of the discontinuities have been selected to represent (weaker) flaws in the form of pores or sliding cracks without cohesion. The remaining discontinuities can only fail if their cohesive and/or tensile strength is exceeded as in the previous simulations. These models are supposed to provide a more direct representation of actual defects in rock like materials. The flaws are shown in grey in the following figures while the activated discontinuities are shown in black.

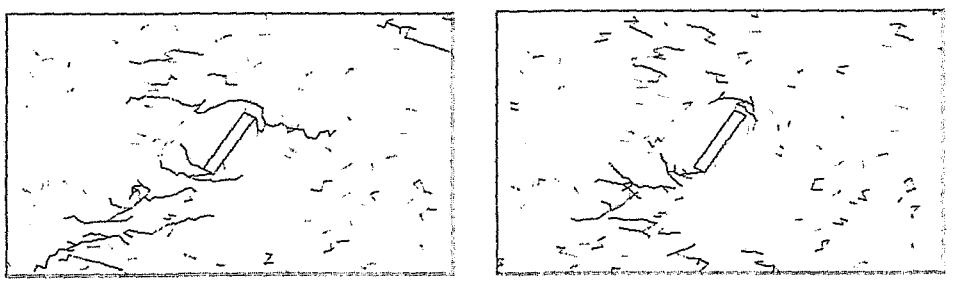

a) Unconfined b) Confined by a vertical stress of 10MPa

Figure 5.44 Complete softening; flaws in the form of pores; friction angle 30 degrees;
cohesion before failure =20MPa; after failure = 0; tensile strength = 20MPa

The results in Figure 5.45 can be compared with the results in Figure 5.39, where the same failure parameters and loading conditions have been used. The unconfined cases result in qualitatively similar behaviour, in the sense that relatively large individual fractures can be observed in both cases, while some form of a shear band appears to develop as well (Figures 5.39a and 5.44a). A comparison between the cases in which a confining stress has been applied (Figures 5.39b and 5.44b) shows a more different response. The "flawless" model of Figure 5.39b still produces relatively large individual fractures, while the simulation with additional pores (Figure 5.44b) only results in relatively small fractures, which do not appear to coalesce into a clear structure.

In the following simulations the discontinuities are only allowed to fail in tension. The additional flaws or pores can obviously induce local tensile stresses and in such a way activate the remaining discontinuities. This may be a more natural representation of the processes which control micro fracturing in a typical rock material. Micro fractures are in this case induced by tensile stresses only and no alternative failure criteria have to be assumed. No second order effects such as buckling are represented by DIGS and the distribution of micro fracturing is thus not influenced by such effects in these results.

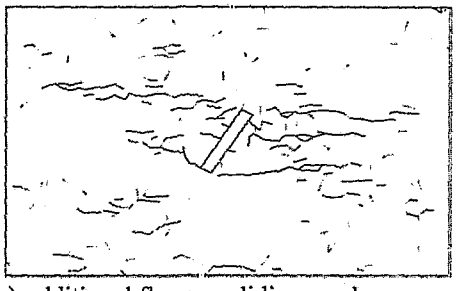

a) additional flaws as sliding cracks unconfined, flaw distribution X

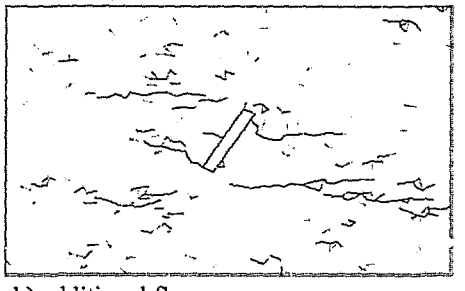

b) additional flaws as pores unconfined flaw distribution X

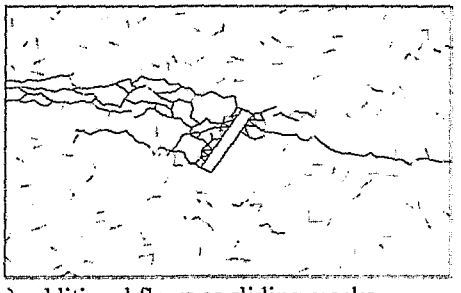

c) additional flaws as sliding cracks unconfined, flaw distribution Y

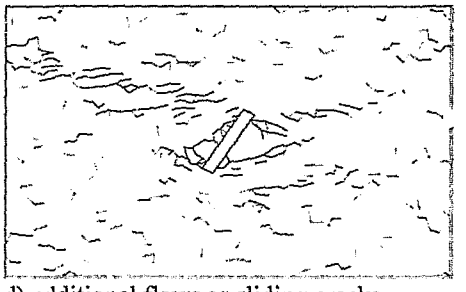

d) additional flaws as sliding cracks 20MPa confinement, flaw distribution Y

Figure 5.45 Tensile failure; additional flaws; tensile strength 20MPa

The flaw distribution in models 5.45c and 5.45d is different from the one in models 5.45a and 5.45b and it can be observed that this difference is also reflected in the resulting fracture pattern. The results appear to be less sensitive to the fact if flaws are represented as sliding cracks (model 5.45a) or as pores (model 5.45b). The application of a confining pressure as used in model 5.45d leads to reduction in the length of individual fractures while the formation of a shear zone appears to be promoted.

These results appear to have some similarity to the results shown in Figure 5.36, in which additional flaws have not been represented. A direct comparison with the "flawless" model in Figure 5.36 is however not possible due to a numerical restriction. The additional flaws restrict the maximum number of activated elements, so that the maximum number of activated discontinuities is different in both models. The general difference between the results of the "flawless" models of Figure 5.36 and the results shown in Figure 5.45 is however that these flaws have an additional effect on the resulting fracture geometry. A coalescence process between individual flaws can lead to a different fracture pattern from the pattern which is generated in the absence of such flaws. This difference can be observed by comparing the relevant results, and it is of special interest to note that the difference in flaw distribution (distribution X or Y) controls the resulting fracture pattern to a large extent. This observation therefore suggests that it is of importance to represent the microstructure of a particular rock in a realistic way.

In the following simulations a regular triangular mesh has been used (Figure 5.34). The results for a perfectly plastic and a moderately "brittle" material are shown in Figures 5.46 and 5.47 respectively.

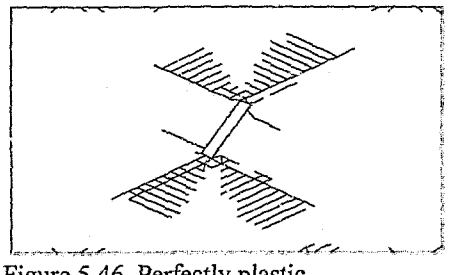

Figure 5.46 Perfectly plastic
regular mesh, uni-axial load
cohesion = 40MPa
Tensile strength = 40MPa
no internal friction

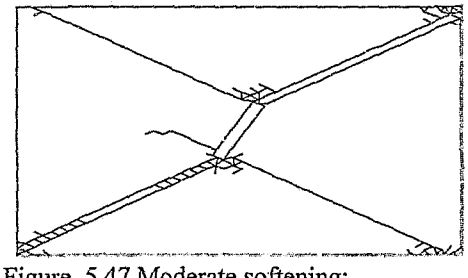

Figure 5.47 Moderate softening;
regular mesh, uni-axial load
cohesion before failure = 20MPa
after failure = 10MPa
tensile strength = 20MPa

Figure 5.46 and 5.47 show the resulting fracture patterns in a regular mesh. It is clear that the softening model (Figure 5.47) is far more affected by the mesh geometry than plastic model (Figure 5.46). In the last case the activated discontinuities appear to fill a yielding zone which can be expected to develop around the slot. The softening, brittle response, however, appears to be far more controlled by the detailed geometry of the mesh. A similar conclusion was reached in section 5.2.

The previous simulations demonstrate how the selection of material parameters can affect the resulting fracture geometry to a large extent. Especially those cases in which cohesion softening is simulated often result in fracture patterns which could be interpreted as shear fractures. The sensitivity with respect to minor changes in failure parameters and post failure behaviour also indicates that these simulations cannot be expected to lead to well defined results. As small disturbances in the input parameters appear to be amplified to a large extent in the results, such results, and thus the models, are inherently unstable. It is unclear to what extent the mesh geometry controls the results. While the non-softening models appear to be less sensitive to the change from a random mesh to a regular mesh, the softening models clearly produce a more pronounced shear fracture within the regular mesh than within a random mesh. The mesh density can also be expected to play a major role in this respect, but this effect has also not been analysed explicitly.

In the following simulations a random mesh of Delaunay triangles has been used again, but in these cases three slots are represented in the mesh. The main purpose of these simulations is to investigate the effect of neighbouring slots on the resulting fracture pattern.

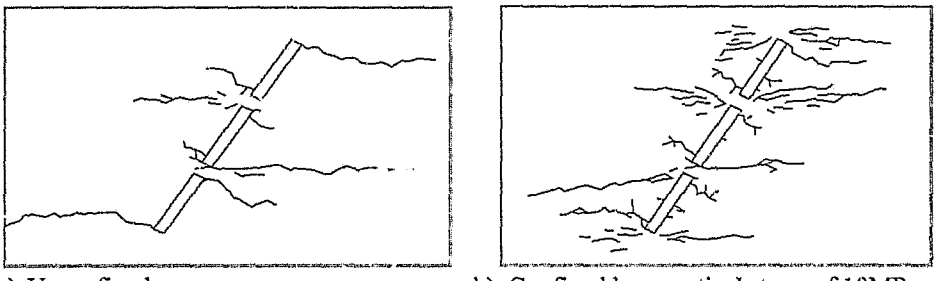

a) Unconfined b) Confined by a vertical stress of 10MPa

Figure 5.48 Tensile fracturing from multiple slots; tensile strength = 20MPa

When these results are compared with the results obtained for a single slot (Figure 5.36) it can be observed that similar fracture patterns occur. The slots do not coalesce due to the fact that shear failure is inhibited and the only effect of the interaction between the slots is a minor modification to the tensile fracture pattern due to a change in stress distribution.

In the following simulations in Figure 5.49, shear failure is allowed to occur as well by reducing the value for cohesion. It may be expected that coalescence of the slots can be reproduced in these simulations.

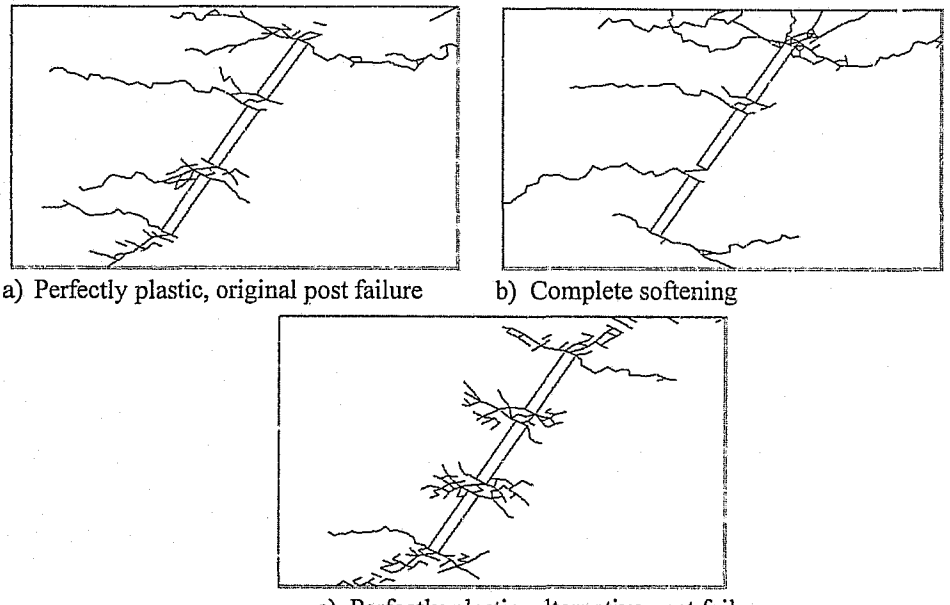

a) Perfectly plastic, original post failure

b) Complete softening

c) Perfectly plastic, alternative post failure

Figure 5.49 Multiple slots, uni-axial loading; cohesion = 20MPa; friction angle = 30 degrees; tensile strength = 20MPa

Figure 5.49 shows how brittle failure is controlled by parameters which control post failure behaviour. If the normal stress, acting on an element which is subjected to failure, is tensile, then the tensile strength in model 5.49a would be set to zero, irrespective of the value of the normal stress. This results in a brittle response under those conditions. Perfectly plastic failure is therefore only simulated under conditions of compressive normal stresses in this particular model. This response is in accordance with the original post failure behaviour.

The model in Figure5.49c shows a different response under the same conditions, as the tensile strength is maintained after failure under normal tensile stress, unless of course these stresses exceed the tensile strength. Failure therefore appears to correspond more to a ductile material in Figure 5.49c than in Figure 5.49a. The response is according to the alternative post failure behaviour. Ductility is often assumed to be non existent under tensile conditions in granular materials, but this assumption may not necessarily be justified. In the next section it will be demonstrated, for instance, how ductile behaviour under tensile conditions leads to more realistic results with respect to the fracture geometry.

All models show a coalescence between the individual slots, although the coalescence occurred at a relatively late stage in the softening model 5.49b, after the formation of a large number of fractures. This appears to suggest that the coalescence process is not associated with an extreme brittle behaviour, but requires ductile behaviour.

Comparing the result of Figure 5.49a with the result obtained from a single slot such as in Figure 5.35a, it can be observed that the fracture pattern in the case of the multiple slots contains longer tensile fractures. The response of the multiple openings therefore appears to be more brittle than that of a single opening. This may be explained from the combined effect of the individual slots which results in a different stress distribution. The closer proximity of the boundaries to the openings, in the case of the multiple openings, may also have an effect on the results. The displacements, which have been imposed on the vertical boundaries, were the same in the case of the single opening as in the case of the multiple openings and the induced average horizontal stresses were therefore approximately equal.

5.3.3 FRACTURING IN PUNCH-THROUGH SHEAR SPECIMENS

Davies et al. (1988) report experimental results from mortar specimens which were subjected to a loading configuration as shown in Figure 5.50. The dotted rectangle indicates the half symmetric region which is represented in the related numerical models. An analysis of the elastic stress distribution shows a concentration of high tensile stresses and high shear (differential) stresses near the tips of the notches (Figure 5.51). Simulating the fracturing process by assuming a tensile fracture criterion results in the formation of wing cracks as is demonstrated in Figure 5.51 as well. Such a result would be representative for the fracturing in extremely brittle materials , but it does not resemble the observed fracture patterns in these mortar specimens (Figure 5.50). The observed failure structures connect the opposing notches and allow total failure by localised shear deformation across these structures.

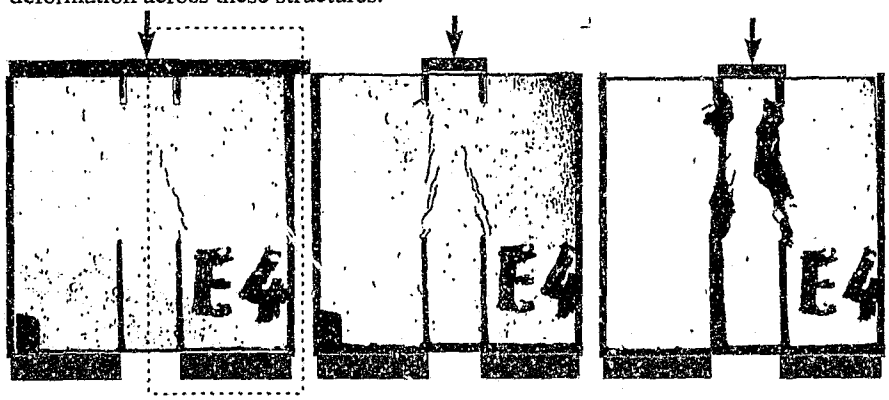

Figure 5.50 Development of en echelon fractures into a macroscopic shear fracture; punch-through shear test of mortar specimens (after Davies et al.,1988) loading from the top between two notches and support at the bottom

While it is obvious that these shear fractures consist of a set of micro fissures, it is not clear how these micro fissures form in the first place. The location and orientation of the micro fissures does not coincide with the *elastic* stress distribution as shown in Figure 5.51 when a tensile failure criterion is assumed. Davies et al. (1988) conclude therefore that these micro-fissures "cannot be due to tension, but must be due to shear". It is in this context of interest to note that the individual micro fractures shown in Figure 5.50 are in fact opening and must therefore be assumed to be formed in tension.

These tests indicate clearly that shear fracturing is preceded by a process of tensile micro fracturing. The location of these micro fractures is inconsistent with a linear elastic stress distribution in a continuum. This indicates that the actual stress distribution, at the onset of micro fracturing, may differ from the one shown in Figure 5.51. However, as the macroscopic fracture is however of more practical relevance, the focus of attention is often on the resulting fracture, which in this case obviously is a shear fracture. What controls the formation of such a shear fracture is not addressed here at all and still remains an area of misunderstanding. In order to investigate possible mechanisms for the formation of shear fractures in general, and this example in particular, the following numerical experiments have been used for analyses.

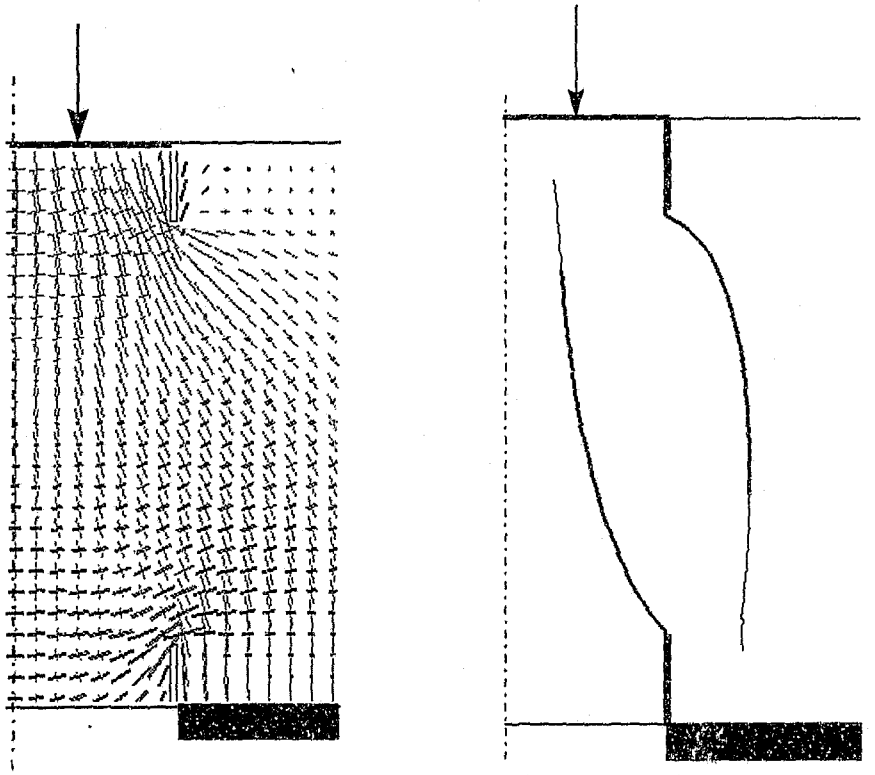

a) Linear elastic stress distribution (double bars denote tension)

b) Resulting mode I fractures

Figure 5.51 Tensile fracture formation from notches in the punch-through experiment; half symmetry as indicated in Figure 5.50 (DIGS result)

Explanations for the formation of shear fractures are often based on the assumption of theoretical, elastic stress distributions. In the context of geological models, which are based on the Riedel experiment (Riedel, 1929), in which a slab of clay is placed horizontally on two parallel adjacent boards, such explanations may lead to unrealistic conclusions. As one board is slid horizontally past the other one, a network of faults develops in the overlying clay layer, only after large amounts of straining. Most of the observed faults are termed "shears", because the elastic stress distribution at the onset of their formation does not suggest an alternative possibility. However, the fact that these so-called shear fractures are only observed in materials which do not exhibit an extreme brittle behaviour indicates a potential relation between brittle fracturing and ductile deformations. If ductile deformations precede the fracturing process, stress distributions will be affected and the assumption of elastic behaviour at the onset of fracturing may be completely misleading.

In order to test this hypothesis, the punch-through experiment shown in Figure 5.50 has been analysed with the use of the computer programs FLAC and DIGS. The results, which are reported in the next section, strongly suggest the association of shear failure localisation with ductile/plastic behaviour, which can affect the stress distribution to such an extent that tensile and brittle fracturing can occur at locations which would *not* be predictable from a *linear elastic* analysis. If shear behaviour is assumed to be associated with brittle behaviour only, without any possibility of ductile and/or non linear elastic deformations, results become unrealistic and effectively tend to reproduce (extreme) brittle material behaviour without the formation of shear bands. The conclusion from these results is therefore that the behaviour of moderately brittle materials is to a large extent controlled by processes which precede brittle failure.

These processes can be associated with the post yielding properties of such a material, and/or with sub-critical damage processes, which effectively result in non linear elastic behaviour. In order to understand the brittle fracturing processes it is essential to have knowledge of these processes. Brittle materials therefore distinguish themselves from each other to a large extent by the amount of (non linear, non elastic) deformation which can be absorbed before their maximum strength has been reached. This is directly related to the 'ductility' of the material

5.3.3.1 NUMERICAL MODELLING OF THE PUNCH-THROUGH EXPERIMENT WITH FLAC

Because of symmetry consideration only one half (the right hand side) of the punch-through specimens has been simulated. Five different scenario's have been modelled:

1. perfect plastic behaviour,
2. strain hardening behaviour
3. strain softening behaviour
4. tensile failure
5. strain softening (same strength as model 3, but more brittle post-failure behaviour)

The properties which have been used to specify the failure envelope and the post failure behaviour are listed in table 5.1

Table 5.1

	model 1 Perfectly Plastic	model 2 Strain hardening	model 3 Strain softening	model 4 Tensile failure	model 5 Strain softening
angle of internal friction	35degrees	35degrees	30degrees	30degrees	30 degrees
dilation angle	0	0	0	0	0
tensile strength	intersection	intersection	10MPa	10MPa	10MPa
cohesion @ 0 strain	10Mpa	10Mpa	10MPa	1000Gpa	10MPa
cohesion @ 0.0001 strain	10MPa	15MPa	10MPa	1000Gpa	10MPa
cohesion @ 0.0002 strain	10MPa	18MPa	8MPa	1000Gpa	8MPa
cohesion @ 0.0005 strain	10MPa	20MPa	5MPa	1000Gpa	5MPa
cohesion @ 0.0010 strain	10MPa	21MPa	5MPa	1000Gpa	0MPa
cohesion @ 0.0100 strain	10MPa	22MPa	5MPa	1000Gpa	0MPa
cohesion @ 1.0000 strain	10MPa	22MPa	5MPa	1000Gpa	0MPa

The results are shown in Figures 5.52. It is obvious that the "very brittle" simulations (models 4 and 5), in which relatively small amounts of strain are associated with relatively large decreases in strength, suffer from grid dependence, as the columns and rows allow the smallest thickness of shear bands and therefore attract most of the inelastic deformations. As the strain across a shear band increases with decreasing shear band thickness and the softening is directly associated with these strains, the narrowest shear bands will accommodate more softening and will thus be favoured as the weakest link. Due to these numerical artefacts, the models 4 and 5 tend to reproduce individual fractures which are shear driven (mode II); suggesting that shear fracture propagation has been simulated as a consequence of, and in response to, the occurrence of strain softening. These results can directly be compared with the DIGS results in a regular mesh (Figures 5.19 and 5.47) where failure localisation was also aligned with the grid. While mode II shear fracture propagation has indeed been reproduced in these simulations, it is obvious that the orientation of these fractures is completely dominated by the geometry of the grid. The results of the other models 1 to 3 in Figure 5.52 do not appear to suffer from this numerical artefact. The reason for this difference appears to be associated with the fact that the post failure behaviour in these models is more ductile than in the other models.

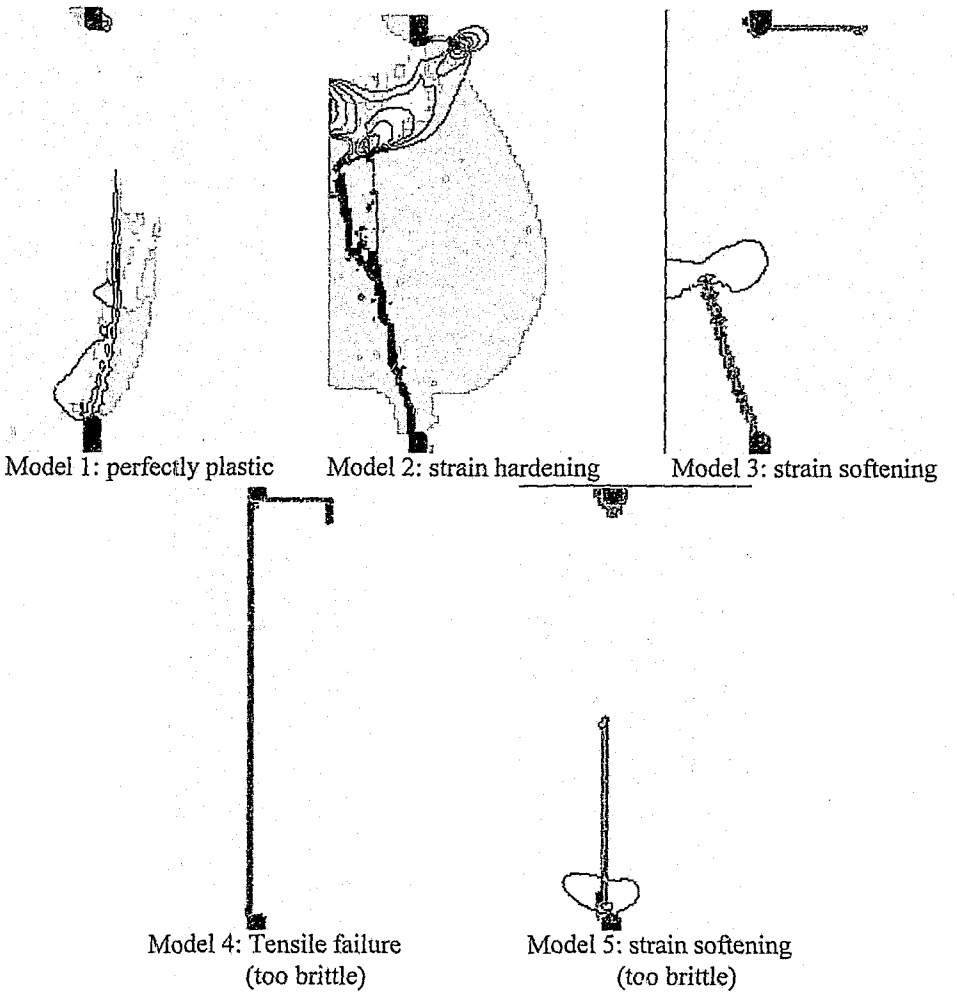

Figure 5.52 Simulation of the punch-through experiment with FLAC;
shaded zones indicate failure and contours indicate tensile stress

The results which are shown in Figure 5.52 show in fact three types of failure localisation. The first one is in the form of tensile failure and this has been obtained from model 2 and model 3 in Figure 5.52. A similar result is shown in Figure 5.51, which was based on a DIGS simulation. In model 2 strain hardening has been represented and a relatively large area (grey and white colours) is subjected to yielding. Within this region the tensile strength of the material becomes exceeded upon further loading and tensile failure takes place. Tensile failure is marked by black. In model 3 moderate strain softening is simulated, but tensile failure appears to take place in a similar form as in model 2. Some yielding (shear failure in grey) occurs in combination with this tensile, brittle failure as well, but the affected area is reduced to a very narrow zone in this case and can hardly be distinguished from the tensile failure zone (black colour). Both results have been obtained with a particular version of FLAC in which the tensile strength was continuously reduced according to the current value of the cohesion.

The second type of failure localisation results from model 1 (Figure 5.52) in which a perfectly plastic material is represented. Shear failure (indicated by a grey and a white colour) takes place in the form of a relatively narrow zone which initiates at both notches and expands into the specimen. The two shear zones ultimately coalesce and link both notches. Tensile stresses, indicated by contour lines, become increasingly concentrated inside this shear band and tensile, brittle failure can therefore be expected to be initiated from within the shear band. This result seems to match the observed behaviour qualitatively well. In this case a mechanism is operative which, through initial plastic deformations, causes tensile, brittle failure to occur at alternative locations from those predicted by (linear) elasticity. It should be emphasised that this particular result has been obtained without the occurrence of tensile failure. The tensile strength which was selected for this particular simulation was larger than the tensile stresses which were generated at any time.

The third type of failure localisation is really associated with mesh dependency and is not very meaningful in a physical sense. In model 4 of Figure 5.52 no allowance has been made for shear failure and only tensile failure could take place. This results in an extreme brittle behaviour which can not be resolved properly by the programme and leads to failure localisation along columns and/or rows of the grid. In model 5 of Figure 5.52 the same parameters have been used as in model 3, but a different post failure behaviour was simulated in this case. In this particular case the tensile strength is not reduced in accordance with a reduction in cohesive strength. As a consequence, tensile failure did not take place in the case of model 5, but localisation of shear failure resulted in a similar failure geometry as the tensile failure in model 4. The alignment with the mesh can in this case be explained from the fact that larger (shear) strains are generated in a shear band which consists of a single element, than in a shear band which consists of multiple elements. In a strain softening material these strains lead to a weakening of the material and the most effective weakening therefore takes place if the shear band is localised along a single row or column. Any other directions would involve a larger number of elements to accommodate the plastic deformation band.

Attempts to realise mode II in plane crack propagation on a laboratory scale usually fail because mode I growth takes over (Melin, 1986). In cases were mode II fractures are claimed to have been formed, the propagation can be seen to be a macroscopic phenomenon involving tensile (mode I) crack formation (Petit and Barquins, 1990), while fully developed shear fractures often appear to be associated with kinematically favourable conditions such as boundary interactions. Physically, the shear failure process seems to be associated with a gradual expansion of a damage zone around an area of stress concentration, which is the notch in this case. A shear fracture may develop at a later stage as a coalescing process between smaller scale mode I fractures which in this case appear to form in response to the expansion of the damage zone. The damage zone itself may be thought of as an area were micro-fracturing occurs or where relatively large (plastic) deformations take place.

The numerical model 1 in Figure 5.52 assumes the latter possibility whereby plastic deformations expand away from the notch and form a yielding zone. The localisation of tensile stresses within this zone is a result of the stress redistribution caused by the plastic deformations. Although not explicitly simulated here, the presence of such tensile stresses indicates the potential for mode I fracture formation as observed in the punch-through experiments. Within the yield zone a shear band (white area in Figure 5.52) is concentrated.

Model 2 in Figure 5.52 allows for strain hardening and the expansion of the damage zone requires a continuous increase of the applied pressure. A shear band does not develop in this particular model because the tensile strength becomes exceeded due to the increasing resistance of the material to deformation. This results in the formation of a tensile fracture as can be observed in Figure 5.52 and further deformations are absorbed by this fracture, so that the potential for shear banding has disappeared. The plastic deformations have an effect on the stress distribution in this particular case and result in the simulation of a tensile fracture which appears to be more realistic than the tensile fracture which has been reproduced in the explicit tensile failure simulation of model 4. The grid dependence does not seem to affect the failure localisation in the case of the strain hardening model 2, while it had a substantially influence on the result of the tensile fracture model 4 and on the result of the strain softening model 5.

The strain softening model 3 of Figure 5.52 resulted in the same type of failure localisation as the strain hardening model 2, namely a tensile failure zone. This result, in the case of model 3, can be explained from a combination of two mechanisms; namely plastic deformations preceding the tensile failure, and a simultaneous reduction of cohesive strength and tensile strength. This appears to allow a brittle (tensile) failure which does not suffer from grid dependence as in the models 4 and 5, most likely because a less brittle behaviour is represented.

The results of the perfectly plastic model 1 in Figure 5.52 resembles the results of the physical experiments quite well, in the sense that a mechanism for tensile fracture orientation and distribution has been captured by this model. An expanding yield zone which leads to a redistribution of stresses appears to precede the onset of brittle, tensile failure. In the case of strain softening such an expanding yield zone rapidly results in tensile failure (model 3), or in a "shear fracture" which is aligned with the mesh (model 5). In the case of the strain hardening model 2, the ever increasing shear resistance also results in tensile failure, because the increasing pressure ultimately exceeded the tensile strength.

The most realistic result was obtained from model 1 in Figure 5.52, due to the fact that an expanding yield zone caused a subsequent stress redistribution. A similar phenomenon occurred in the strain softening model 3, but in that case the stress redistribution led to the formation of a single, large scale tensile fracture. This in itself is a very interesting result, as it indicates that a tensile fracture can be generated, without the grid alignment as observed in the explicit tensile failure model 4, by representing the fracture process zone as a yielding material. However, the generation of a shear fracture could only be simulated in FLAC by preventing tensile failure from taking place and by using a perfectly plastic model. While these results are not claimed to capture the mechanisms which control and

lead to brittle shear failure, they do indicate the importance of yielding as a precursor to failure localisation.

The physical experiments showed variations in fracture geometry which can most likely be related to the detailed post yield behaviour of the material. While in these numerical simulations plasticity has been used to simulate the mechanism of ductile deformations before the onset of brittle failure, an additional model, in which the effect of micro damage is represented by a reduction in the Elasticity Modulus, has been used as well in order to represent the failure process. This model allows for the non linear pre-failure behaviour which is typical for brittle rock. Failure and post-failure is however not represented by this model. The result of the model is shown in Figure 5.53 where the varying Elasticity Modulus can be seen to cause tensile stress concentrations to occur inside the material rather than at the edge of the notch. Subsequent tensile failure may in that case be expected to take place at locations which are a certain distance from the notch itself. These locations will most likely shift with an expanding damage zone. The resulting failure pattern could thus be expected to be similar to the observed en echelon pattern depicted in Figure 5.50. This would suggest that a *non linear elastic* model may be a suitable alternative to the more cumbersome *inelastic* models. As the FLAC models do not allow a direct simulation of tensile fracturing, more advanced analyses could not be undertaken and it was decided to use a different approach, using DIGS, so that the tensile fracturing process can be more realistically represented.

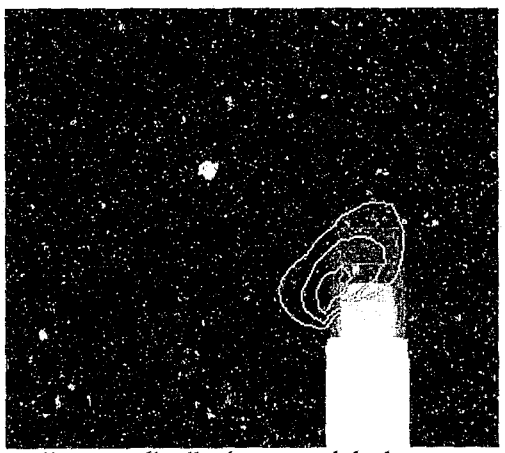

Figure 5.53 Tensile stress distribution around the bottom notch in the case of non-linear elasticity; (Elasticity Modulus variation is depicted by the colour intensity)

5.3.3.2 NUMERICAL MODELLING OF THE PUNCH-THROUGH EXPERIMENT WITH DIGS

Figure 5.51 already shows the tensile fracture geometry which results from a simulation with DIGS in which explicit tensile fracturing is reproduced. This section focuses on alternative failure criteria such as the Energy Criterion and the Mohr-Coulomb criterion. Some results from the Energy Criterion are shown in Figure 5.54 where it can be observed how different failure parameters affect the final fracture geometry. Tensile fracturing is most suppressed in the case where the internal friction angle equals zero under perfect

plastic conditions, while tensile fracturing is most dominant in the case of cohesion softening.

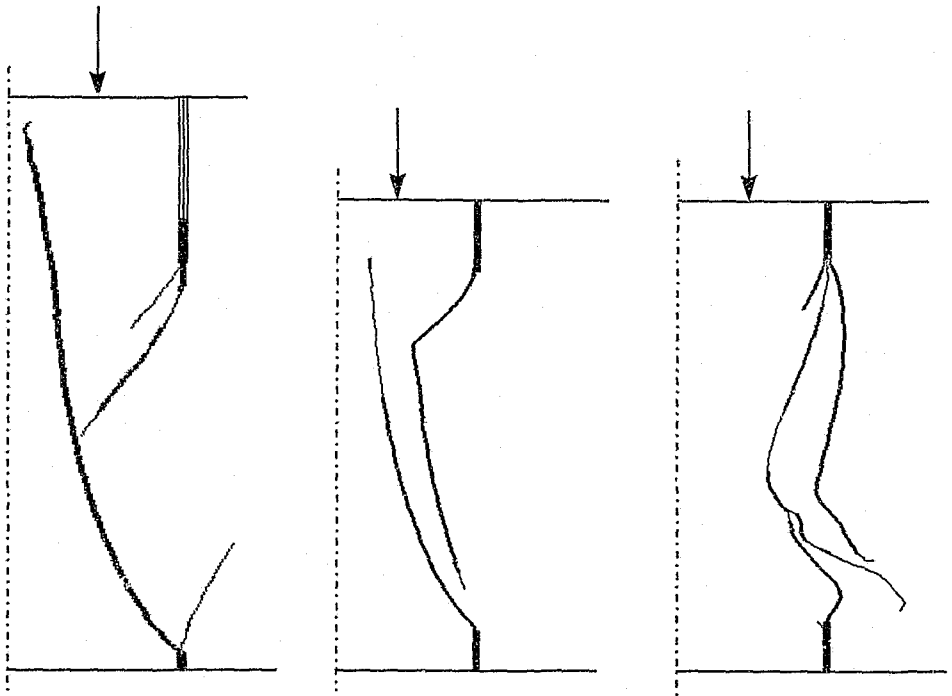

Perfectly plastic: friction angle = 30°

Cohesion Softening: friction angle = 30°

Perfectly plastic: friction angle = 0°

Figure 5.54 Fracture geometry in the punch-through experiment according to the Energy Criterion; black depicts crack opening and grey depicts shear; the thickness of the lines indicates the relative amount of crack opening or shear displacement (DIGS result)

Although none of these results matches the observed behaviour accurately, all of the simulations lead to a coalesce of the two notches. Shear failure is considered with the Energy Criterion and the resulting fracture pattern can therefore be expected to accommodate shear deformations. As the detailed fracture geometry is not realistic enough, the tessellation scheme has been used as well in order to represent the underlying rock micro structure. For this purpose a random mesh of Delaunay triangles, which is shown in Figure 5.55, has been selected .

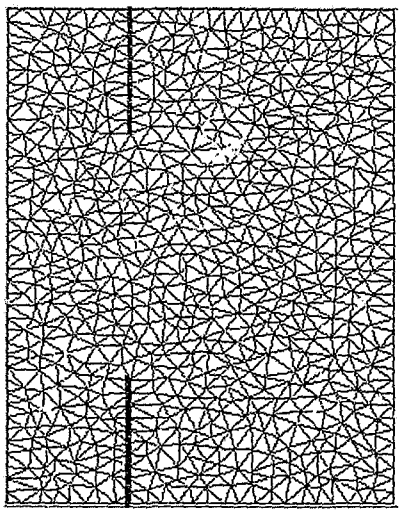

Figure 5.55 Tessellation mesh used for the simulations of the punch-through experiment; random Delaunay triangles; half symmetry similar to the previous models

No mesh variation has been allowed in the following simulations, so that the strength parameters are the only variables which may affect the results. The load is applied in the form of a forced vertical displacement along the top surface between the top notches. This is the area immediately underneath the arrow in the following figures. The bottom surface at the outside of the bottom notches is not allowed to deform vertically, while no restraint is imposed on its horizontal deformation. All other boundaries are unrestrained. The vertical deformation is applied in increments in order to reduce excess stresses and deformations on the system. Fracture activation takes place in an incremental, sequential fashion in the sense that after each fracture increment the stresses and displacements are updated. In the figures opening fractures are depicted in black, while fractures which are subjected to shear deformation are shown in grey. In all simulations use has been made of the same random triangular Delaunay mesh and no attempt has been made to analyse the influence of the mesh.

The parameters which are being investigated are the strength parameters of the Mohr-Coulomb criterion, which are imposed on all discontinuities. In this way the effects of cohesion softening and hardening can be investigated, as well as the relation between tensile and shear strength. The effect of the friction angle has also been addressed by varying the value of the friction angle in different simulations. The main purpose of this exercise is to establish which parameters promote tensile failure and which parameters promote shear failure and also to investigate possible relationships between post yielding behaviour and failure modes.

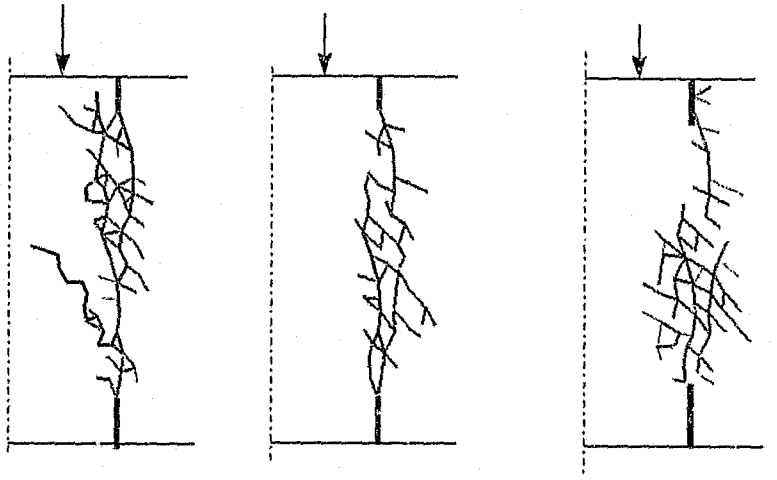

a) Complete softening b) Moderate softening c) Perfectly plastic

a) Cohesion before failure 15MPa; after failure 0
b) Cohesion before failure 15MPa; after failure 10MPa
c) Cohesion before and after failure 15MPa

Figure 5.56 Resulting fracture patterns: Tensile strength = 20MPa, friction = 30degrees.

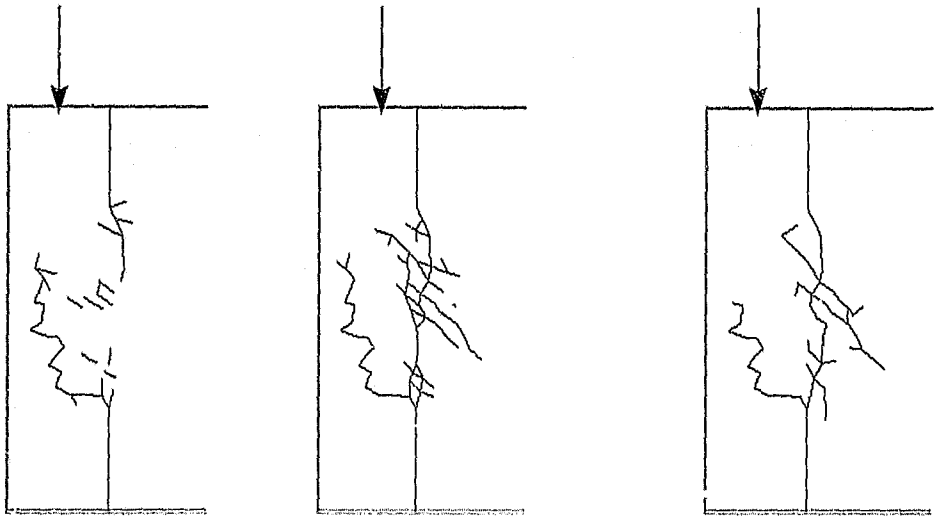

a) Complete softening b) Moderate softening c) Perfectly plastic

Figure 5.57 Same parameters as the models in Figure 5.56; but the presence of tensile stresses result in brittle failure in this case

In Figure 5.56 the effect of cohesion softening can be observed for a given tensile strength and friction angle. It is clear that while the perfectly plastic model only shows shear deformations, both the moderate and the total softening models show evidence of tensile

failure in addition to the shear failure. It is of interest to note that the tensile failure which occurs takes place at different locations from the tensile failure in a elastic continuum (Figure 5.51). This indicates the effect of shear deformation on subsequent tensile failure. All simulations result in an effective linking of the two notches.

Figure 5.57 is obtained from models with exactly the same parameters as the models which are shown in Figure 5.56. The difference is that in the constitutive formulation; if (shear) failure occurs while any of the principal stresses is tensile, the tensile strength is reduced to zero in the case of Figure 5.57. This effectively results in an additional brittle failure under such conditions and the effect can be observed from the difference in the results shown in Figures 5.56 and 5.57. In Figure 5.57 the additional brittle failure manifests itself primarily in the individual cracks which propagates towards the left from the bottom notch.

Figure 5.58hows the effect of tensile strength under various circumstances. A relatively low tensile strength leads to the formation of a tensile fracture without much shear failure. An increase in tensile strength can suppress the potential for tensile failure so that shear failure dominates. In both cases (a and b) a perfectly plastic material has been simulated. In the case of a strain hardening material, tensile failure appears to dominate even at a relatively moderate tensile strength, due to the fact that shear failure requires increasingly higher stress levels in that case.

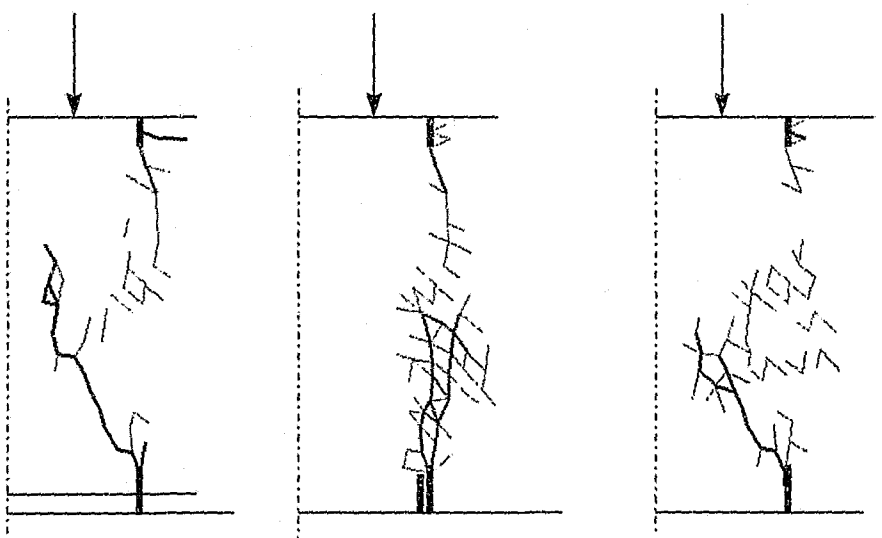

a) Low tensile strength, perfectly plastic (shear)

b) High tensile strength perfectly plastic (shear)

c) Hardening; average tensile strength

a) Tensile strength 15MPa
b) Tensile strength 25MPa
c) Cohesion after failure 25MPa (hardening); tensile strength 20MPa

Figure 5.58 Resulting fracture patterns: Cohesion before failure = 15MPa; friction angle = 30 degrees

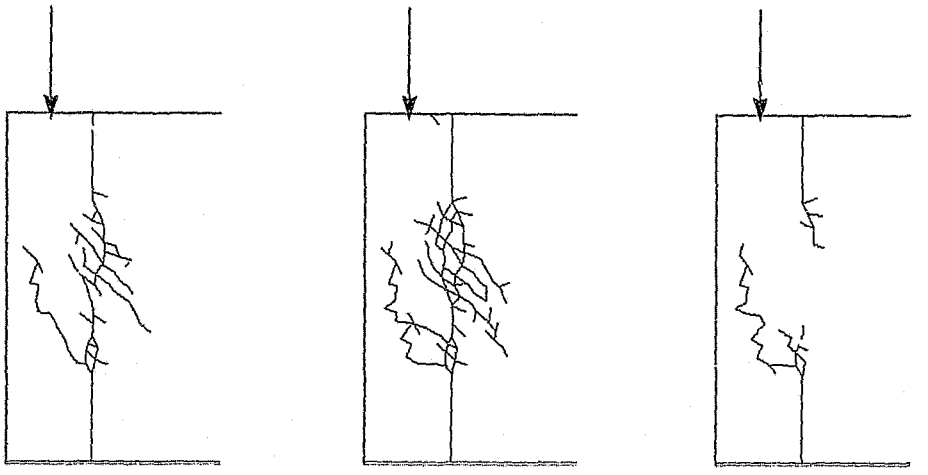

a) Low tensile strength perfectly plastic (shear)

b) High tensile strength perfectly plastic (shear)

c) Hardening; average tensile strength

Figure 5.59 Same parameters as the models in Figure 5.58, but the presence of tensile stresses results in brittle failure in this case

The results which are shown in Figure 5.59 are derived with the same failure parameters as those in Figure 5.58, but the post failure behaviour is different in both cases. In the model shown in Figure 5.59, shear failure under conditions of a tensile minor principal stress results in a loss of tensile strength. In the model shown in Figure 5.58, the tensile strength is not affected by shear failure. The difference between these two constitutive models is most clearly demonstrated in both combinations (b) where a relatively high tensile strength is represented. While a high tensile strength suppresses brittle, tensile failure in Figure 5.58, such a high tensile strength is rendered ineffective under conditions of shear failure in the case of the model shown in Figure 5.59.

As a consequence, the shear failure between the two notches never takes place without the brittle failure in the form of the individual fracture which propagates from the bottom notch towards the left. As this behaviour is not observed in the physical experiments, it can be concluded that the presence of tensile stress does not necessarily have to be associated with brittle failure as cohesion can be maintained during plastic deformations, even if a material is subjected to tensile stresses.

In the following simulations the effect of a reduced friction angle is investigated. In all cases perfect plasticity is ensured by maintaining a constant cohesive strength. Tensile strength has been varied and the post failure behaviour with respect to the tensile strength has been varied as well. The results appear to be quite realistic in the sense that a link between the notches is obtained in which tensile, opening fractures (black) can be observed as

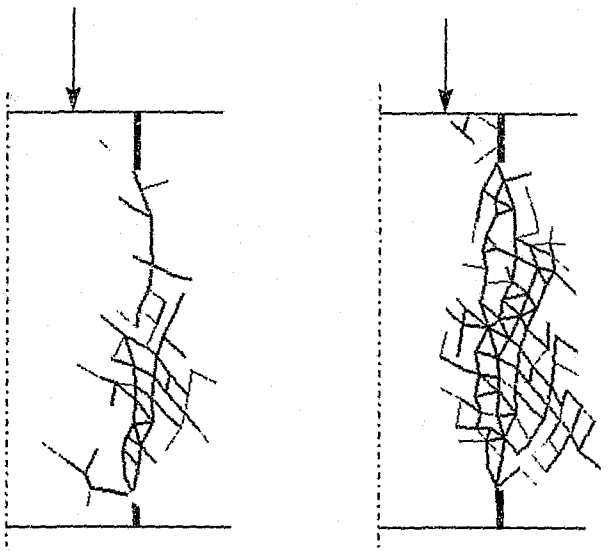

a) tensile strength 20MPA b) tensile strength 20MPa

a) Cohesion before and after failure 15MPa; friction 20 degrees; tensile strength 20MPa
b) Cohesion before and after failure 10MPa; friction 20 degrees; tensile strength 40MPa

Figure 5.60 Resulting fracture patterns

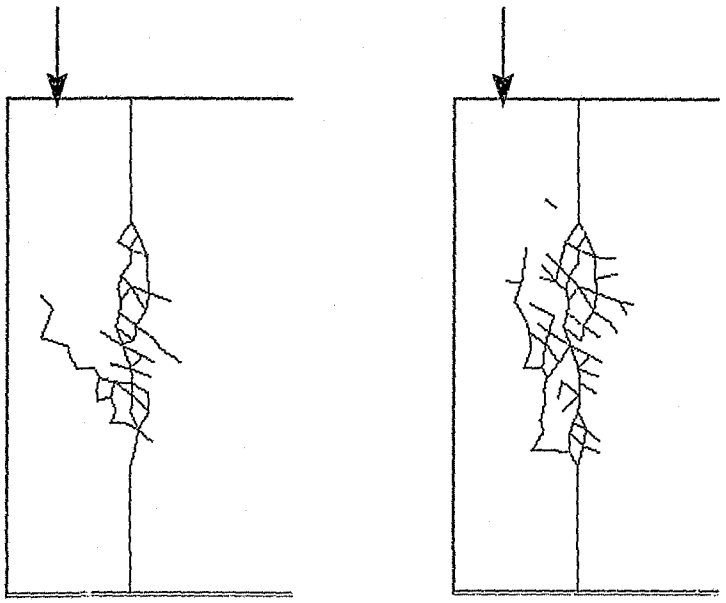

a) Tensile strength 20MPa b) Tensile strength 40MPa

Figure 5.61 Same parameters as the models in Figure 5.60, but the presence of tensile stresses results in brittle failure in this case

Figure 5.60 shows results for a relatively low friction angle. Models (a) and (b) show the effect of variations in tensile strength in a simulation of a perfectly plastic material. The reduced tensile strength does not affect results substantially in this case and a shear band between the two notches can be observed in both cases. The results shown in Figure 5.61 do not appear to produce the tensile, brittle fractures as the previous examples in which the same constitutive model led to a relatively large amount of brittle failure (Figures 5.57 and 5.59). This may be explained from the reduced friction angle which is favourable for failure under conditions of confining stresses, but increasingly limits failure under tensile stress conditions.

In the following simulations the effect of an increased friction angle is investigated. Perfect plasticity is assumed in all cases and the tensile strength is only limited by the values of cohesion and friction.

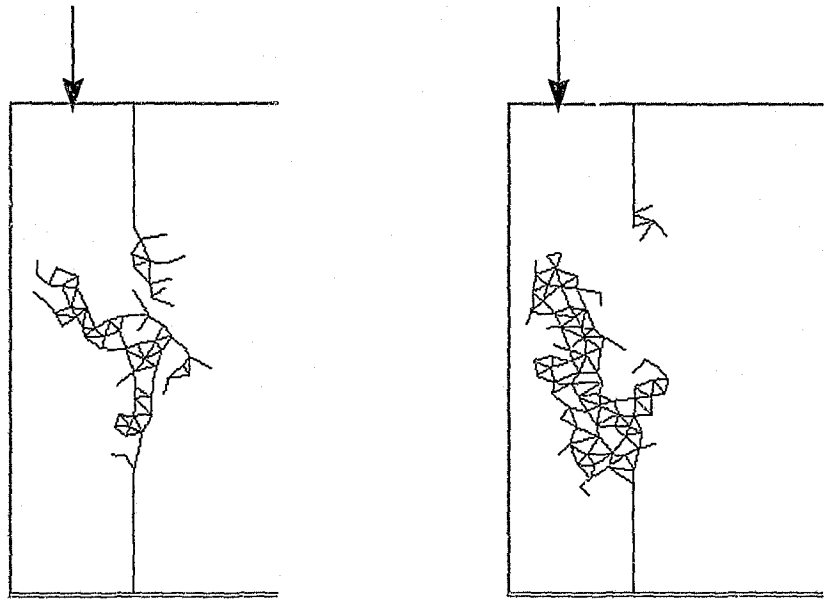

a) friction angle = 40 degrees; cohesion = 20MPa

b) friction angle = 50 degrees

Figure 5.62 Results for relatively high friction angles; cohesion after failure = 0; residual friction angle = 30 degrees

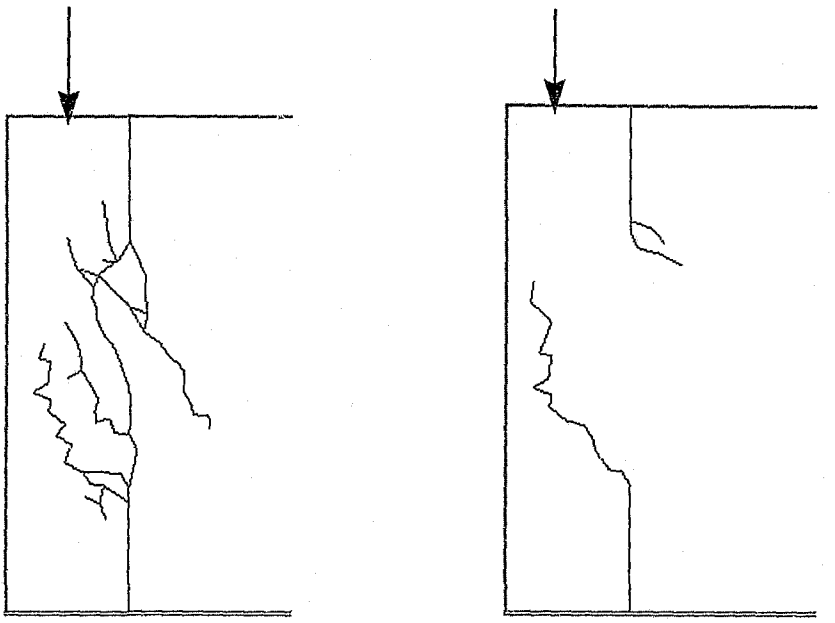

Figure5.63 Same parameters as the models in Figure 5.62, but the presence of tensile stresses results in brittle failure in this case

Figure 5.62 shows the effect of a high friction angle (steep slope of the Mohr envelope). Although it is not clear which of the discontinuities are subject to shear failure and which of them are subject to tensile failure, it is clear that in this case the notches are not being linked by the failure zone. The area of activated discontinuities appears to coincide with area in which tensile failure could be expected. Failure does, however, not seem to be localised but is relatively widely distributed over this area. This result is quite odd; the uniform distribution cannot be explained if tensile, brittle failure takes place, while the location of failure does not coincide with shear failure. The loss of cohesion after failure would be expected to result in brittle fracturing as well, but this is not reflected in the results.

Figure 5.63 clearly shows a more brittle response and the fracture pattern is completely different from the results in Figure 5.62. Both results do not match the physical results as a bridge between the two notches is not obtained in both cases. High friction angles do therefore not seem to be appropriate for the simulation of brittle shear failure in this case.

In the following simulations the effect of a small change in boundary conditions is investigated. Vertical loading is applied by forced displacements along the horizontal surface in between the notches underneath the arrow. These vertical displacements are incrementally increased and during each displacement increment incremental mobilisation of activated discontinuities is simulated. If the final vertical displacement is reached in six deformation increments of a particular size a certain fracture pattern as shown in Figure 5.64a is obtained. If the magnitude of these vertical deformation increments is doubled, so that the same final displacement is reached within 3 deformation increments, a different

fracture pattern, as shown in Figure 5.64b is obtained. This results demonstrates the sensitivity of the results with respect to a change in boundary conditions

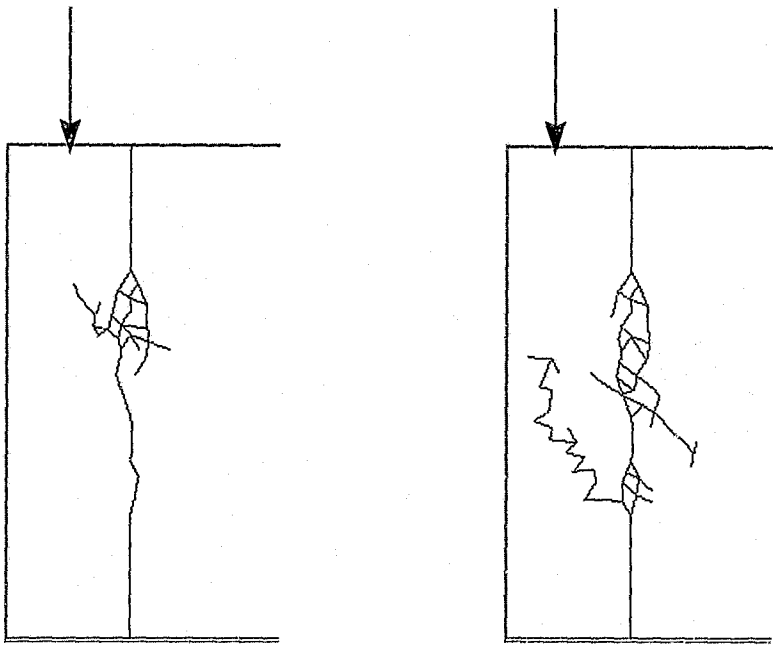

a) loaded in six deformation increments

b) loaded in three deformation increments

Figure 5.64 Effect of a small perturbation in boundary conditions; perfectly plastic in shear, Cohesion = 15MPa; friction angle = 20 degrees and tensile strength = 40MPa

Figure 5.64 shows how a minor change in loading conditions can lead to a major difference in the resulting fracture pattern. In model (a) fracturing is initiated at the second loading increment which coincides with the first loading increment of model (b). After each loading increment the stress field is adjusted to accommodate the additional deformations before any additional fracturing is allowed. The conditions after the second loading increment in model (a) and the first loading increment in model (b) should therefore be exactly the same as the (elastic) stress distribution must be the same. However, small deviations in the numerical solution do occur and result in the selection of different elements for failure initiation. The choice of the first element to fail will affect subsequent stress distributions and associated failure patterns. It is for this reason that small perturbations can affect the selection between elements which are more or less equally prone to fail. As the choice of a particular element influences the subsequent failure path, especially under conditions of brittle failure, such a choice could load to substantial differences in the resulting fracture pattern as can be appreciated from Figure 5.64.

In the final simulations the friction angle has been reduced to small values. Cohesion softening has been assumed as well in these models.

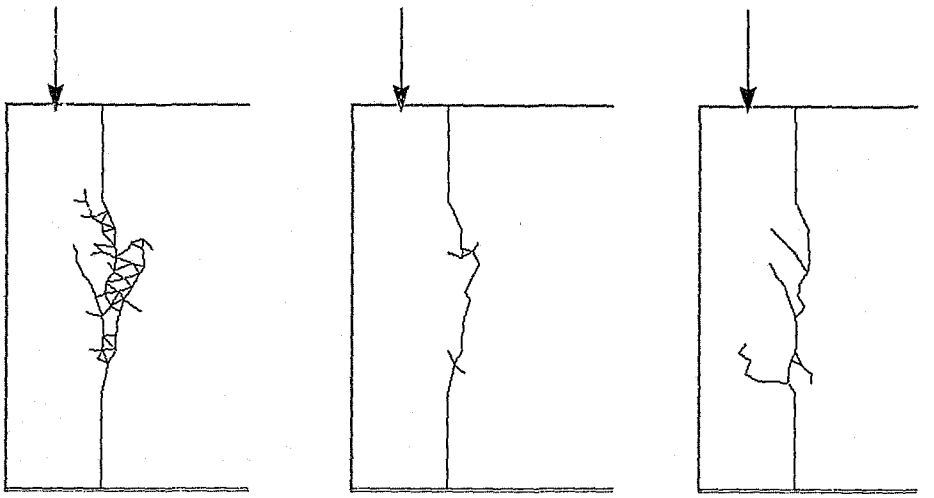

a) friction angle 15 degrees, b) friction angle 15 degrees, loss of tensile strength upon failure in shear (b and c) c) friction angle 20 degrees

Figure 5.65 Low friction angles; complete softening; cohesion before failure = 25MPa; tensile strength controlled by cohesion and friction angle

Figure 5.65 shows the results for a brittle material with a low friction angle. In all models failure develops between the two notches and tensile fracturing appears to be completely suppressed in model (b). Model (a) demonstrates a uniform distribution of failure in a similar fashion as the models with the higher friction angles in Figure 5.62. It is not clear why this apparent non brittle failure occurs in a model in which the input parameters dictate a brittle behaviour. The difference between model (a) and model (b) is again the constitutive formulation which enforces the loss of tensile strength in model (b), if shear failure takes place while any of the principal stresses is tensile. In model (a) the constitutive formulation only allows tensile failure once the tensile strength is exceeded. Shear failure is thus only controlled by the pre and post failure properties of the cohesion and friction angle in that case. In model c) a tensile fracture develops as well; the friction angle in this particular model is higher than in the models (a) and (b).

Although a fracture zone develops between the two notches in the models of Figure 5.65, the mechanism of fracturing does not appear to resemble the observed behaviour of the experiments shown in Figure 5.50 in any detail. In fact none of the models has been able to reproduce the echelon formation of tensile fractures, followed by a coalescence and subsequent formation of a shear fracture. The simulations depicted in Figures 5.56, 5.58, 5.60 and 5.64 show evidence of tensile fracturing inside a shear band and appear to reproduce the observed behaviour to a certain extent. The FLAC model 1 in Figure 5.52 also shows a similar effect. These simulations indicate that the stress distribution which precedes the formation of the tensile fractures must be different from a (linear) elastic one. It is questionable whether a correct stress distribution is obtained by the occurrence of

shear failure as has been simulated in the numerical models presented here. Factors which have not been addressed here may be of more relevance to this problem. Such factors could include flaw distribution, mesh geometry, mesh density, three dimensional effects, dynamic effects, etc. In order to obtain a better insight in the response of various brittle materials to excess loading, such factors need to be investigated. As current numerical models fail to reproduce observed behaviour accurately, the reason for this shortcoming has to be identified in order to progress in this field.

Besides the effect of the conventional input parameters, the effect of the mesh geometry, the effect of flaw distribution and the effect of changes in constitutive behaviour, deviations in loading conditions can apparently also be amplified and lead to relatively large deviations in the resulting fracture geometry. All these effects have to be considered in order to appreciate the potential for scattering in results, not only results from numerical simulations, but equally so results from real materials, as real materials would respond in a similar fashion to changes in properties, property distributions and loading conditions.

The effect of tensile strength in relation to the cohesive strength very clearly affects the development of the typical tensile wing crack. Cohesion softening does not appear to influence the resulting fracture pattern to a large extent, but the mode of fracturing changes from shear to extension with increasing softening. High friction angles, in combination with extremely high tensile strengths (figure 5.62 and 5.63), result in fracture patterns which are at odds with expected behaviour in the case of Figure 5.62. It is not clear why brittle failure is not reproduced in that particular case. Figure 5.63, for which an adjusted constitutive model has been used, shows a result which is more in line with the input parameters.

Low friction angles appear to promote the formation of a shear band between the two notches. This result can be associated directly with the promotion of failure under confining conditions and the suppression of failure under tensile conditions due to the relatively shallow slope of the Mohr-Coulomb criterion in stress space. Tensile failure is promoted by the constitutive model which enforces brittle failure if any of the principal stresses happens to be tensile. Suppression of tensile failure is therefore more effectively achieved with the other constitutive model, in which brittle failure is only associated with direct tensile failure or with cohesion and/or friction softening.

5.4 CONCLUSIONS

In general, it can be concluded that the results which have been shown in this section are sensitive to a large number of factors. The tessellation schemes introduce an additional parameter in the form of a mesh, and this parameter proves to influence the results to a large extent as well, especially if brittle behaviour is simulated. The distribution of flaws also has an effect on the results, and this effect may not be similar to that of the mesh geometry.

No analysis has been made with respect to the density of the mesh, but it is likely that that parameter may have an effect as well. The effect of conventional parameters such as friction, cohesion and tension is obviously quite noticeable and it not obvious how these

parameters should be calibrated when they are related to the behaviour of individual discontinuities inside a material.

Even with the more sophisticated tessellation schemes, observed results from physical experiments could not be matched in detail. While the purpose of these numerical models is obviously not an exact reproduction of complicated, real behaviour, it is essential that fundamental basic mechanisms are represented by the models. If this is not the case, the physical basis of such models becomes highly questionable. It is clear that failure localisation processes depend to a large extent on the micro mechanical structure of a material. If the simulation/reproduction of these processes is required, the appropriate representation of the micro structure can not be avoided. Although the models which have been presented here do allow a certain representation of the micro structure, be it the grid of the Finite Difference models, or the tessellation schemes of the Displacement Discontinuity models, it is unlikely that any of these representations is sufficiently accurate to be able to generate realistic results in terms of failure localization.

A general observation is that the behaviour of brittle materials is to a large extent affected by the amount of plastic deformation which can be observed before their maximum strength is reached. The numerical simulations demonstrated that such plastic shear deformations can affect the stress distribution to such an extent that tensile, brittle fracturing can occur at locations which are not predictable from a conventional linear elastic analysis. If shear failure is assumed to be controlled by pure brittle behaviour, without ductile and/or non linear elastic deformations, numerical results become unrealistic.

The models which are used here are still too empirical and are not designed to capture accurately any micro mechanical structures, which are of a three dimensional nature. Global behaviour can often be reproduced in a satisfactorily way by these models, as the calibration of the relevant parameters is also done at a global scale. The micro mechanical processes are not explicitly reproduced, nor are they required in order to capture the global behaviour of a specimen in many cases. However, if localisation of failure takes place at a scale of practical importance, global behaviour will be affected and the failure localisation needs to be accounted for. Many numerical models allow for the simulation of failure localisation, but these simulations are not based on micro mechanical processes of fracture initiation and coalescence, but on some empirical formulation, either involving a constitutive description of uniform material behaviour, or explicit large scale fracture growth rules.

Such empirical models can be extremely useful for the efficient simulation of (large scale) effects once appropriate calibration has taken place. In order to have confidence in such empirical models, it is necessary that the underlying mechanical behaviour and the inherent assumptions and simplifications which have led to the formulation of the empirical models is clearly understood. At present such an understanding has not been achieved. The micro mechanical processes which result in failure localisation on a large scale are often not obvious or properly identified and the formulation of empirical models can therefore at best be a good guess. An appropriate understanding and representation of relevant micro mechanical processes is thus required before any progress can be expected in the numerical simulation of failure localisation in a variety of brittle materials.

6.0 APPLICATIONS

6.1 FRACTURE FORMATION AHEAD OF STOPE FACES

6.1.1 Introduction

The formation of face parallel fractures ahead of a tabular longwall stope in a homogeneous rockmass cannot be related to mode I fracturing as (global) tensile stresses are absent in such a situation. While the presence of geological discontinuities may explain the initiation and propagation of tensile fractures ahead of a typical stope face, such a possibility has been excluded for the purpose of this analysis. In situ observations reveal the presence of fractures up to a distance of 5 metres in front of the stope face. These fractures are often separated by regions of intact rock and the density of fracturing increases with decreasing distance from the stope face (Adams et al., 1981; Legge, 1984 and Brummer, 1987). Typical laboratory experiments of brittle rock do not show such a fracture pattern and the failure in the abutments of the openings in such experiments is best described by uniform crushing, without any evidence of localisation and discrete fracturing (Gay, 1984). While the difference between laboratory results and in situ observations could be attributed to many factors, an obvious factor appears to be the absence of discontinuities in the laboratory tests. This in itself may be a satisfactorily explanation for some observed behaviour, but is not necessarily complete.

In tri-axial compression tests on brittle, homogeneous rock, ultimate failure is typically associated with the occurrence of one or more discrete macro fractures which are inclined with respect to the principle loading direction. Such shear fractures may also occur around highly stressed excavations if similar loading conditions are encountered. Shear fracturing offers an explanation for the observed separation of fractures and it also enables the relaxation of stresses in an all compressive stress field. In the following numerical simulations, the formation of shear fractures in a homogeneous, elastic medium is analysed. Both DIGS and FLAC have been used for this purpose.

6.1.2 DIGS SIMULATION OF SHEAR FRACTURING AHEAD OF A STOPE FACE

Two fracture criteria have been used for the simulation of shear fractures, namely the Excess Shear Stress criterion and the Energy criterion. As has been shown in Chapter 4, the first criterion is more prone to unstable behaviour when local tensile stresses are induced and the resulting fracture geometry shows in general a relatively small inclination with respect to the direction of the principle stresses. The Energy criterion produces results which can be better related to shear fractures as defined by a Mohr-Coulomb criterion. Both criteria have been applied in the following simulations and it is of interest to note that especially the ESS criterion generates remarkable results. An example of a simulation with that criterion is shown in Figure 6.1.

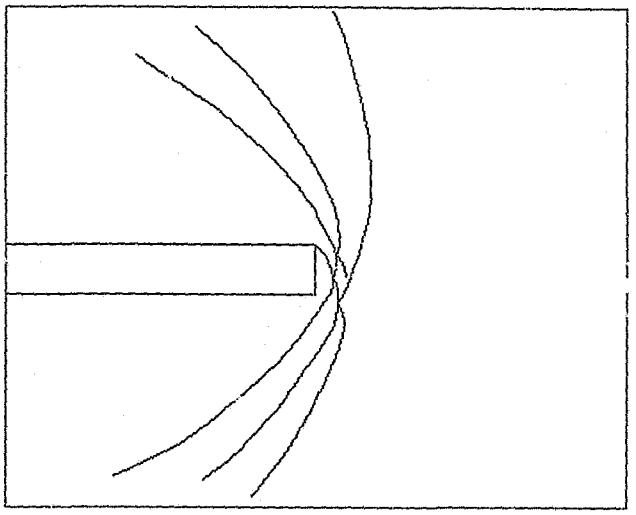

Figure 6.1 DIGS simulation of shear fracturing ahead of an advancing stope face; Excess Shear Stress criterion

The fracture pattern in Figure 6.1 has been obtained by initiating fractures at those locations which indicated the maximum potential for failure, after a previous fracture had fully developed. The first fracture initiated from one of the corners of the stope; the right hand top corner was arbitrarily chosen in this case, but all subsequent initiation points were associated with unique maximum values for fracture initiation. The fractures initiated in a direction corresponding to an optimum "shear" inclination with respect to the direction of the principal stresses, but gradually developed in a direction which was more aligned with the principal stress direction. This is in accordance with the example of Chapter 4 where a similar results has been obtained.

In the following simulation the Energy criterion has been applied and the resulting fracture geometry is shown in Figure 6.2. Fractures have initially been allowed to initiate from both edges of the excavation and the locations of subsequent fracture initiation points have been selected based on their potential for fracture initiation. This process is the same as the one used in the previous example.

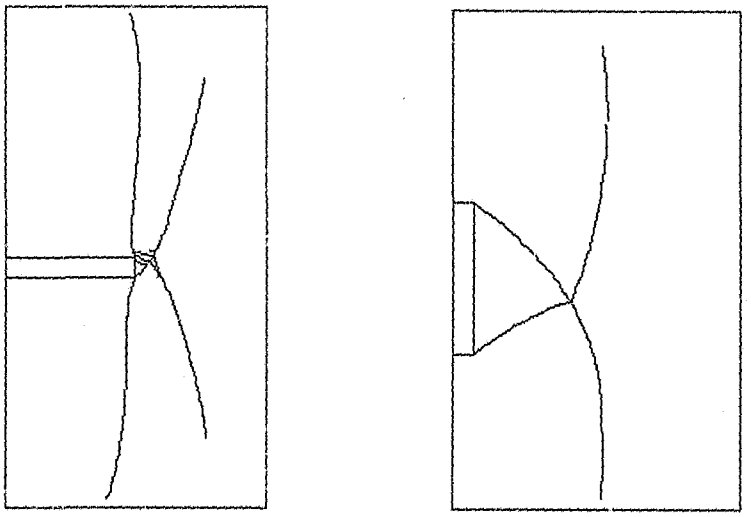

a) Shear fracturing ahead of a narrow slot b) Shear fracturing ahead of a wide slot

Figure 6.2 DIGS simulations of shear fracturing ahead of an advancing stope face according to the Energy Criterion

The fracture formation ahead of a narrow slot is similar to that of a wide slot, and in both cases the formation of a single wedge can be observed (Figure 6.2). The explanation for these results may be found in the difference between the Energy criterion and the ESS criterion. Figure 6.1 shows the development of multiple fractures and wedges ahead of a narrow slot with the use of the Excess Shear Stress criterion, but only two shear fractures develop from the slot edges when the Energy criterion is applied. As the Energy criterion leads to fractures which form in such a way that a maximum amount of shear deformation is absorbed, it can be argued that excess stresses are completely relieved by primary fracturing and the potential for secondary fracturing is reduced to a minimum. This is in contrast to the Excess Shear Stress criterion where secondary fracturing does take place and where excess stresses are apparently not completely dissipated by the primary fractures. Fractures which are generated from the ESS criterion deviate more readily from the theoretical shear fracture inclination and this results in the incomplete absorption of excess stresses. The potential for secondary fracturing is therefore available from excess stresses which were not relieved by primary fracturing.

The results from the Excess Shear Stress criterion in Figure 6.1 are intuitively appealing, and resemble the conceptual model of fracturing around a tabular stope according to Adams et al. (1981) more closely than the results from the Energy criterion. The Energy criterion leads to results (Figure 6.2) which have more in common with the conceptual model of shear fracturing by Brummer (1984), except for the fact that in Brummer's model multiple shear fractures are assumed to form ahead of a longwall stope. It should however be realised that results from the ESS criterion are caused because an efficient absorption of excess shear stresses is not taking place in that case. As a result a fracture which is a combination between a shear fracture and a tensile fracture is promoted. The fact that such a result appears to be more realistic than the results from the Energy criterion may indicate

that shear fracturing is not such a common phenomenon as is often assumed. While shear failure and shear deformations obviously do occur, this may not necessarily happen by the formation of shear fractures. Further research should establish if and under which circumstances (brittle) shear fracturing takes place.

6.1.3 FLAC SIMULATION OF SHEAR FRACTURING AHEAD OF A STOPE FACE

In order to obtain the results which are shown in Figure 6.3, an opening with a small span to height ratio had to be created, instead of a more realistic large span to height ratio, typical for a stope. Although the DIGS simulations from Figure 6.2 seem to suggest that the span to height ratio of the excavation does not influence the mechanism of shear failure, it was found that no realistic results could be achieved with FLAC for large span to height ratio's. This may be due to the fact that numerical problems dominated the results in those cases.

The numerical problems which occurred were in fact related to the localisation of failure. In the cohesion softening models, localisation of failure typically occurred along columns or rows of elements if rectangular openings with a relatively large span and narrow height were simulated. These results reflect the mesh sensitivity of FLAC. By simulating smaller spans, the stress concentrations in the abutments are reduced and localisation of failure appeared to occur without being dominated by the mesh. The rate of cohesion softening with respect to generated plastic strain also has an effect on the mesh sensitivity as has been demonstrated in section 5.3.2. The combination of stress concentrations and rate of softening will therefore determine if failure localisation will be dominated by the mesh or not.

The following parameters were used for the Mohr-Coulomb strain softening model in Figure 6.3:

- cohesion at yield until a plastic strain of 0.01%: 10.0MPa
- residual cohesion after a plastic strain of 0.05%: 0.2MPa
- angle of internal friction 40°
- dilation angle 0°

These values allow for brittle, strain softening behaviour, which was is requirement to obtain fully developed (shear) fractures. Figure 6.3 shows the result of a typical FLAC simulation.

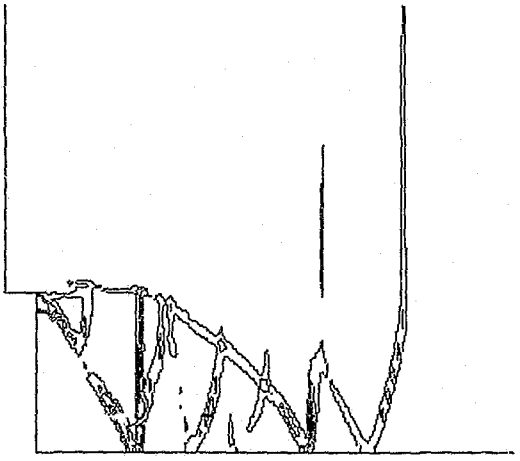

Figure 6.3 FLAC simulation of failure in the abutment of an excavation; Quarter symmetry, vertical stress 60MPa, horizontal stress 30MPa, contours of plastic strain

From Figure 6.3 it can be seen that the shear bands form a pattern of wedges in the side wall of the opening. The area which separates the shear bands is however not completely intact, as it has been subjected to plastic deformations. The shear bands form within the yielding material and brittle failure (loss of cohesion) mainly takes place within these shear bands. This result is different from the DIGS simulations where shear fracturing has been simulated in an elastic, intact medium with larger stope spans. It was not possible to produce similar results with FLAC because larger stress concentrations and a more brittle material behaviour would invariably lead to numerical problems associated with failure localisation. It was for this reason decided to abandon this approach and no further simulations of this kind have been performed.

The results shown in Figure 6.3 nevertheless give an indication of the potential for shear fracture formation ahead of an advancing mining excavation in a homogeneous rock mass. Due to the numerical problems associated with failure localisation it was unfortunately not possible to simulate a more realistic model of a longwall stope. In this particular simulation uniform yielding precedes the formation of the localised shear fractures. Future research should be conducted to investigate this aspect further, as the plastic deformation processes which precede failure may be of major importance.

6.2 BEDDING PLANES

6.2.1. General

Bedding planes are discontinuities separating different layers of sedimentary deposits. Their presence is quite common in most of the hangingwalls and footwalls of the deep level gold bearing reefs in South Africa, except for those reefs were the hangingwalls consists of lava deposits. Due to the nature of bedding plane formation, their orientation is usually more or less parallel to that of the neighbouring reefs. Depending on detailed geological sedimentary processes, the thickness of the layers, the contents of the layers, the thickness of the beddings themselves, the contents of the beddings and associate properties such as geometry, cohesive strength, stiffness, friction etc. can vary considerably.

The fact that these geological structures represent natural weaknesses or "flaws" in the rockmass around most deep level stopes makes them important features from a mechanical point of view as resistance against deformations along these planes can be severely limited. For this reason they are commonly recognised as sources of inelastic deformations around such stopes. In this section the influence of bedding planes on parameters such as closure and stress distribution and their effect on the formation of mining induced fractures is investigated.

Although the problem of deformations and stress distributions in layered strata appears to be relatively simple, it is an extremely demanding one from a numerical point of view. The geometry of layered strata is effectively related to a series of beams which are stacked on top of one other. The transmission of vertical forces and stresses along these beams towards the abutments induces bending moments and associated deformations and stresses inside such beams. Those deformations and stresses are of practical interest because they may represent the closure values and the actual stress levels in the hanging and footwall layers around stopes. Unfortunately the numerical representation of bending beams by the displacement discontinuity method as implemented in DIGS, using linear variations of stresses and deformations along discontinuities, does not always produce realistic results. Boundary conditions and aspect ratio affect the reliability of the results to a large extent; a thick beam with stresses prescribed at all its boundaries does not pose a problem, whereas a slender beam with prescribed displacements at some of its boundaries can cause erroneous results in the case of DIGS.

The Finite Difference Method as implemented in FLAC appears to be able to simulate beam bending more correctly, although convergence of the solution may take a large number of cycles.

In order to test both numerical approaches (DIGS and FLAC), a simple geometry, for which an analytical solution is available, has been used. This geometry is shown in Figure 6.4 and represents a single beam with a length l, a height of 1metre and an elasticity modulus of 70000MPa which is completely immobilised at the right hand side, completely unrestrained at the left hand side and loaded by a uniformly distributed vertical load of 0.027MPa (gravity only) along the entire length of the beam. The analytical solution is based on thin beam theory in which it is assumed that plane sections remain plane, that linear elasticity is applicable, the thickness of the beam is small compared to its length and

second order effects can be neglected. The following relation between the vertical load (p) on the beam and the vertical deformation (w) of the beam is then valid:

$$p(x) = -EI\frac{d^4w}{dx^4} \tag{6.1}$$

in which E represents the elasticity modulus, I the moment of inertia and x the distance along the beam.

The horizontal stresses in the beam can be calculated from:

$$\sigma(y) = \frac{M(x)y}{I} \tag{6.2}$$

in which y is the distance across the beam, measured from the centreline, and $M(x)$ is the bending moment at a particular cross section of the beam.

The horizontal stress at the immobilised (clamped) side of the beam along the top surface is then:

$$\sigma(top) = \frac{3p(x)l^2}{h^2} \tag{6.3}$$

in which h is the height of the beam. For this particular case it follows that:

$$\sigma(top) = 0.081l^2(MPa) \tag{6.4}$$

The vertical deformation at the unrestrained side can be expressed for this case as follows:

$$w(l) = 5.786{*}10^{-4}\,l^4{*}(mm) \tag{6.5}$$

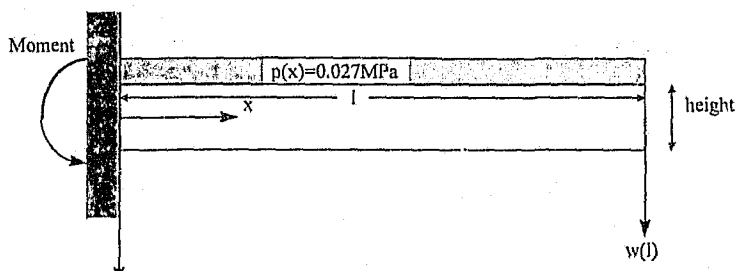

Figure 6.4 Cantilevering beam which is clamped on the left hand side

Layered strata can effectively be represented by individual beams stacked on top of each other. In order to obtain a correct representation of the stress distribution in these layers it is necessary that the individual beams are represemed in a realistic way. The purpose of this analysis is to investigate to what extent the numerical solutions deviate from the analytical solution.

The results from numerical simulations with DIGS are shown in Figure 6.5 in which the calculated and theoretical values are plotted against the number of iterations. In this simulation a beam of 10m length and 1m height has been represented by elements of 0.5m length

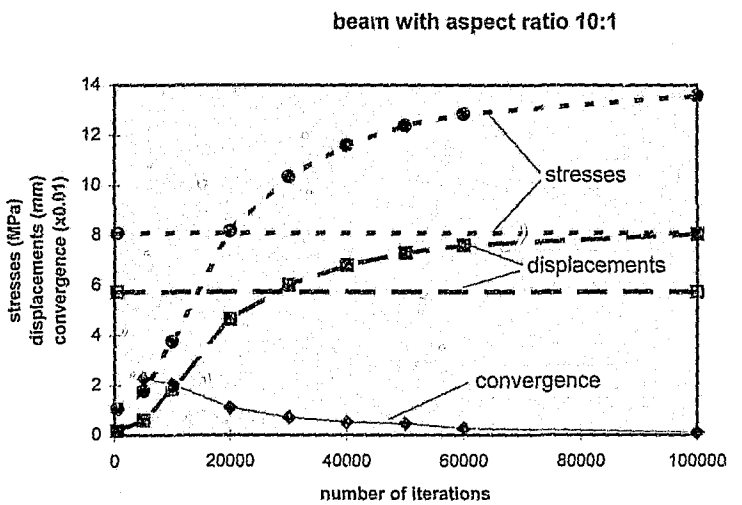

Figure 6.5 Theoretical and numerical (DIGS) values for stresses and displacements in a cantilevering beam (theoretical values are indicated by horizontal lines)

It is clear from Figure 6.5 that although convergence does occur ultimately after a very large number of iterations, the computed values for the stresses and displacements *exceed* the theoretical values by 40-68%. A model in which the element density was doubled, by reducing the element length to 0.25m, resulted in improved values for both the displacements and the stresses, although the reported error was orders of magnitude higher than in the case of the larger elements and convergence did not appear to take place.

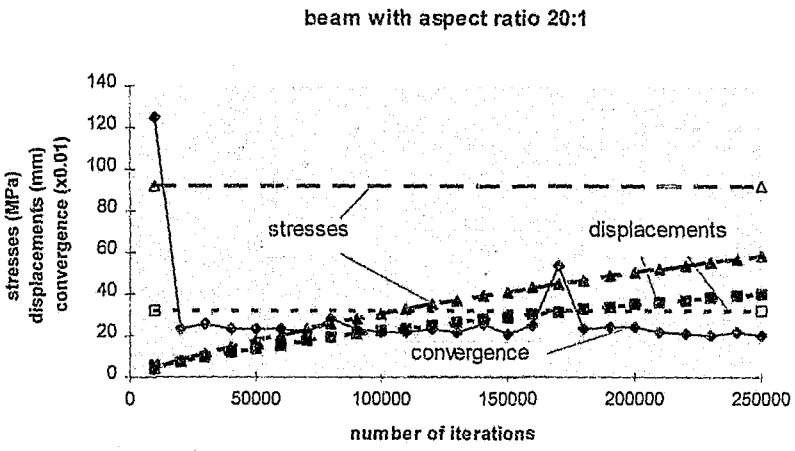

Figure 6.6 Theoretical and numerical (DIGS) values for stresses and displacements in a cantilevering beam

Figure 6.6 shows that convergence cannot be reached even after an extremely large number of iterations. It is not clear to which values the numerical results tend to asymptote, but this becomes irrelevant as the computational time required for these calculations prohibits any practical applications and, judging from the previous case, the results cannot be expected to be correct either. It was found that correct results and rapid convergence did take place when an aspect ratio of 5:1 was chosen for the beam, but such a limitation puts severe restrictions on the potential of the programme to represent layered strata. It is for this reason that the results of deformations and stresses in hangingwall beams which are reported in this section have to be considered very carefully. Practical applications may, however, provide more favourable conditions than the situation depicted in Figure 6.4 and the problem may therefore be less severe as suggested here.

The finite difference programme FLAC has also been used to simulate the clamped beam as shown in Figure 6.4 and the results of a beam with an aspect ratio of 20:1 are depicted in Figure 6.7. Using elements of 0.5m length and 0.25 m height, the computed displacements at the free end of the beam are 89% of the theoretical value while the computed stresses near the clamped end are 92% of the theoretical value. Increasing the density by using elements of 0.25m by 0.125m led to computed displacements and stresses which were 95% and 100% of theoretical values, respectively. Although convergence was also relatively slow for all these cases, reasonable results could be obtained and the FLAC results for the layered strata can therefore be used with more confidence.

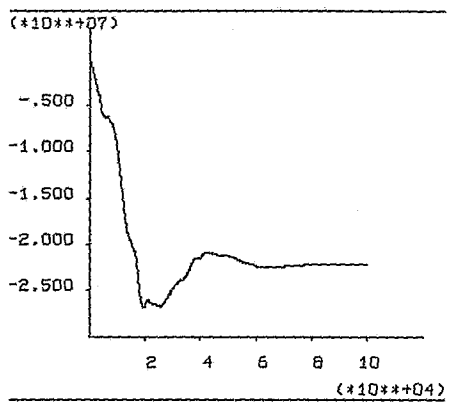

Figure 6.7 Axial stresses in the extreme beam elements (vertical axis) in relation to the step number in the iteration process (horizontal axis); Numerical simulation with FLAC

6.2.2 BEDDING PLANES IN FLAC SIMULATIONS

The following simulations have been carried out using FLAC. The influence of bedding planes on the stress distribution in general, and the failure potential in particular, has been investigated. The influence of parameters such as bedding plane spacing, friction coefficient, number of bedding planes and support resistance has also been addressed. While it was concluded in the previous section that the results from FLAC simulations can be expected to be more realistic than those from DIGS simulations in the case of layered strata, the FLAC simulations do not allow for a detailed failure analysis as it cannot represent fracturing. For this reason DIGS has been applied in the next section. Those results have to be treated with some care, as can be appreciated from the analysis on single beams in Section 6.2.1.

Figure 6.8 shows the stress distribution around a single stope in an elastic medium. The location of possible failure is indicated by contour lines which are based on a Mohr-Coulomb failure criterion and areas where minor principal stresses are tensile are also delineated by contour lines. Only a quarter symmetry around the stope is represented here as vertical and horizontal axes have been used as axes of symmetry. The cohesion has been set to 25MPa and the angle of internal friction to 30°. Two locations of potential failure can be observed in Figure 6.8, namely an area around the stope face, where a combination of large compressive stresses and a low confinement result in low values for the safety factor, and an area in the immediate hanging- (and foot-)wall, where excessive tensile stresses lead to low safety factors. The last area is not considered in this analysis as it is assumed that fractures induced near the stope face would absorb such tensile stresses in the back areas.

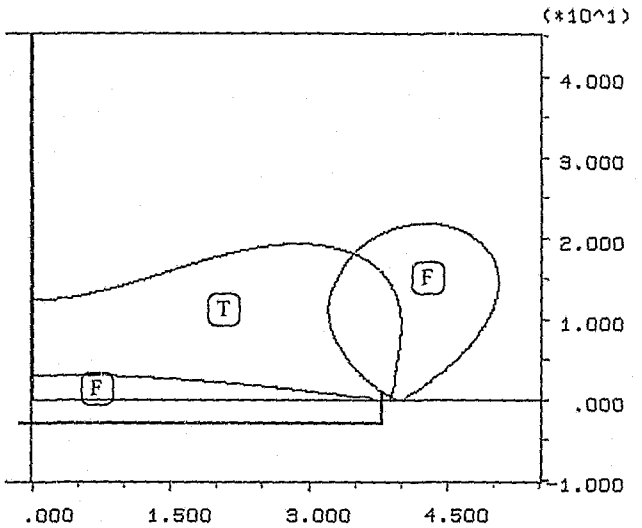

Figure 6.8 A longwall stope half span in an elastic medium; quarter symmetry; areas of potential failure according to the Coulomb shear failure criterion are indicated by F; the area where minor principal stresses are tensile is indicated by T

Figure 6.9 is a typical result from a simulation in which bedding planes are represented by planar discontinuities with varying frictional resistance and without any bonding strength or cohesion. It is clear from this figure that the stress distribution is to a large extent affected by the presence of bedding planes. The mechanism which influences the stress distribution is based on the limited shear resistance across the bedding planes which leads to the occurrence of shear deformation (slip) at locations of high shear stress exceeding the frictional resistance. Such locations can be found near the abutments, as indicated in Figure 6.9a and b. Relaxation of shear stresses across bedding planes results in displacements which induce rotations of the hangingwall and footwall layers towards the opening. Gravity will oppose the deformations in the foot wall while hanging-wall deformations will be enhanced.

In Figure 6.9 the spacing of the bedding planes is 2 metres, the coefficient of friction $\tan 20^{o}$, the stope span is 80 metres and a vertical load of 60MPa and a horizontal load of 30MPa is applied to the respective boundaries. This Figure shows only one of the models which are listed in table 6.1. It is of interest to note that the contours of potential failure (Figure 6.9b) according to a Mohr-Coulomb failure criterion, coincide more or less with the contours of tensile minor principal stress (Figure 6.9a). This indicates that all failure can be expected to be associated with tensile fracturing. In the case without bedding planes, shown in Figure 6.8, it can be observed that the area of failure near the abutments does not necessarily involve tensile stresses and failure in that situation can only be associated with (inelastic) shear deformations. By introducing discontinuities such shear deformations can be absorbed without failure of the intervening medium. However, the stress redistribution associated with these shear deformations may lead to the induction of tensile fracturing as will be demonstrated in the following section.

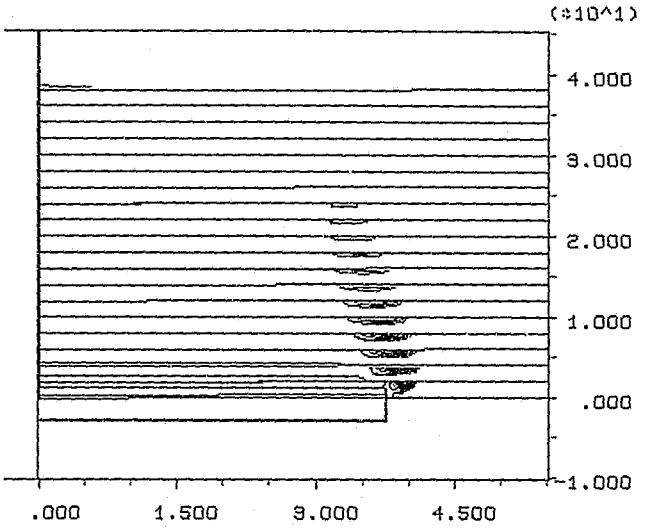

Figure 6.9a Bedding planes, spaced 2m. with friction coefficient of tan20°; contours delineated areas where minor principal stresses are larger than 5MPa.

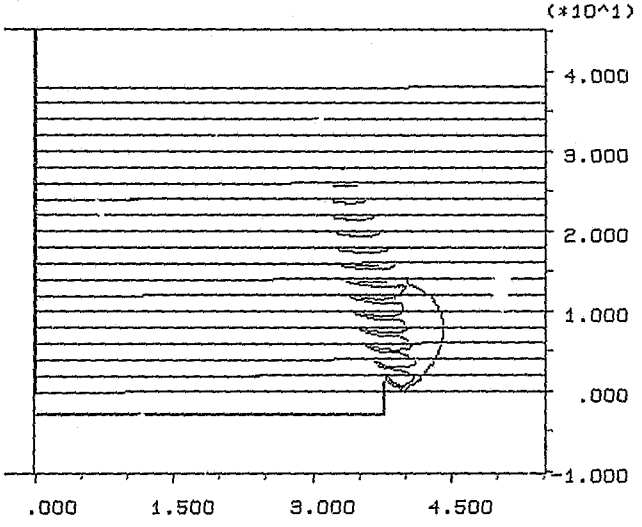

Figure 6.9b Bedding planes spaced 2m. with friction coefficient of tan20°; contours delineate areas of potential failure.

In order to analyse quantitatively the effects of bedding planes on stresses and deformations, parameters such as bedding plane spacing and friction coefficient have been varied and the results are shown in Table 6.1

Table 6.1 Results of various FLAC simulations on the effects of bedding planes

spacing (m)/ number of bedding planes	friction coefficient	support pressure (MPa)	horizontal stress at bottom/ top of beam (MPa)	maximum deformation @ midspan (mm)
no bedding	no bedding	none	39.1/---	77
2/1	0.176	none	29.6/5.7	153
2/1	0.364	none	33.3/12.6	136
2/1	0.577	none	35.0/18.0	120
4/1	0.176	none	29.7/-9.7	124
4/1	0.364	none	33.5/-0.5	111
4/1	0.577	none	36.0/6.0	101
2/19	0.176	none	19.0/-13.8	189
2/19	0.364	none	23.4/3.0	124
2/19	0.577	none	31.1/12.7	115
2/1	0.364	0.1	25.9/18.7	79
4/1	0.577	0.1	28.2/12.5	86
2/19	0.364	0.1	19.5/5.8	122
2/19	0.577	0.1	31.5/12.7	100
multiple mining steps				
2/19	0.364	none	23.3/3.1	127
2/19	0.364	0.1	20.4/5.0	120
2/19	0.364	10	-8.2/-11.2	95
2/19	0.364	60	-65.0/-63.0	27

The results presented in Table 6.1 suggest that the closure associated with multiple layers is smaller than the closure resulting from a single beam, provided the coefficient of friction is larger than 0.176 ($\tan 10^o$). Another interesting result is that while moderate support pressures can be sufficient to reverse the vertical inelastic deformation of a single beam, they becomes less effective if multiple beams are involved. Of special interest in this respect is the case where the support pressure has been increased to the original field stress (60MPa). Even in that case vertical deformations cannot be reversed completely and the original stress state is also not restored. The explanation for this behaviour is that shear deformations along the bedding planes become locked in and do not disappear when original loading conditions are restored. These effects are quite relevant to the representation of mining conditions in numerical models as this implies that the loading history, or mining sequence, can affect resulting deformations and stresses. The principle of superposition, which can always be applied in the case of elasticity, is not valid when (inelastic) displacements become locked in, such as in this case. A more detailed treatment on this subject is given by Kuijpers and Napier (1991). The effects of multiple mining steps are however hardly noticeable in the results which are given in Table 6.1.

It has also been demonstrated that the "crushing" of a face area in combination with the presence of bedding planes can result in the effective compression of the strata between such bedding planes (Kuijpers, 1992). The bedding planes limit the shear stresses which can be transmitted across them and in such a way contain the effects of the crushing to the area which is bounded by them. Without the presence of these bedding planes the effects of

the crushing would be distributed throughout the rock mass without inducing any compressive stresses in the strata surrounding the excavation.

6.2.3 BEDDING PLANES IN DIGS SIMULATIONS

The results which are reported in this section are based on DIGS simulations. Although these results may be affected by numerical problems, as can be appreciated from the discussion in section 6.2.1, the effect of an additional parameter, namely dilation along the bedding planes, can qualitatively be assessed. The main advantage of the DIGS simulations is however the fact that they can be used to study the effect of bedding planes on fracture generation. This will be demonstrated as well in this section. Table 6.2 summarises the results which are based on a stope span of 72m which is subjected to far field stresses of 60MPa in the vertical direction and 30MPa in the horizontal direction.

Although the analysis of a single beam in section 6.2.1 indicated erroneous behaviour of DIGS in that particular case, this does not suggest that the results of the following simulations are meaningless. It is obvious that potential errors may have occurred and absolute values may therefore be incorrect. However these simulations still have a qualitative value and the effects of various parameters may be evaluated. T

Support pressures are assumed to be uniformly distributed across the hangingwall of the total stope, the stresses which are reported in Table 6.2 are the horizontal stresses in the hangingwall skin at the centre of the stope and the deformations listed in Table 6.2 are the vertical deformations of the hangingwall at the centre of the stope. The coefficient of friction along the bedding planes is $\tan 30^{o} = \frac{1}{3}\sqrt{3} = 0.577$.

Table 6.2 Results of various DIGS analyses on the effects of bedding planes

spacing (m)/ number of beds	number of mining steps	support pressure (MPa) / bedding plane dilation (degrees)	resulting stress in hangingwall @ midspan (MPa)	maximum deformation @ midspan (mm)
no bedding	1	0/n.a.	30.0	118
1 to 5/8	1	0/0	?	135
1 to 5/8	1	0/30	?	147
1 to 5/8	18	0/30	?	164
1/8	1	0/30	?	126
1/8	18	0/30	?	136
2/8	1	0/30	?	150
2/8	18	0/30	?	172
4/8	1	0/30	20	167
4/8	18	0/30	?	171
4/8	1	0/30	17	139
8/8	1	0/30	?	147
8/8	18	0/30	?	147
2/16	1	0/0	12	144
2/16	1	10/0	2	124
2/16	1	30/0	-18	84
2/16	1	60/0	-48	25
2/16	1	0/30	14	173
2/16	1	10/30	-12	150
2/16	1	30/30	-35	107
2/16	1	60/30	-65	48
2/16	18	0/30	?	196
2/16	18	10/30	-40	151
2/16	18	30/30	-60	107
2/16	18	60/30	-90	48
6/5	1	0/30	24	157
6/5	1	0/0	21	135
8/4	1	0/30	27	147
8/4	1	0/0	24	132
10/3	1	0/30	29	137
10/3	1	0/0	27	129
15/2	1	0/30	29	127
15/2	1	0/0	31	124

note: the question marks indicate that these values have not been computed

The results from table 6.2 suggest that dilation along the bedding planes can contribute to a large extent to the amount of closure. Multiple mining steps seem to result in higher closure values, especially if the bedding plane spacing remains relatively small. It should however be noted that in the multiple mining step simulations, more iterations have been performed; this, together with the erroneous behaviour indicated in Section 6.2.1, may in itself have led to differences in the results. Another observation is that the number of bedding planes does affect the amount of closure, especially if dilation is involved. It can also be seen that the vertical extent of bedding plane presence in the hanging (and foot) wall plays a role. In this particular simulation, where a stope span of 72m was assumed, it was found that a total number of 8 bedding planes resulted in a maximum value of closure when the spacing between these bedding planes was selected at 4m so that they would be present up to a vertical distance of 32m from the excavation into the rock mass. Decreasing or increasing this distance would lead to smaller values for the deformation (closure). This indicates that stope parallel bedding planes are activated at a distance of approximately 32m normal to the stope in these particular simulations.

The spacing and number of bedding planes are directly related to one other in these simulations, as the spacing directly controls the maximum number of active bedding planes. The vertical distance from the stope, within which bedding planes can be activated, is limited to approximately 32m and a larger bedding plane spacing is therefore related to a smaller number of activated bedding planes. It is for this reason not realistic to address these parameters individually. Of more practical relevance is the issue of bedding plane extent into the rock mass. If bedding planes are omnipresent in the area where, due to mining induced stresses, mobilisation is possible, then the only parameter which will determine the total deformation is the number/spacing of bedding planes in that area. If however bedding planes do not completely cover the area of possible mobilisation, these deformations will be restricted. The deformations are not completely reversible and substantial vertical deformations and horizontal stresses are locked into the system even after support pressures have resumed the original vertical stresses (due to complete closure of the back area).

Figure 6.10 shows a typical result of a DIGS simulation with bedding planes. The area of interest is the abutment of the excavation as this is the location where fracturing is initiated in response to mining induced stresses. Both stress distributions and contours of tensile stresses are shown in Figure 6.10

Author Kuijpers J S
Name of thesis Identification Of Inelastic Deformation Mechanisms Around Deep Level Mining Stopes And Their Application To Improvements Of Mining Techniques Kuijpers J S 1998

PUBLISHER:
University of the Witwatersrand, Johannesburg
©2013

LEGAL NOTICES:

Copyright Notice: All materials on the University of the Witwatersrand, Johannesburg Library website are protected by South African copyright law and may not be distributed, transmitted, displayed, or otherwise published in any format, without the prior written permission of the copyright owner.

Disclaimer and Terms of Use: Provided that you maintain all copyright and other notices contained therein, you may download material (one machine readable copy and one print copy per page) for your personal and/or educational non-commercial use only.

The University of the Witwatersrand, Johannesburg, is not responsible for any errors or omissions and excludes any and all liability for any errors in or omissions from the information on the Library website.